

Dissertation zur Erlangung des Doktorgrades
der Fakultät für Chemie
der Ludwig-Maximilians-Universität München

Optical Investigation of Charge Carrier Dynamics in Organic Semiconductors and Graphene for Photovoltaic Applications



von
Karl Matthias Handloser
aus
München

2014

This work is dedicated to Gerit

Erklärung

Diese Dissertation wurde im Sinne von § 7 der Promotionsordnung vom 28. November 2011 von Herrn Prof. Dr. Achim Hartschuh betreut.

Eidesstattliche Versicherung

Diese Dissertation wurde eigenständig und ohne unerlaubte Hilfe erarbeitet.

München, den 18. Februar 2014

.....
(Unterschrift des Autors)

Dissertation eingereicht am:	18. Februar 2014
1. Gutachter:	Prof. Dr. Achim Hartschuh
2. Gutachter:	Prof. Dr. Christina Scheu
Mündliche Prüfung am:	24. März 2014

Abstract

Due to the raising demand on electrical energy the field of organic solar cells evolved rapidly within the last decades.

The detailed knowledge about energy transport within any used material is the key towards increasing light to energy conversion efficiency within the photovoltaic device.

Therefore the objective of the present thesis is the time resolved optical investigation of charge carrier dynamics and phenomena within organic semiconductors and graphene. Triggered by the need of becoming more and more independent from silicon based devices organic polymers are in the focus of current semiconductor research. A major drawback within the currently used organic polymers for photovoltaic applications is the short exciton diffusion length in combination with the high exciton binding energy compared to silicon or *III – V* semiconductors. These drawbacks limit current device designs to thin film applications only.

The present work is grouped into two segments.

Throughout the first part new device designs to raise the efficiency of light to energy conversion of polymer based devices within a interdisciplinary work among chemists and physicists are presented. Realized either by reducing non-radiative losses within exciton transport by the use of self induced ordering effects within the polymer or by the use of an covalent organic framework architecture. By filling this COF with an organic polymer the presence of electron-donor and acceptor in close proximity is realized, which was for the first time successfully demonstrated within a working device in the course of this thesis.

Another approach is the control on the film morphology, which leads to an increased efficiency of the resulting device, due to the optimization of electrical transport properties within the semiconductor. This increase of unpercolated pathways for charge carriers and its influence on efficiency is demonstrated for TiO_2 blocking layers and also for organic polymer films in the first part of the thesis.

To substitute silicon in different areas, graphene became another promising candidate for electronic and optoelectronic devices within the last decade due to its outstanding material properties. The huge variety of possible applications, ranging from serving as transparent electrode material up to transistor fabrication technology creates the demand of detailed information of charge carrier transport within this material.

In the course of the second part of this work the photoluminescence of exfoliated graphene flakes on different sample materials is used to investigate the time dependent inter- and intraband charge carrier dynamics. Fourier-plane imaging in combination with polarization pulse shaping is demonstrated to be a versatile tool to examine the emission characteristics of the ultrabroad non-linear luminescence. The applied theoretical models are in good agreement with the obtained experimental results and were able to clarify the influence of carrier-carrier scattering and phonon mediated energy transfer in time domain on the photoluminescence properties of graphene.

Contents

1	Motivation	vii
1.1	Synopsis of the thesis	ix
2	Previous knowledge and state of the art	3
2.1	Solar cells	3
2.2	Shaping of femtosecond laser pulses	6
2.2.1	Properties of light in media	6
2.2.2	Group velocity dispersion	6
2.2.3	The transform-limited pulse	8
2.2.4	Femtosecond polarization pulse shaping	9
2.2.5	Chirped laser pulses	9
2.2.6	Compressing the pulse	10
2.2.7	Bloch equations for semiconductors	11
2.2.8	Graphene Bloch equations	12
3	Experimental details	15
3.1	Setup	15
3.1.1	Leakage radiation detection and Back-focal plane imaging	18
3.2	Ultrafast experiments	19
3.2.1	Time correlated single photon counting	19
3.2.2	Grating-based 4f pulse shaper	21
3.2.3	Multiphoton intrapuls interference phase scans	23
4	Influence of metallic and dielectric nanowire arrays on the photoluminescence properties of P3HT thin films	25
4.1	Motivation	25
4.2	Materials and methods	26
4.3	Results and discussion	28
4.4	Conclusion	32
5	The interpenetrated network based photovoltaic device: charge transfer towards the included Fullerene	33
5.1	Motivation	33
5.2	Materials and methods	34
5.3	Results and discussion	35
5.4	Conclusion	40
6	Increasing crystallinity for improved electrical conductivity of TiO₂ blocking layers	41
6.1	Motivation	41
6.2	Materials and methods	42
6.3	Results and discussion	42
6.4	Conclusion	46

7	The influence of blocking layers on the performance of TiO₂ nanowire hybrid photovoltaic device	47
7.1	Motivation	47
7.2	Materials and methods	47
7.3	Results and discussion	48
7.4	Conclusion	54
8	Non-linear photoluminescence from graphene	55
8.1	Motivation	55
8.2	Materials and methods	55
8.3	Results and discussion	55
8.4	Conclusion	61
9	Controlling charge carrier relaxation and photoluminescence in graphene using chirped laser pulses	63
9.1	Motivation	63
9.2	Materials and methods	63
9.2.1	Sample preparation	63
9.3	Results and discussion	67
9.3.1	NL-PL intensity dependence on normalized chirp	67
9.3.2	NL-PL polarization dependence on normalized chirp	69
9.3.3	Modeling of the NL-PL	71
9.3.4	High and low power limit of the excitation	72
9.4	Conclusion	74
10	Summary and outlook	75
	Bibliography	76
	List of Figures	97
	List of Publications	99
	List of Conferences	101
	Curriculum Vitae	104

1 Motivation

Electrical energy and its generation is probably the key topic at the beginning of the 21st century. The continuously growing demand of electrical energy is nowadays mainly covered by conventional power plants burning fossil energy sources. Becoming more and more independent of fossil fuels is the major aim of mankind to ensure the coverage of the future need on electrical energy. Stimulated by this demand different approaches to harvest alternative energy sources were developed. This triggered an enormous effort of researchers in the area of light to energy conversion in universities, research institutes and companies. The most promising approach appears to be the generation of electrical energy by photovoltaics of different designs and materials.

Photovoltaic cells are based on the photovoltaic effect, which was for the first time experimentally demonstrated by Becquerel in 1839 [1] and 66 years later theoretically explained as the photoelectric effect by Einstein [2] for which he received the Nobel prize in 1921. Two decades later solar cells become commercially relevant in the 1940's. At that time the Bell labs had to answer the question which energy source to use for satellites. They decided to employ the patent by R.S. Ohl et al. [3] in which he suggested to use a p-n junction made from doped silicon to generate electrical energy out of light.

This first solar cell, which was based on a silicon p-n junction was proven to be inefficient because of the high concentration of impurities in the silicon. Soon after this first drawback Shockley et al. in 1947 and DuPont et al. in 1950 managed to purify the used silicon. In 1962 the Telstar1 satellite was equipped with 3600 silicon based solar cells [4]. From this time on the field of photovoltaic rapidly evolved up to present. Nowadays people try to maximize efficiency of light to energy conversion by the use of different solar cell designs and materials (see Chap.2). Two major classes of photovoltaic devices evolved within the last two decades. One is the inorganic device, which means a solar cell mainly built out of inorganic material (i.e. *III – V* junctions and silicon devices) and the other class is the respective organic device.

Since the large scale production of silicon and other inorganic semiconductor materials meeting the high purity requirements is expensive and energy consuming the organic device is supposed to be a suitable exchange for inorganic solar cells in future.

Organic polymers are beginning to play a key role in solar cell applications because of their appealing material properties (i.e. cost, tunable absorption,...). To increase the efficiency of these solar cells the two major disadvantages of polymers have to be overcome: The short exciton diffusion length on the order of a few tens of nm that is substantially smaller than the light absorption length and the extremely high exciton binding energy of $\approx 1\text{eV}$ in comparison to inorganic semiconductors (a few tens of meV for inorganic materials). Current device designs thus need to balance energy transport and light absorption efficiencies limiting in the case of P3HT (poly3-hexylthiophene), PCBM ([6, 6]-phenyl C₆₁-butyric acid methylester) or MDMO-PPV (poly(2-methoxy-5-(3'-7'-dimethyloctyloxy)-1,4-phenylenevinylene)) or comparable materials present applications to thin films only. Due to its material properties each polymer can serve as electron donor or acceptor. Sev-

eral strategies are currently being investigated that focus either on controlling the film morphology or on enhancing plasmonically light absorption [5, 6] within the device.

Overcoming the major drawbacks of each solar cell material means also gaining deeper insight into charge carrier dynamics of the respective material. Therefore fundamental knowledge about the charge carrier transport within certain devices and materials is necessary. Throughout the first part of this thesis several device designs have been studied by optical, electrical and electron microscopy investigations.

While the overall efficiency of all types of photovoltaic devices can be improved either by reducing contact resistance or using transparent contact materials to enhance light absorption graphene became strongly related to the topic of solar cells [7–9]. The material’s ability to conduct electricity without reducing the amount of transmitted light graphene is considered the most promising candidate for transparent conduction layers used in solar cells [10].

Graphene is a monolayer of sp^2 hybridized carbon atoms forming an honeycomb lattice. This material was already theoretically predicted to exist in 1947 by Wallace et al. in his textbook [11] and served up to present as model structure for theoreticians [12, 13]. Novoselov et al. invented a simple preparation method based on mechanical exfoliation of high quality bulk graphite. Therefore naturally kish graphite flakes are repeatedly peeled utilizing Scotch tape and then transferred to a substrate [14]. Another approach to fabricate graphene on a flat substrate is based on the epitaxial growth of graphene by thermally heating silicon carbide substrates to high temperatures [15, 16] and was presented by Berger et al also in 2004. Since this year graphene flakes in reasonable sizes and qualities were available, graphene attracted the first interest of the community. Novoselov et al. reported for the first time on electrical transport measurements on this material [17] in 2004. From this time on the Manchester group around A. Geim and K. Novoselov dominated the research in this field up to present. The physical effect identified as one of the most significant phenomena in condensed matter physics is the integer Quantum Hall Effect discovered by K. von Klitzing, G. Dorda, and M. Pepper in 1980 [18]. This effect is neither influenced by impurities or interface effects in the semiconductor since it depends exclusively on fundamental constants.

For their description and modeling of charge carriers as a two dimensional electron gas (2DEG) von Klitzing received the Nobel price in 1985. These quantum physical findings in combination with the availability of graphene for the community triggered an huge effort on fascinating experiments. The one with the highest impact in the field were on one hand the occurrence of the Berry’s phase [19] or experiments in which the relativistic properties of the charge carriers close to the Fermi level led to a near ballistic sheet conductivity [17]. A. Geim and K. Novoselov further theoretically predicted and showed experimentally that graphene has unique electronic properties, like the existence of quasi-particle excitations that can be described as massless Dirac Fermions.

This feature leads to the presence of a Landau level with zero energy in single layer graphene and hence to a shift of $\frac{1}{2}$ in the filling factor of the Hall conductivity.

A. Geim and K. Novoselov from the University of Manchester received 2010 the Nobel prize for their work on the anomalous quantum Hall effect [20, 21] at room temperature in graphene.

Due to its unique optical, electro-optical and structural flexibility, which is reflected in its electronic properties [22–30], like lowest room temperature resistance of any known material, outstanding mechanical strength and many others this material seems to be suitable for being used in many different devices either enhancing the device performance or to reduce its power consumption due to the extremely high room temperature charge carrier mobility of $30000 \text{ cm}^2/\text{Vs}$ [31, 32] and the extremely high thermal conductivity [33, 34]. In combination with its impressive mechanical properties (Young modulus 0.5 TPa) [35–37], which were also mentioned in the nobel announcement by an impressive Gedankenexperiment: *"1 square meter graphene hammock would support a 4 kg cat but would weigh only as much as one of the cat's whiskers, at 0.77 mg (about 0.001% of the weight of 1 m² of paper)"* [38] make graphene a promising candidate for a variety of applications.

The complete set of properties ranging from the chemical characterization to other material properties of graphene can be found elsewhere [39, 40]. These properties led to different applications [16, 22, 41–44], such as field effect transistors [45–47], field emission displays [48], , fast graphene based photodetectors [47, 49–51], photovoltaic devices [52, 53] or as saturable absorber in modelocked laser systems [54, 55]. Recently it was shown that graphene retains its impressive set of properties even when it is coated with a silicon film by molecular beam epitaxy (MBE) [56]. This knowledge opens up a new opportunity for the future design of inorganic or hybrid photovoltaic devices. To completely utilize the full potential of the wonder material graphene detailed knowledge about its key properties for each application is necessary. For the use in electronic devices the charge carrier dynamics in graphene is probably the most relevant property.

Insight into the electronic band structure and the related material properties of graphene were given by a lot of fascinating experiments and techniques, like optical absorption [57], Raman scattering [58–63], two photon absorption [64], pump-probe [65], phonon lifetime [66] and many other optical and non-optical experimental techniques. These experiments gave insight into many different material properties, like mobility of charge carriers, reflectivity and structure and addressed many open scientific questions.

Since charge carriers in graphene are considered to behave like massless Fermi-Dirac particles their ultrashort dynamics are extremely challenging to be extracted experimentally.

1.1 Synopsis of the thesis

The experimental work presented in this thesis is grouped primarily in two segments each addressing certain scientific questions regarding the photophysics of organic polymers (Chap. 4, Chap. 5, Chap. 6, Chap. 7) and graphene (Chap. 8, Chap. 9). The first experimental section addresses different approaches to enhance either light absorption or reduce non-radiative losses within different organic polymer thin films suitable for photovoltaic applications.

In the second part of this thesis a new experimental technique combining ultrafast pulse shaping with leakage radiation microscopy making use of the strong non-linear photoluminescence (NL-PL) signal from graphene is introduced. Photoluminescence and its emission characteristics is used to get further insight into the dynamic of energy transfer from the excitation towards the charge carriers and is a versatile tool to investigate carrier-carrier interactions occurring on ultrafast timescales. In (Chap. 8 and in Chap. 9)

detailed investigations and theoretical modeling of the photoluminescence of graphene are presented. These findings range from the generation to the controlling of the photoexcited radiative and non-radiative emission by characterizing the emission energy, polarization and the influence of the photoluminescence on excitation power and energy [25,65,67–72].

Each experimental chapter starts with an short motivation section which introduces the scientific problem to the reader and reviews the current state of knowledge.

The present thesis is composed as follows:

Chapter 2 and Chapter 3 establishes the theoretical and experimental background and is intended as a brief overview about the current state of knowledge.

In Chapter 4 the optical properties of organic semiconductor thin films (MDMO-PPV and P3HT) deposited on nanostructured surfaces are investigated using time-resolved two-photon photoluminescence (PL) microscopy. This chapter is intended to show the possibility to enhance the efficiency of organic photovoltaic devices by nanopatterning of the used substrate. The surfaces consist of parallel metallic or dielectric nanowires forming well-defined arrays on glass substrates. Keeping the nanowire dimensions constant and varying only their spacing from 40-400 nm the range of different types of nanowire-semiconductor interactions is studied. Nanostructured surfaces, when fabricated across large areas, could be used to control film morphologies and to improve energy transport and collection efficiencies in P3HT-based solar cells.

Chapter 5 describes the filling of 3 nm pores in an covalent organic framework (COF) with [6,6]-phenyl-C61-butyric acid methyl ester (PCBM). Since PCBM serves as electron acceptor and the thieno[2,3-b]thiophene-COF (TT-COF) as donor, the architecture of a photoconductive thienothiophene-based covalent organic framework is utilized to overcome one of the major disadvantages of any polymer based solar cell: the short exciton diffusion length within the organic polymer. This chapter describes the chemical generation of the used TT-COF and the the experimental proof that the PCBM completely filled the pores. In the last section of this chapter the working device built out of the nanostructured matrix of TT-COF and PCBM is presented and its efficiency is evaluated as a proof of principle measurement.

In Chapter 6 the results on the optimization of the TiO_2 blocking layer to improve the efficiency of organic and hybrid solar cells is presented. The major aim of the present work is to increase the electrical conductivity within the TiO_2 blocking layer to guarantee for efficient charge carrier transport and separation. This is realized by optimizing the calcination process towards an increase in particle/domain size to increase the unpercolated pathways for charge carriers and to get deeper insight into the morphology of the sol-gel produced films.

In Chapter 7 a hybrid organic solar cell consisting of upright freestanding TiO_2 nanowires embedded in an P3HT thin film is presented. The influence of the fabrication method of the blocking layer on the TiO_2 nanowires to guarantee for efficient charge carrier transport and separation is investigated by time resolved photoluminescence measurements and electrical transport measurements. Differences of morphology and of the constituents of

the blocking layer are investigated by scanning and transmission electron microscopy.

Chapter 8 reports on the strong broadband photoluminescence signal obtained from exfoliated graphene flakes after femtosecond laser excitation on transparent dielectric substrates. Since graphene is a zero gap semiconductor this effect arised completely unexpected by the community in 2010. This non-linear effect could be described by several models presented throughout this chapter.

To gain further understanding and allow for verification of the applied models the influence on the NL-PL intensity and energy of varying excitation energy and power is investigated.

In Chapter 9 the NL-PL from single and few layer graphene based on the findings presented in Chapter 8 is further investigated. Since this effect is explained by two competing models [73–75] the strong photoluminescence of graphene is in the focus of current research. Controlling the excitation of charge carriers within the graphene flake allow for drawing conclusions about the microscopic carrier-carrier interactions. In the course of this section it is shown that the control of the optical excitation of graphene leads to a control over the coupled coherence and the respective population dynamics of charge carriers. Therefore the NL-PL created by chirped broadband femtosecond laser pulses launches surface plasmon polaritons (SPP) in a thin Au-film in the direction of the excitation. These radiative emission generated by the SPPs is detected via leakage radiation microscopy to extract the original spatial distribution of the exciting photoluminescence. The obtained experimental results provide insight into the microscopic polarization and its relaxation dynamics. Positively chirped excitation pulses for which the lower energy of the pulse interacts first with the sample maximizes the NL-PL intensity. The theoretical models applied within this chapter are developed by E. Malic and his co-workers [28, 29, 76, 77] which are in general agreement with the experimental results presented.

2 Previous knowledge and state of the art

This chapter provides theoretical descriptions and previous knowledge useful for the understanding of the presented experiments in the course of this work.

2.1 Solar cells

Based on the photovoltaic effect, which was for the first time experimentally demonstrated by Becquerel in 1839 [1] and 66 years later theoretically explained as the photoelectric effect by Einstein [2] for which he received the Nobel prize in 1921 the first patent of a silicon based solar cell was sent to the US patent office in 1941 by Ohl and co-workers [3] (see Fig. 2.1).

Driven by the wish of extending working time for satellites Chapin and co-workers built the first solar cell based on a p-n junction out of silicon [78]. This is the best known and most built basic concept for solar cells up to present.

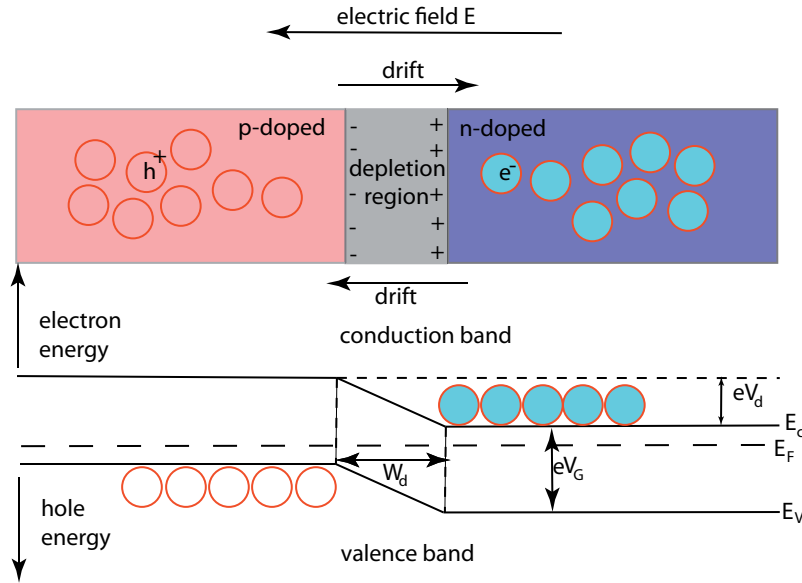


Fig. 2.1 Junction of a p and a n-type semiconductor. At zero bias the depletion region W_d is formed. This region is extended by a backward bias for effective charge separation for use in solar cells.

The width W_d of the depletion region within the p-n junction is extended by applying a backward bias $-V$ (see Eqn. 2.1). This leads to a more effective charge carrier separation

$$W_d \approx \sqrt{\frac{2\epsilon_r\epsilon_0}{q} \left(\frac{N_A + N_D}{N_A N_D} \right) (V_{bi} - V)} \quad (2.1)$$

and therefore to an increase of efficiency of the solar cell [79]. Here N_A and N_D is the number of free charge carriers (donor and acceptor) and the relative dielectric permittivity ϵ_r and the respective vacuum permittivity ϵ_0 and V_{bi} is the built-in voltage between p and

n-type semiconductor. To gain the maximum efficiency of the silicon solar cell device incoming light has to be absorbed completely. Therefore the penetration depth (skin depth) of visible light in silicon has to be taken into account.

The skin depth σ_{Si} is defined as the depth below the surface of the (semi-)conductor at which the current density has fallen to $1/e$ with respect to its value J_S at the surface.

$$\sigma_{Si} = \sqrt{\frac{2\rho}{\omega\mu}} \quad (2.2)$$

With the resistivity ρ and the angular frequency ω and μ the absolute magnetic permeability.

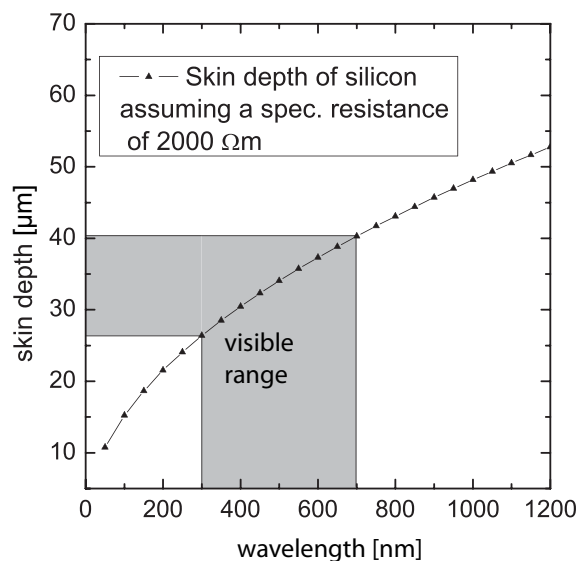


Fig. 2.2 Calculated penetration depth (skin depth) of light into silicon based on Eqn. 2.2.

Fig. 2.2 shows the relatively long skin depth of silicon for visible and infrared light. Since the fabrication of silicon is expensive and energy consuming many different materials and designs were invented within the last two decades to reduce costs and raising efficiency. The dominating types of solar cells can be classified into Silicon [78], *III-V* [80], thin film chalcogenide [81], amorphous silicon [82], photochemical or dye sensitized [83], organic [84] and the so called multi-junction devices [85], which show efficiencies up to 50% [86].

Organic polymers are cheap, non-toxic, easy to fabricate, printable and have with that unbeatable advantages compared to any other known solar cell material. These material properties have been the driving forces for the development in organic photovoltaic devices raising their efficiency from $10^{-5}\%$ in the early 70ies to almost 10% nowadays [87].

Despite this remarkable progress within the last four decades the difference in efficiency of $\approx 10\%$ to $\approx 30\%$ compared to silicon and *III-V* devices (see Tab. 2.1) makes further improvement necessary.

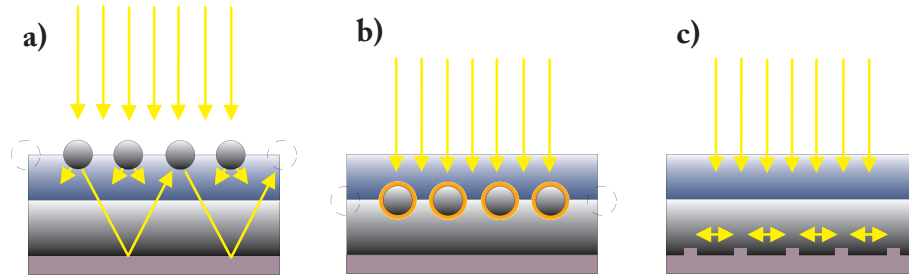
In the course of this work several approaches to improve efficiency of organic and hybrid organic solar cells are presented. These approaches aim on the reduction of the two major disadvantages of organic polymers: The relatively short exciton diffusion length and the high exciton binding energy in most of the polymers used for photovoltaic applications. Increasing efficiency of the organic photovoltaic devices is often realized by increasing the

Table 2.1 Efficiency records of different types of solar cells measured by independent test centers

	Efficiency [%]	J_{sc} [mA/cm ²]	Test centre (and date)
Si(crystalline)	25.0 ± 0.5	42.7	<i>Sandia</i> (3/99)
Si (multicrystalline)	20.4 ± 0.5	38.0	<i>NREL</i> (5/04)
Si (thin film)	19.1 ± 0.4	37.8	<i>FhG-ISE</i> (2/11)
Si (amorphous)	10.1 ± 0.3	29.47	<i>NREL</i> (7/09)
III-V cells (GaAs thin film)	28.3 ± 0.8	16.75	<i>NREL</i> (8/11)
Thin film chalcogenide (CIGS cell)	19.6 ± 0.6	34.8	<i>NREL</i> (4/09)
Photochemical (Dye sens.)	11.0 ± 0.3	21.93	<i>AIST</i> (9/11)
Organic thin film	10.0 ± 0.3	16.75	<i>AIST</i> (10/11)
Multijunction (GaInP/GaInAs/Ge)	34.1 ± 1.2	14.7	<i>FhG-ISE</i> (9/09)

amount of absorbed light by scattering from metal nanoparticles within the polymer thin film (see Fig. 2.3(a)).

Different solar cell designs [6] to enhance light absorption in the surrounding polymer are shown in Fig. 2.3. Here Fig. 2.3 a) shows a polymer film with randomly distributed metal nano-spheres serving as multiple scatterer for the incoming light. Subsequently the optical path within the polymer is extended while keeping the polymer film thickness constant. Additionally the strong plasmonic enhancement of the electrical field around the metal nanostructures can be used to transfer energy from the incoming light into the polymer (see Fig. 2.3(b) and [6]). Nanopatterning of the used substrate is another promising tool to enhance light absorption within the organic polymer (see chapter 4). This approach increases exciton diffusion length by extending the unpercolated pathways for electrons due to ordering of the molecules (see Fig. 2.3(c)) within the polymer film.

**Fig. 2.3** Different approaches to enhance light absorption in the surrounding polymer (adopted from [6]).

One approach to overcome the disadvantage of the short exciton diffusion length in PCBM is presented in Chap. 5. In this work it is shown that by filling the nanometer sized pores of a COF-system the charge carrier separation is drastically enhanced in comparison to thin film and blend devices.

2.2 Shaping of femtosecond laser pulses

2.2.1 Properties of light in media

To give deeper insight into the presented experimental results and techniques some calculations regarding the way light travels through media are described in this section. The mathematical descriptions presented in the following are mainly based on [88–90].

Group velocity

The group velocity v_g of a wave through a medium is defined as the inverse of the derivative of the wavenumber with respect to angular frequency:

$$v_g \equiv (dk/d\omega)^{-1} \quad (2.3)$$

With $k = \omega n(\omega)/c_0$ $dk/d\omega$ is expressed by:

$$\frac{dk}{d\omega} = \frac{n + \omega dn/d\omega}{c_0} \quad (2.4)$$

By plugging this into Eqn. 2.3 the group velocity reads:

$$v_g = \frac{c_0/n}{1 + \omega/n dn/d\omega} = v_{phase}/(1 + \frac{\omega}{n} \frac{dn}{d\omega}) \quad (2.5)$$

The refractive index $n(\omega)$ depends on the wavelength the group velocity is calculated in terms of the vacuum wavelength λ_0 . Therefore Eqn. 2.5 can be rewritten:

$$\frac{dn}{d\omega} = \frac{d}{d\lambda_0} \frac{d\lambda_0}{d\omega} \quad (2.6)$$

From there it follows for v_g :

$$v_g = \frac{c_0}{n} / (1 - \frac{\lambda_0}{n} \frac{dn}{d\lambda_0}) \quad (2.7)$$

From the presented equations it becomes clear that the propagation speed of light through a medium strongly depends on the wavelength dependent refractive index $n(\omega)$. In the experiments presented in Chap. 8 and in Chap. 9 the laser pulse characteristics are tuned on femtosecond timescales by modulating the refractive index within the spatial light modulator (SLM). For experimental details see Chap. 3. In the following the group velocity dispersion (GVD) and group delay dispersion (GDD) are introduced for describing the Fourier transform pulse shaping (FT-PS) technique presented in Chap. 3.

2.2.2 Group velocity dispersion

To create ultrashort laser pulses every optical element and its influence on the group velocity by its characteristic refractive index has to be taken into account. This is extremely sensitive, due to the fact that the refractive index of every known material depends on the wavelength. The group velocity dispersion (GVD) describes the propagation speed of light through media for different wavelength. Since an ultrafast laser pulse has a huge spectral bandwidth, due to the Fourier transform limit it is an important issue for every ultrafast experiment. The effect of a linear, passive optical device (lenses, prisms, etc.) on

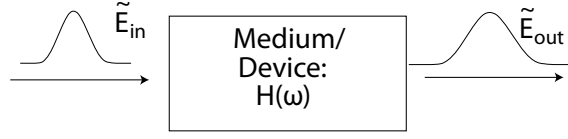


Fig. 2.4 Light properties are changed by traveling through medium or device. \tilde{E}_{in} describes the electrical field of the incoming Gaussian laser pulse, while \tilde{E}_{out} describes the respective electrical field after being influenced by the medium described by $H(\omega)$.

a optical pulse is to multiply the frequency-domain field by a transfer function:

$$\tilde{E}_{out}(\omega) = H(\omega)\tilde{E}_{in}(\omega) \quad (2.8)$$

While the transfer function $H(\omega)$ can be described by:

$$H(\omega) = e^{(-\alpha(\omega)L/2)} e^{-i\phi_H(\omega)} \quad (2.9)$$

The wave of the incoming and outgoing electrical fields $\tilde{E}_{in}(\omega)$ and $\tilde{E}_{out}(\omega)$ can also be described by $E(\omega) = S(\omega) \exp[-i\phi(\omega)]$. By plugging in the field functions into Eqn. 2.8, the spectral phase of the output light will be:

$$\phi_{out}(\omega) = \phi_H(\omega) + \phi_{in}(\omega) \quad (2.10)$$

The phase due to a certain medium with length L is defined as:

$$\phi_H(\omega) = \mathbf{k}(\omega)L \quad (2.11)$$

For a mathematical description of the dispersion of light in media the \mathbf{k} -vector is expanded in a Taylor series:

$$\mathbf{k}(\omega)L = \underbrace{\mathbf{k}(\omega_0)}_{\frac{\omega_0}{v_g(\omega_0)}} L + \underbrace{\mathbf{k}'(\omega_0)}_{\frac{1}{v_g(\omega_0)}} [\omega - \omega_0]L + \frac{1}{2} \underbrace{\mathbf{k}''(\omega_0)}_{\frac{d}{d\omega}[\frac{1}{v_g}] } [\omega - \omega_0]^2 \quad (2.12)$$

Here the second order term $\mathbf{k}''(\omega) = \frac{d}{d\omega}[\frac{1}{v_g}]$ describes the dispersion of the group velocity (GVD). This means that the group velocity will be different for different frequencies within the laser pulse while propagating through a medium.

A more convenient expression for the GVD is again in terms of wavelength. Taking into account that $\frac{d\lambda_0}{d\omega} = \frac{-\lambda_0^2}{2\pi c_0}$ and with that $\frac{d}{d\omega} = \frac{d\lambda_0}{d\omega} \frac{d}{d\lambda_0} = \frac{-\lambda_0^2}{2\pi c_0} \frac{d}{d\lambda_0}$ and Eqn. 2.7 one gets for the GVD:

$$\mathbf{k}''(\omega_0) = \frac{\lambda_0^3}{2\pi c_0^2} \frac{d^2 n}{d\lambda_0^2} \quad (2.13)$$

The group delay dispersion is defined as the $GVD \cdot L$, which leads with Eqn. 2.13 to:

$$\frac{d}{d\omega}[\frac{1}{v_g}] \cdot L = \mathbf{k}''(\omega)L \quad (2.14)$$

From Eqn. 2.11 and Eqn. 2.12 it becomes clear that the phase ϕ of the pulse within the optical medium holds:

$$\phi_H(\omega) = \underbrace{\phi_{H0}}_{\text{phase}} + \underbrace{\phi_{H1}(\omega - \omega_0)}_{\text{groupdelay}} + \underbrace{\frac{\phi_{H2}(\omega - \omega_0)^2}{2!}}_{\text{GDD}} + \dots \quad (2.15)$$

Eqn. 2.15 clearly shows that the phases for light propagating through optical media add a dispersive pulse broadening is unavoidable.

2.2.3 The transform-limited pulse

The duration of a transform-limited pulse (TLP) is completely determined by the inverse value of its spectral width $\delta\omega_{rms}$. This pulse is the shortest possible pulse without applying changes to phase or frequency of the pulse. For the following calculation a model pulse described by the complex amplitude $A_0(t)$ by the real envelope $\rho_0(t)$ and a phase $\phi_0(t)$ [88] is used.

$$A_0(t) = \rho_0(t)e^{i\phi_0(t)} \quad (2.16)$$

The pulse duration is defined as a root-mean-square (RMS) value

$$\tau_{rms} = [\tilde{t}^2 - \langle \tilde{t} \rangle^2]^{\frac{1}{2}}. \quad (2.17)$$

While

$$\tilde{t}^n = W_0^{-1} \int_{-\infty}^{\infty} t^n |A_0(t)|^2 dt, n = 1, 2, 3, \dots \quad (2.18)$$

with the pulse-energy $W_0^{-1} = \int_{-\infty}^{\infty} |A_0(t)|^2 dt$

The spectral width of the pulse is described in a similar way:

$$\Delta\omega_{rms} = [\tilde{\omega}^2 - \langle \tilde{\omega} \rangle^2]^{\frac{1}{2}}. \quad (2.19)$$

While

$$\tilde{\omega}^n = W_0^{-1} \int_{-\infty}^{\infty} \omega^n s_0(\omega) d\omega, n = 1, 2, 3, \dots \quad (2.20)$$

with the spectral density of the pulse $s_0(\omega)$:

$$s_0(\omega) = 2\pi |A_0(\omega)|^2 = (2\pi)^{-1} \left| \int_{-\infty}^{\infty} A_0(t) e^{-i\omega t} dt \right|^2 \quad (2.21)$$

The duration τ_{rms} of the pulse and its spectral bandwidth $\Delta\omega_{rms}$ are related as:

$$\tau_{rms} \Delta\omega_{rms} = K \geq \frac{1}{2}. \quad (2.22)$$

In case that the pulse duration τ_{rms} is completely determined by the inverse of the spectral width $\Delta\omega_{rms}$. For transform limited pulses the constant $K \approx 1$.

The used laser system provides Gaussian pulses with the following envelope:

$$\rho(t) = \rho_0 \exp(-t^2/2\tau_0^2) \quad (2.23)$$

It holds for a Gaussian pulse at the transform limit $K = \frac{1}{2}$.

The half-width of the pulse length at the \exp^{-1} point of the intensity is equal to $\tau_0 = \sqrt{2}\tau_{rms}$, while τ_0 is related to the pulse length at half-width $\tau_{\frac{1}{2}}$ by $\tau_{\frac{1}{2}} = 2\sqrt{\ln 2}\tau_0$

For a Gaussian pulse the pulse duration is described by:

$$\tau_0 \Delta\omega_0 = 2, \tau_{\frac{1}{2}} \Delta\omega_{\frac{1}{2}} = 4 \ln 2 \quad (2.24)$$

Assuming now a Gaussian pulse which phase varies in time quadratically.

$$\rho_0(t) = -\alpha_0 t^2 / 2 \quad (2.25)$$

This pulse is called phase modulated (PM). The quadratic dependence of the phase on time leads to an linear rate of frequency modulation α_0 in time.

$$\delta\omega(t) = \omega(t) - \omega_0 = d\rho_0(t)/dt = -\alpha_0 t \quad (2.26)$$

The frequency modulation (FM) described in Eqn. 2.26 is called linear chirp. Controlling the chirp of the optical pulse can be realized by the use of pulse shaping techniques in combination with a spatial light modulator.

2.2.4 Femtosecond polarization pulse shaping

In the course of this work computer-controlled femtosecond polarization pulse shaping technique was applied to control intensity, momentary frequency, and light polarization in time [91–95]. The influence of chirping the excitation laser pulses on the charge carrier recombination dynamics is presented in Chap. 9.

2.2.5 Chirped laser pulses

This section includes a mathematical description of the influence of positive and negative chirp [89] on the pulse characteristics based on the work of Piredda et al. [96]. Each single frequency component of the optical field can be expressed as negative time-exponentials

$$\hat{f}(\omega) = \hat{f}_0(\omega) \exp[i(kr - \omega t)] \quad (2.27)$$

The SLM adds a positive spatial phase $\varphi(\omega)$ to the pulse phase. This phase corresponds to the term $\exp(ikr)$, which is equal to $\exp \varphi(\omega)$. This leads to

$$\hat{f}(\omega) = \hat{f}_0(\omega) \exp[i(\varphi(\omega) - \omega t)]. \quad (2.28)$$

The integral over each single-frequency component represents the pulse in time domain

$$f(t) = \int_{-\infty}^{\infty} f_0 \exp(i\varphi(\omega)) \exp(-i\omega t) d\omega \quad (2.29)$$

and is the well known Fourier transform.

Since the pulse spectrum is centered around ω_0 it holds for $\hat{f}_0(\omega) = \hat{g}_0(\omega - \omega_0)$ and $\varphi(\omega) = \psi(\omega - \omega_0)$:

$$\psi(\omega - \omega_0) = \hat{C}(\omega - \omega_0)^2 \quad (2.30)$$

$$\hat{g}_0(\omega - \omega_0) = \exp\left[\frac{(\omega - \omega_0)^2}{\Delta\omega^2}\right]. \quad (2.31)$$

The pulse phase in the time domain will be then

$$\eta(\omega) = \exp(-iCt^2 - i\omega_0 t) \quad (2.32)$$

where C has the same sign of \hat{C} .

Therefore

$$f(t) = g(t) \exp(-iCt^2 - i\omega_0 t) = g(t) \exp[-i\eta(t)] \quad (2.33)$$

The instantaneous frequency is

$$\omega_{inst}(t) = \frac{d\eta(t)}{dt} = \frac{d(Ct^2 + \omega_0 t)}{dt} = 2Ct + \omega_0 \quad (2.34)$$

For positive chirp $C > 0$ the following values are extracted Tab. 2.2

Table 2.2 Chirp and frequency sequence

Case	frequency sequence	
for $t < 0$	$\omega_{inst} < \omega_0$	(red shift)
for $t > 0$	$\omega_{inst} > \omega_0$	(blue shift)

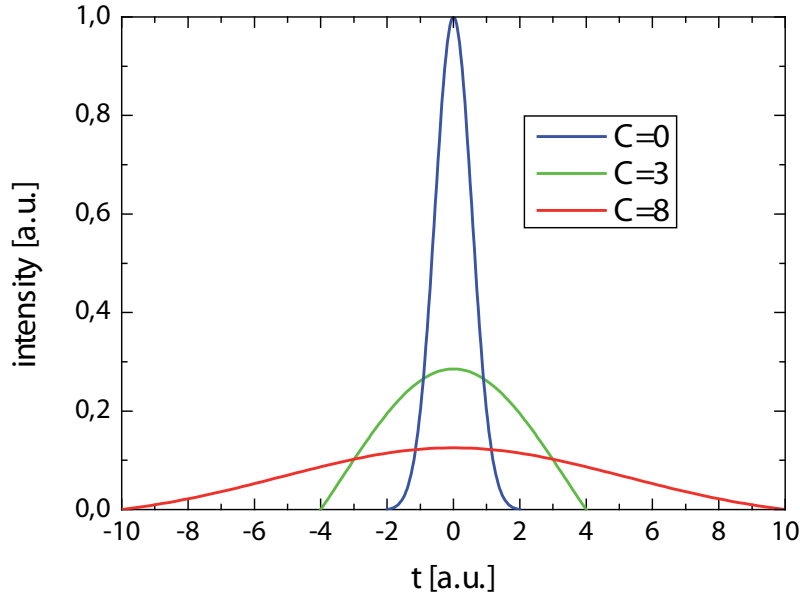


Fig. 2.5 Theoretical evaluated chirped Gaussian laser pulses like described in Sec. 2.2.5 keeping the overall fluence constant.

2.2.6 Compressing the pulse

Since every optical element adds a certain chirp to the pulse the whole system has to be corrected for this issue to guarantee for reproducible results. The compensation of second-order dispersion in femtosecond can be realized by the use of dispersive elements, like gratings [97,98] or prisms [99–101] or the combination of both [102] or alternatively by the use of chirped mirrors [103,104] or simply by the use of a Michelson interferometer [105].

2.2.7 Bloch equations for semiconductors

The optical response upon coherent excitation, such as laser sources of semiconductors can be described by the Bloch equations for semiconductors (SBE). These equations are based on quantum theory and form a closed set of integro-differential equations [89, 106–109].

The SBEs are named after the structural analogy to the optical Bloch equations that describe the excitation dynamics in a two-level atom interacting with a classical electromagnetic field. As the major difference with respect to the atomic approach, the SBEs must address the many-body interactions resulting from Coulomb force and scattering among charges and the phonon induced coupling of lattice vibrations and electrons, since the optical properties of semiconductors are determined by conduction and their respective uppermost valence bands. Since the SBEs include systematically many body effects within the semiconductor they are one of the most sophisticated and successful approaches to describe optical properties of semiconductors based on the classical description of light-matter interaction. The equations presented in this section are mainly based on the work of Lindberg and co-workers [106], since the influence of high and low power optical excitation on the relaxation dynamics is discussed within this work.

The Hamiltonian reads:

$$H = \sum_k \epsilon_c(k) a_{c,k}^\dagger a_{c,k} + \sum_k \epsilon_v(k) a_{v,k}^\dagger a_{v,k} + V. \quad (2.35)$$

The energies $\epsilon_c(k)$ and $\epsilon_v(k)$ are defined for a single electron in the lattice and the respective Coulomb interaction term V . The interaction of the exciting electric field is most often described by the rotating wave approximation [106], while it is assumed that the number of charge carriers is conserved within the band. The resulting equations of motion for the two expectation values for electrons and holes:

$$\langle a_k^\dagger a_k \rangle = n_{e,k}, \quad (2.36)$$

$$\langle b_{-k}^\dagger b_{-k} \rangle = n_{h,k}. \quad (2.37)$$

The expectation value for the microscopic polarization of the medium reads

$$\langle a_k^\dagger b_{-k}^\dagger \rangle = p_k^*. \quad (2.38)$$

While the first two expressions represent the population of electrons and holes within the band at certain k-values the third (microscopic polarization) becomes macroscopic because of the applied external electric field. By solving the Hamiltonian equation of motion:

$$\frac{\partial}{\partial t} \langle A \rangle = -i \text{tr}([A, H_{\text{tot}}] \rho), \quad (2.39)$$

based on Eqn. 2.35 one gets the time dependent coherent parts of the equation of motion, like described in [106]. This equations consider only the macroscopic expectation values, which translates to the diagonal matrix elements of the density matrix leading to an

effective Hamiltonian H_{eff} considering coherent excitation and scattering as well leading to the effective Bloch equations:

$$\frac{\partial}{\partial t} p_{k,coh}^* = i \left[\epsilon_e^s(k) + \epsilon_h^s(k) - \sum_{q(\neq 0)} V(q)(n_{e,k+q} + n_{h,k+q}) \right] p_k^* - i[\mu_k^* E^*(t) + \sum_{q(\neq 0)} V(q)p_{k+q}^*] \times (1 - n_{e,k} - n_{h,k}), \quad (2.40)$$

$$\frac{\partial}{\partial t} n_{e,k,coh} = -2Im \left[\left[\mu_k E(t) + \sum_{q(\neq 0)} V(q)p_{k+q} \right] p_k^* \right] \quad (2.41)$$

and

$$\frac{\partial}{\partial t} n_{h,k,coh} = \frac{\partial}{\partial t} n_{e,k,coh} \quad (2.42)$$

Since no scattering contributes in Eqn. 2.40 to Eqn. 2.42 holds for all k values:

$$n_{h,k,coh} - n_{e,k,coh} = 0 \quad (2.43)$$

In the work of Lindberg et al. [106] the coherent optical excitation of semiconductors in relation to high and low power regime is discussed and the influence on the Bloch equations for semiconductors is calculated.

It is worth noting that the resulting PL-intensity can be calculated either by the knowledge of p or n . Based on the finding presented in this section the graphene Bloch equations have been extracted by our cooperation partners Ermin Malic and his group [28, 29, 72, 76, 77, 110, 111]. The resulting theoretical approach to explain charge carrier excitation and relaxation mechanisms is used within the presented experimental results in Chap. 9.

2.2.8 Graphene Bloch equations

Based on the findings in Sec. 2.2.7 the following set of equations is evolved by our cooperation partners from the group of Prof. Malic. Further details can be found in [112]. The dynamics of the microscopic polarization $p_{\mathbf{k}}(t)$, is evaluated within graphene Bloch equations describing the coupling to the carrier occupation $\rho_{\mathbf{k}}^\lambda(t)$ in conduction and valence band ($\lambda = c, v$), and to the phonon population $n_{\mathbf{q}}^j(t)$ at the phonon momentum \mathbf{q} for different optical and acoustic phonon modes j [76].

Based on the Hamilton operator $H = H_0 + H_{c-f} + H_{c-c} + H_{c-ph}$ accounting for the non-interacting contribution H_0 , the semi-classical electron-field coupling H_{c-f} , the electron-phonon H_{c-ph} , and the electron-electron interaction H_{c-c} , the dynamics of the quantities of interest $\mathcal{O}(t) = p_{\mathbf{k}}(t), \rho_{\mathbf{k}}^\lambda(t), n_{\mathbf{q}}^j(t)$ is determined using the Heisenberg equation of motion:

$$i\hbar \frac{d}{dt} \mathcal{O}(t) = [\mathcal{O}(t), H]. \quad (2.44)$$

For the contribution to the Hamilton operator ($H_0 + H_{c-f}$) excluding the many-particle interactions, the evaluation of the commutator in Eq. (2.44) directly yields

$$\frac{d}{dt} \rho_{\mathbf{k}}^c(t) = -\frac{d}{dt} \rho_{\mathbf{k}}^v(t) = 2\Im[\Omega_{\mathbf{k}}^{vc*}(t)p_{\mathbf{k}}(t)], \quad (2.45)$$

$$\frac{d}{dt} p_{\mathbf{k}}(t) = -i[2v_F k - \Omega_{\mathbf{k}}^{vv}(t) + \Omega_{\mathbf{k}}^{cc}(t)]p_{\mathbf{k}}(t) - i\Omega_{\mathbf{k}}^{vc}(t)[\rho_{\mathbf{k}}^c(t) - \rho_{\mathbf{k}}^v(t)], \quad (2.46)$$

where v_F denotes the carrier velocity and $\Omega_{\mathbf{k}}^{\lambda\lambda'}(t) = i \frac{e_0}{m_0} \mathbf{M}_{\mathbf{k}}^{\lambda\lambda'} \cdot \mathbf{A}(t)$ describes the coupling between the carrier system and an external optical excitation represented by its vector potential $\mathbf{A}(t)$. Here, e_0 (m_0) is the free electron charge (mass) and $\mathbf{M}_{\mathbf{k}}^{\lambda\lambda'}$ is the electron-field matrix element [76].

Applying the correlation expansion and second-order Born-Markov approximation for the many-particle interactions H_{c-ph} and H_{c-c} , the equations obtain additional contributions and can be solved numerically. For further details see [76, 112].

$$\frac{d}{dt} p_{\mathbf{k}}(t) = -\gamma_{\mathbf{k}}(t) p_{\mathbf{k}}(t) + \mathcal{U}_{\mathbf{k}}(t), \quad (2.47)$$

$$\frac{d}{dt} \rho_{\mathbf{k}}^{\lambda}(t) = \Gamma_{\lambda\mathbf{k}}^{in}(t) [1 - \rho_{\mathbf{k}}^{\lambda}(t)] - \Gamma_{\lambda\mathbf{k}}^{out}(t) \rho_{\mathbf{k}}^{\lambda}(t), \quad (2.48)$$

$$\frac{d}{dt} n_{\mathbf{q}}^j(t) = \Gamma_{j\mathbf{q}}^{em}(t) [n_{\mathbf{q}}^j(t) + 1] - \Gamma_{j\mathbf{q}}^{abs}(t) n_{\mathbf{q}}^j(t), \quad (2.49)$$

The numerical solution of Eqs. (2.45-2.49) gives access to the coupled photo-excitation-induced dynamics of the microscopic polarization, carrier occupation, and phonon population resolved time, momentum, and angle.

$$\dot{p}_{\mathbf{k}}(t) = -[iv_F k + \gamma_{\mathbf{k}}(t)] p_{\mathbf{k}}(t) + \Omega_{\mathbf{k}} \Delta \rho_{\mathbf{k}}(t) + \mathcal{U}_{\mathbf{k}}(t), \quad (2.50)$$

where the driving term is the Rabi frequency $\Omega_{\mathbf{k}} = \frac{e_0}{m_0} \mathbf{M}_{\mathbf{k}} \cdot \mathbf{A}(t)$ with the electronic charge e_0 , mass m_0 and Fermi velocity v_f . The dynamics of the microscopic polarization depends on $\Delta \rho_{\mathbf{k}}(t) = \rho_{\mathbf{k}}^c(t) - \rho_{\mathbf{k}}^v(t)$, expressing the difference between the carrier occupations in the conduction and the valence band. Furthermore, the dynamics couples to ultrafast carrier scattering via diagonal dephasing:

$$\gamma_{\mathbf{k}}(t) = \frac{1}{2} \sum_{\lambda\mathbf{k}} \Gamma_{\lambda\mathbf{k}}^{in}(t) + \Gamma_{\lambda\mathbf{k}}^{out}(t) \quad (2.51)$$

and off-diagonal $\mathcal{U}_{\mathbf{k}}(t)$ dephasing, where $\Gamma_{\lambda\mathbf{k}}^{in/out}(t)$ describe time-, momentum-, and angle-dependent carrier scattering rates [76].

3 Experimental details

In this chapter the used measurement techniques are presented. At first the layout of each experiment is presented, while in the second part of the chapter time resolved measurement techniques are described in detail. In individual parts of this chapter a full overview about the used combination of a homebuilt inverted confocal laser scanning microscope (CLSM) and time correlated single photon counting (TCSPC) and ultrafast pulse shaping (UPS) is given.

3.1 Setup

The main part of the used setup is a inverted optical microscope. This CLSM (based on a Nikon Eclipse TE2000 platform) is used in epi/inverted-geometry (see Fig. 3.1), which allows for detecting exclusively light from a single plane. Here, a single infinity corrected microscope objective (Nikon CFI Plan Apo VC 60x NA 1.4) having sufficient transmission in the near infrared (IR) spectral region is used to excite and collect the optical response of the sample. The collimated laser beam (black line in Fig. 3.1) is reflected by a beamsplitter or a dichroic mirror and is focused onto the sample surface. The emitted light from the sample is collected by the same objective, reflected at the beamsplitter and focused by a second lens on a pinhole in front of the detector. The microscope is equipped with a piezo scan stage (Physik Instrumente PI-P-517.3) which allows for rastering the sample through the fixed focus within a range of $10000\mu\text{m}^2$.

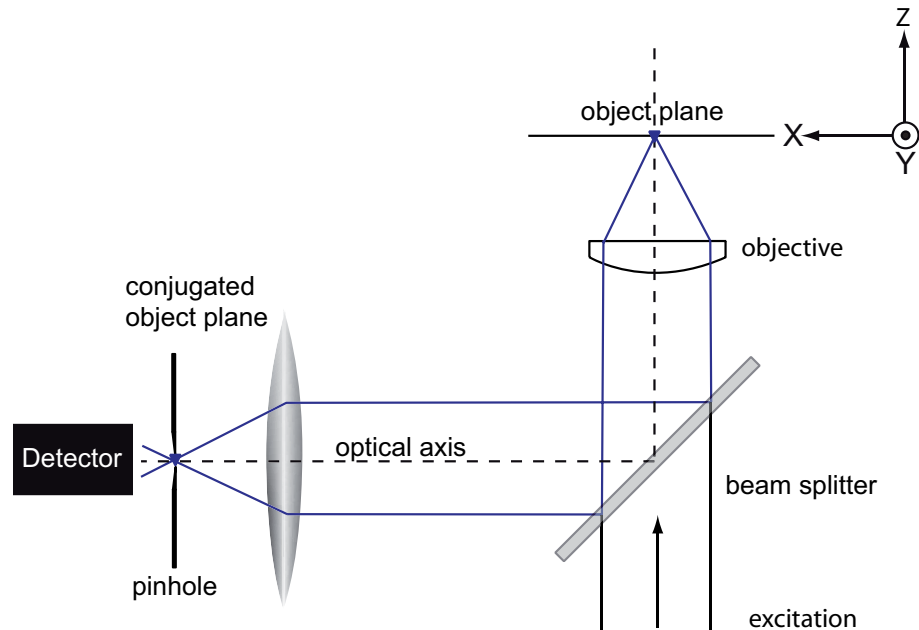


Fig. 3.1 The collimated laser beam is reflected by a beamsplitter and focused onto the sample surface. The emitted light from the sample is collected by the same objective, reflected at the beamsplitter and focused by a second lens on a pinhole in front of the detector (adopted from [113]).

The pulsed laser, which excites the optical response of the sample is a Ti:Sa oscillator (Coherent Mira) optically pumped by a frequency doubled (532nm) Nd:YAG (Verdi V10) laser (cf. Fig. 3.2). This system creates 150fs laser pulses at a tunable center wavelength λ between 760 – 900nm at a repetition rate of 76 MHz.

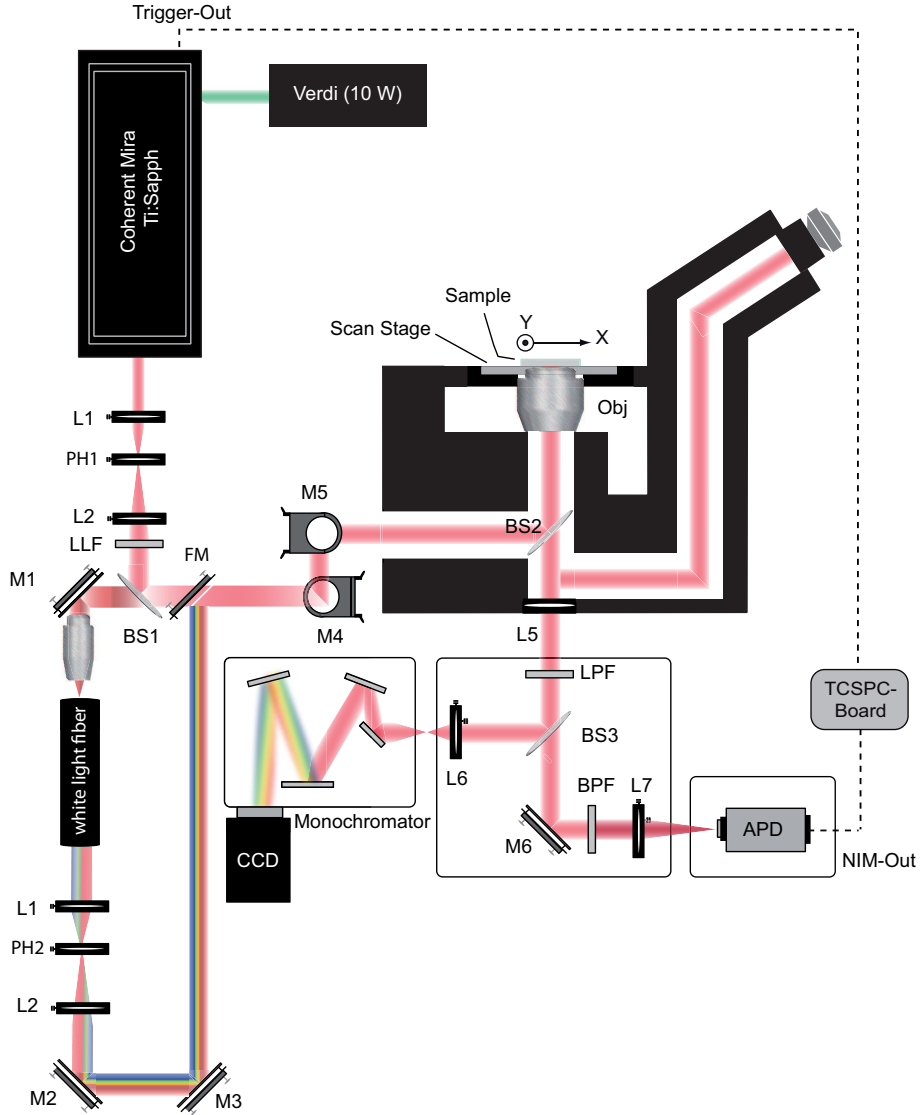


Fig. 3.2 This figure shows an illustration of the setup used for TCSPC experiments and confocal studies. A Ti:Sa oscillator provides femtosecond laser pulses which pump either a photonic crystal fiber to generate a white light continuum or can be used directly to excite the sample. Both beams can be used at the same time or in single pulse experiments. The detection allows for recording spectra via the monochromator and the CCD camera while the APD allows for time resolved intensity measurements.

Avalanche Photo Diode

An avalanche photo diode (APD) is a silicon based diode consisting of a p-n junction sandwiching an area free of charges (depletion region). The operation principle of an APD is based on the conversion of the energy of photons into free charge carriers in the semiconductor bulk and their further multiplication via the process of impact ionization.

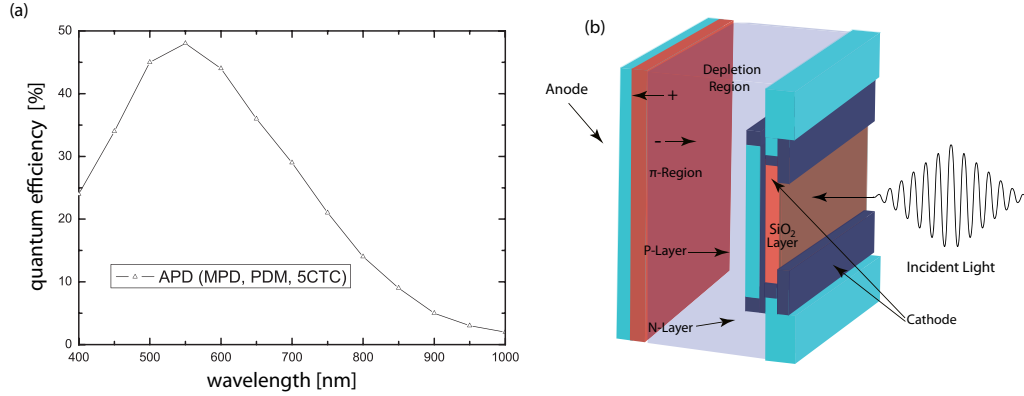


Fig. 3.3 (a) Quantum efficiency of the used avalanche photo diode. (b) Shows the working principle of an APD (adopted from [114]). Photons entering the diode first pass through the SiO₂ layer and then through the p and n layers before entering the depletion region. These highly energetic electrons create free charges in the depletion layer, which then migrate towards the electrode.

The basic element of the structure is the p-n junction. By reverse biasing this junction a volume is created where all charges drift towards their respective electrodes (depletion region). In an APD the charge carriers traversing this region acquire enough energy by the very high electric field ($> 10^5$ V/cm) to produce electron-hole pairs by impact ionization and with that an avalanche (avalanche breakdown) of electrons and holes moving towards the electrode. These current pulses are then detected in an external circuit. To achieve the gain needed for single photon detection the APD (MPD PDM) is operated with a reverse voltage above its breakdown voltage. This leads to a gain factor up to 10^6 on very short timescales. Since an extremely uniform field distribution over the sensitive area of the detector is necessary to reduce the noise level the biggest area available commercially is 2.5cm^2 [115] up to present.

Charged Coupled Device

The Charged Coupled Device invented 1970 by Boyle et al. [116, 117] is a well known semiconductor device for imaging technology. The photo-active region of this detector type consists of small transistors mostly out of silicon, which accumulate charges proportional to the light intensity by applying an electrical field. This trapped charges within each transistor are then transport towards an contact electrode by sequentially pulsing this electric field. Nowadays many different designs and architectures for different applications are commercially available.

To reduce the dark current generated by thermal electrons within the conductive layer the CCD device (Andor Newton & IDUS open electrode) is thermo-electrically cooled by a Peltier element to $\approx -70^\circ$ Celsius. This camera is mounted on a spectrometer (Shamrock 300i) consisting of different gratings to balance detection sensitivity and resolution for each application.

Detection Sensitivity

To estimate the detection sensitivity of the utilized experimental setup the transmission throughout the whole system is measured utilizing the white light source described in Fig. 3.2. Afterwards the optical transmission of every single element in the beam path is measured separately to extract its influence on the detected signals. The detection

sensitivity is mainly influenced by the quantum efficiency (see Fig. 3.3 a)) of the detection device (APD or CCD-camera) and by the beam splitter located directly underneath the microscope objective as depicted in Fig. 3.1.

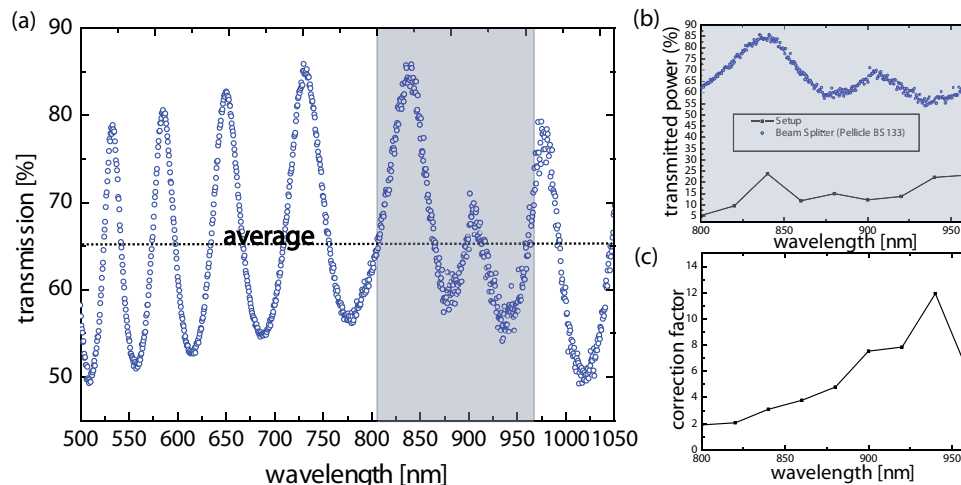


Fig. 3.4 (a) Shows the spectral modulations of the used setup caused mainly by the beam splitter. The gray shaded region is the most used detection range. To obtain reliable results the signal was corrected with the shown parameters ((b)(c)).

The resulting correction factor for the system is shown in Fig. 3.4. The resulting factor calculated by the quotient of the transmitted intensity with and without the losses of the setup is used throughout the presented experiments in the course of this work to correct the detected signals.

3.1.1 Leakage radiation detection and Back-focal plane imaging

Leakage radiation microscopy [118, 119] detection together with back-focal plane (BFP) imaging [120–122] was utilized to investigate the carrier relaxation with momentum (k_x, k_y) resolution in the presented experiments (see Chap. 9).

An emitter placed on a thin metal film can relax by launching propagating surface plasmons polaritons (SPPs). These SPPs are electromagnetic modes bound to the interface between the metal and the adjacent dielectric. In the present configuration two SPP modes are distinguished: The lower plasmon between the gold film and the glass substrate and the upper plasmon between gold film and an effective medium formed by the dielectric spacer layer and air. Due to momentum mismatch both SPPs can not couple directly to photons in the respective dielectric medium. Due to the larger refractive index of glass as compared to that of the dielectric spacer layer / air side, the upper plasmon, on the other hand, can couple to photons in the glass. This process is termed leakage radiation. For momentum conservation k_{SPP} has to match the in-plane photon momentum $k_{||}$ leading to the resonance condition $k_{SPP} = k_{||} = 2\pi/\lambda n \sin\theta$. As the result, leakage radiation is emitted into the lower halfspace at a certain angle θ that is determined by the frequency of the light emitted by the source and the SPP dispersion relation [123].

The angular distribution of emission can be visualized by imaging the BFP of the microscope objective. The resulting pattern directly reveals the intensity distribution with respect to photon momentum ($k_{||,x}, k_{||,y}$) and hence ($k_{SPP,x}, k_{SPP,y}$) (Fig. 3.5).

For an in-plane dipolar emitter the resulting image shows two arc-like features in the direction of the oscillating dipole that can be calculated according to [124]:

$$I(k_{||}, \varphi) = I_0 \frac{\cos^2(\varphi - \Phi)}{(k_{||} - k_{SPP})^2 + (2L_{SPP})^{-2}}. \quad (3.1)$$

Where L_{SPP} is the plasmon propagation length and Φ represents the orientation of the emitting in-plane dipole.

Eqn. 3.1 also quantitatively describes emission from extended structures as has been shown for quasi-one dimensional single-walled carbon nanotubes [120]. Unpolarized emission can then be represented by the sum of the emission patterns of two orthogonal in-plane dipoles leading to a ring of uniform intensity.

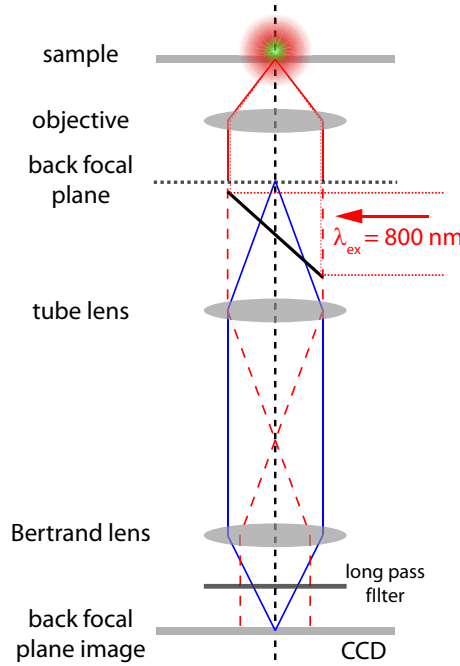


Fig. 3.5 Schematic of beam path used for back focal plane imaging. An additional lens (Bertrand lens) is introduced to image the back focal plane of the microscope objective onto a CCD camera.

A more detailed description of the underlying experimental technique can be found elsewhere [125].

3.2 Ultrafast experiments

In this section the used ultrafast experimental techniques are introduced. The presented methods provide picosecond and femtosecond time resolution. In the course of this work Time Correlated Single Photon Counting and Ultrafast Pulse Shaping experiments were carried out.

3.2.1 Time correlated single photon counting

Time correlated single photon counting (TCSPC) is a very sensitive technique to measure fluorescent lifetimes with picosecond time resolution (presented description based on [126]). The TCSPC measurement, which was conceived in 1961 by Bollinger and Thomas [127] relies on the concept that the probability distribution for emission of a single photon after

an periodic excitation can be monitored by plotting intensity against time distribution of all the photons emitted as a result of the excitation. By sampling the single photon emission after a large number of excitation flashes, the experiment constructs this probability distribution.

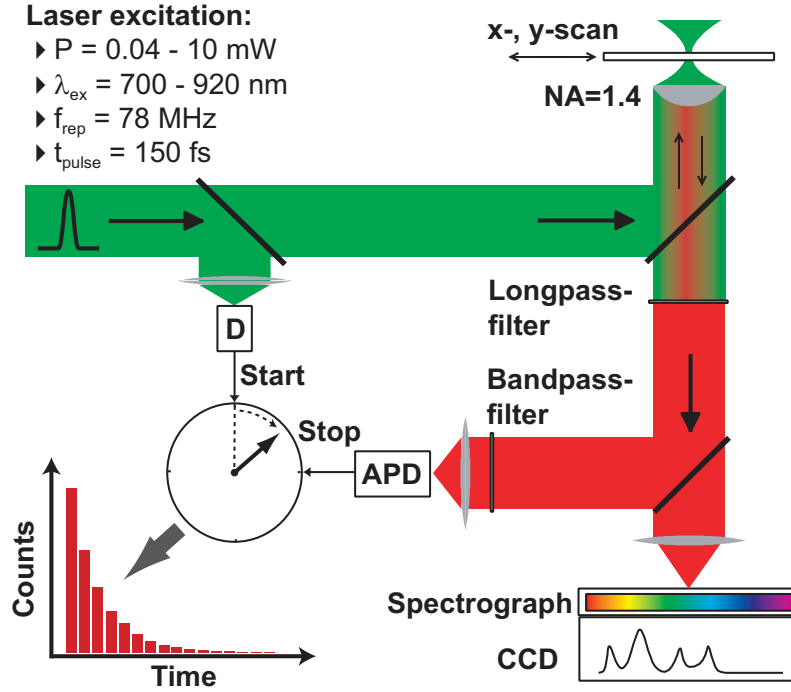


Fig. 3.6 Optical beam path and electronic of the used TCSPC setup. A femtosecond laser excites events at the sample, which are detected by the ultrafast electronic and statistically post-processed to extract for the evolution of each event in time (see text).

Ideally one fluorescence photon is observed every few hundred excitation laser pulses. The working principle is depicted in 3.7, while the layout of the optical beam path is visible in 3.6.

A single photon pulse creates a significant amplitude jitter (gain-noise) in all high gain detector, due to the random amplification process inside the device. The big advantage of the TCSPC-method compared to the analog read-out of high gain detectors is the effective suppression of this jitter, since photon counting is free of gain- and electronic noise as long as the noise amplitude is smaller than the photon-amplitude. Further technical and experimental details can be found elsewhere [113, 126, 128].

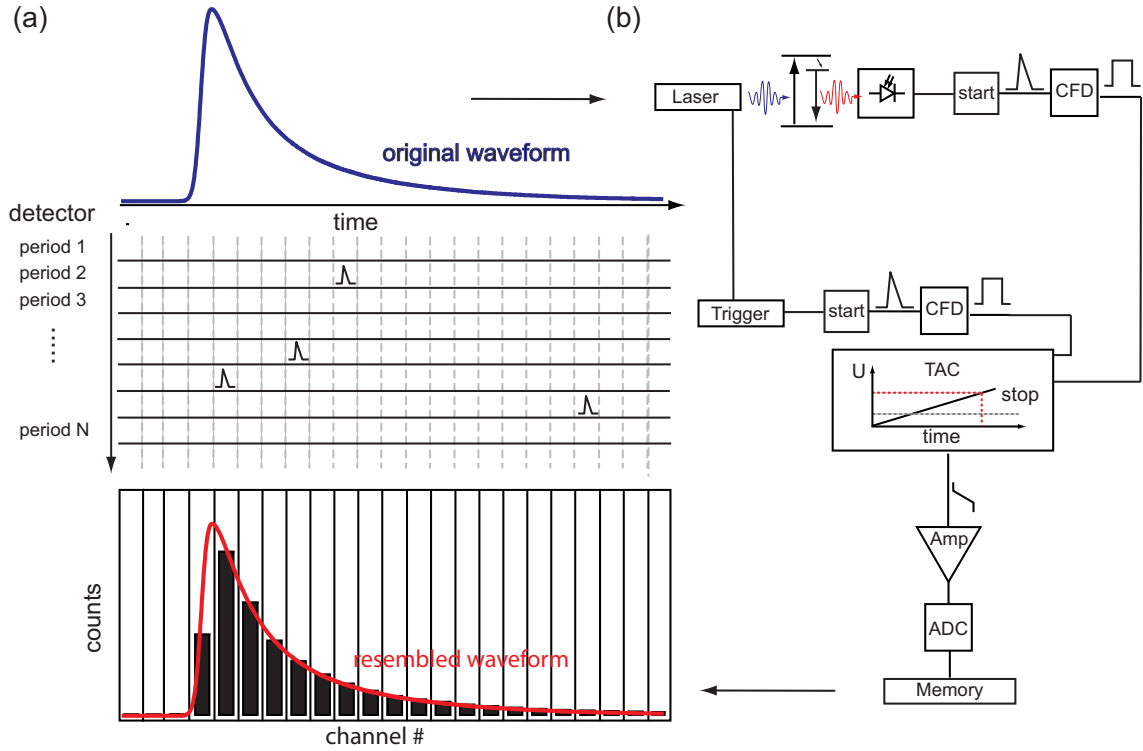


Fig. 3.7 Working principle of the TCSPC detection method consisting of a fast detector (MPD-PDM) and a digital circuit [126] for the readout (a). The detection device (MPD-PDM) is triggered by the TTL-pulses generated by the laser system. The time distributed photons are then used to resemble the original waveform utilizing a software applying the likelihood event approach (see text).

3.2.2 Grating-based 4f pulse shaper

In this section the experimental techniques for Fourier transform pulse shaping (FT-PS) are explained. The creation of focused laser pulses at the sample consisting of a certain and controlled pulse duration requires detailed knowledge about the laser pulse with respect to phase, spectrum and intensity.

The zero dispersion line

In 1983 Froehly [129] and co-workers introduced a new design for a pulse shaper, the zero dispersion line or 4f-shaper, a particular form of a spectrometer composed of two diffraction gratings and two lenses arranged in a 4f set-up. The detection device is replaced by a mask (see Fig. 3.8). Each spectral component is angularly dispersed by the first grating, then focused to small diffraction spots in the Fourier plane by the first lens. Thus, in this plane, all the spectral components are spatially separated and focused. Then a second combination of lens and grating allows for the recombination of all the frequencies into a single collimated beam. If nothing would have been placed in the Fourier plane then the device is dispersion free (zero dispersion, (see Fig. 3.8 a)) due to the symmetry of the system.

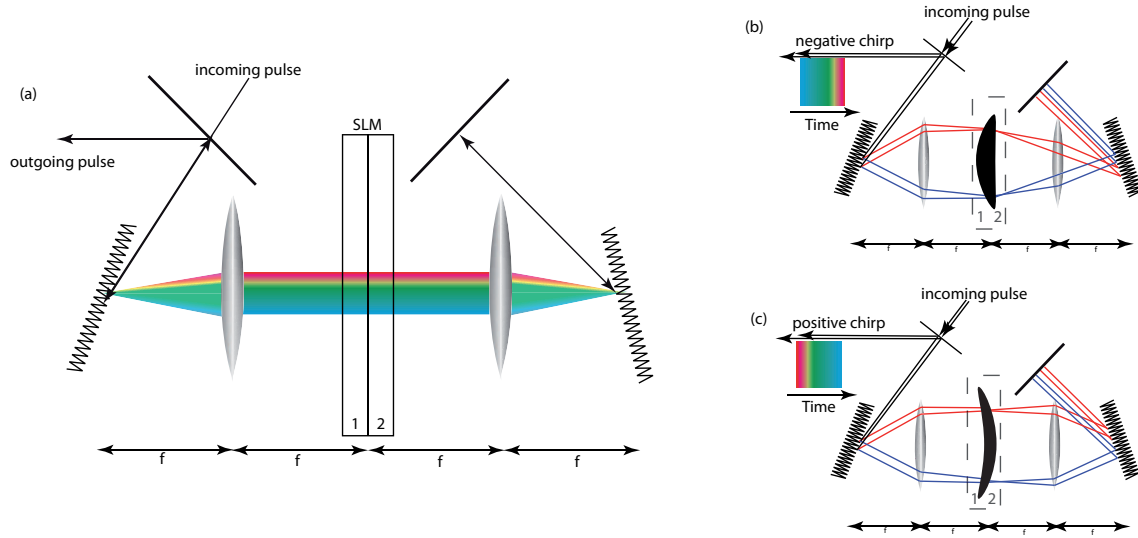


Fig. 3.8 Basic layout of the optical beam path used for Fourier-transform pulse shaping is depicted in a). The influence of negative chirp on the time evolution of the created pulse is shown in b), while the complementary phase function (positive chirp) is visualized in c).

Spatial light modulator

The used spatial light modulator (CRI SLM 128 Dual Mask) use one horizontal row of 128 nematic liquid crystal (LC) pixel to alter the phase or the polarization state of the laser pulse. Each pixel has a height of 5 mm and a pitch of .1 mm. The gap between each pixel is $2\mu\text{m}$ wide. The SLM is placed directly in the Fourier-plane of the zero dispersion line to influence the pulse characteristics Fig.3.8 in phase and amplitude. The

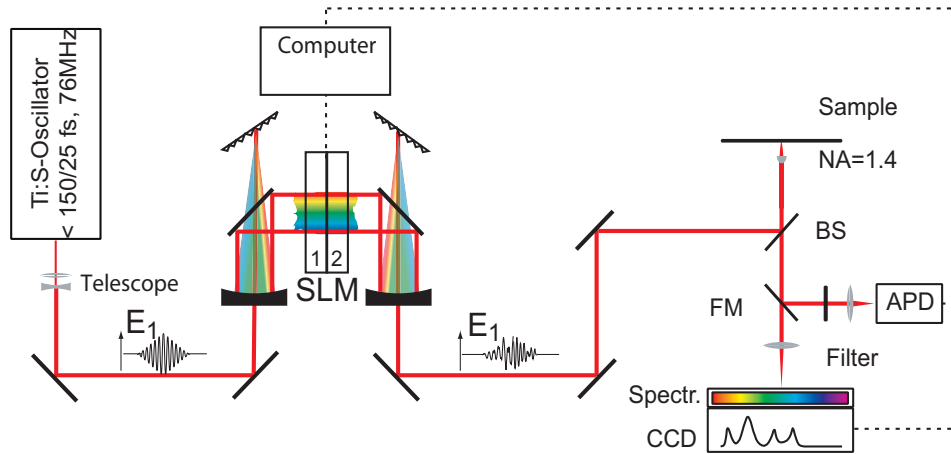


Fig. 3.9 Layout of the beam path used for pulse shaping experiments depicted in a). The femtosecond laser pulse is dispersed at a grating and send to the LC masks of the SLM. There the pulse is modified (see text) and resembled at a second grating. A zero dispersion line composed of two gratings and two lenses of focal length f , arranged in a $4f$ set-up. In the Fourier plane FP, all the spectral components are spatially separated and focused. [92,94].

molecules within the LC pixels are free to diffuse and are randomly distributed as in a liquid, but still maintain their long-range directional order (nematic), which is essential

for tuning the refractive index in every SLM pixel electrically along the axis parallel to the incoming light, while the orthogonal axis remains unchanged. By applying a electric field the refractive index along the this axis can be tuned and with that group velocity v_g for light at a certain wavelength within each pixel.

In the used SLM (CRI SLM-128) two of such LC-masks are mounted orthogonal to each other enclosing 45° with respect to the polarization of the incoming laser pulse.

This configuration allows for tuning phase and amplitude of the pulses at once. By equally addressing both masks by the control software the device can be used to modulate the phase only and create light of arbitrary polarization.

The influence of the applied phase function to the SLM masks on the pulse characteristic can be seen in Sec. 2.2.6. While the phase acquired by each frequency component of the pulse traveling through the SLM decreases with an increase of the LCM drive level. The used laser source is a Ti:Sa oscillator providing 150 fs pulses at a repetition rate of 76 MHz Fig. 3.9. To improve the temporal resolution of the experiments presented in Chap. 9 a single mode optical fiber was pumped by the fundamental of this laser system. By pumping a single mode optical fiber the spectral bandwidth is increased leading to pulse duration of ≈ 25 fs due to the formalism presented in Sec. 2.2.3.

3.2.3 Multiphoton intrapuls interference phase scans

To calibrate the experimental system used for the investigation of charge carrier dynamics in graphene (Chap. 9) Multiphoton intrapuls interference phase scans (MIIPS) were carried out. MIIPS is a method that combines iterative spectral phase characterization and compensation and has proven to be very well suited for optical microscopy experiments using femtosecond lasers in combination with a pulse shaper [91, 98, 99, 130, 131]. MIIPS takes advantage of the influence that phase modulation has on the probability of nonlinear optical processes at specific frequencies [132, 133]. In the presented experiments the second harmonic generation (SHG) from $\text{Fe}_2(\text{IO}_3)_3$ [134] is used to perform MIIPS. Nanocrystals of $\text{Fe}_3(\text{IO}_3)_3$ on glass served as reference sample material.

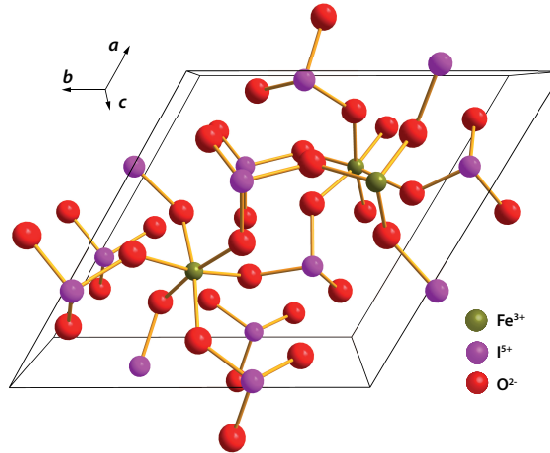


Fig. 3.10 Unit cell of the hexagonal $\text{Fe}_2(\text{IO}_3)_3$ crystals utilized for SHG generation in Chap. 9.

Within this material the second-order susceptibility $\chi^{(2)}$ is non-zero [89]. Assuming the exciting electric field strength of the laser as:

$$\tilde{E}^2 = E e^{i\omega t} + c.c. \quad (3.2)$$

After excitation of the $\text{Fe}_2(\text{IO}_3)_3$ the non-linear polarization within the crystal is described by:

$$\tilde{P}^{(2)}(t) = 2\epsilon_0\chi^{(2)}EE^* + (\epsilon_0\chi^{(2)}E^2e^{i2\omega t} + c.c.) \quad (3.3)$$

From Eqn. 3.3 it becomes clear that the second order polarization has a contribution at 2ω . This instantaneous process is used to measure the MIIPS traces depicted in Fig. 3.11. For further details on SHG see [89]. Since MIIPS is not based on autocorrelation between two events, no overlapping of beams in time or space is required. A series of calibrated reference phase functions are introduced, and the SHG spectrum resulting from each one is collected. The two-dimensional data (spectra vs phase parameter (Fig. 3.11)) contain enough information for an accurate phase retrieval. The calibrated reference function $\phi_{MIIPS}(\omega)$ is scanned across the spectrum of the laser pulse to reveal the unknown phase $\phi(\omega)$ of the pulse at the position of the sample. In general $\phi(\omega)$ is determined by the phase of the laser output, the 4f shaper and the dispersion of the optical elements such as the high NA objective, other lenses and filters. It has been shown that the second-harmonic-generation (SHG) spectrum resulting from the total phase $\Phi(\omega) = \phi(\omega) + \phi_{MIIPS}(\omega)$ that peaks for vanishing second derivative of $\Phi(\omega) \rightarrow 0$ can be used to retrieve $\phi(\omega)$ with high accuracy [130].

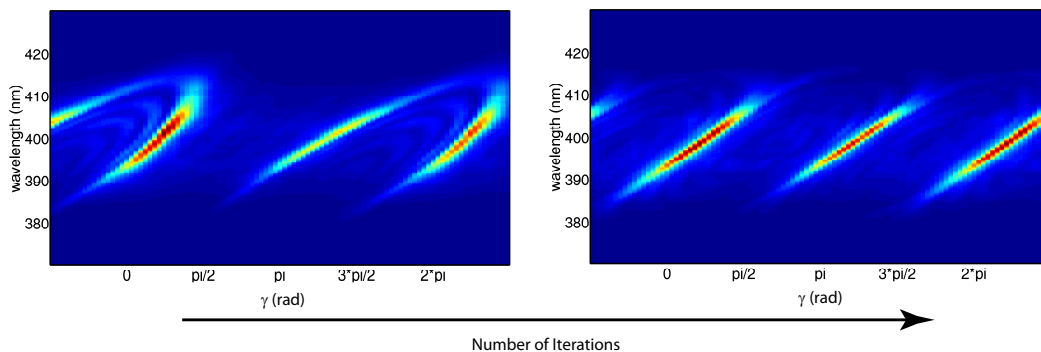


Fig. 3.11 Iterative pulse optimization using MIIPS. SHG spectra recorded for $\text{Fe}_3(\text{IO}_3)_3$ nanocrystals on glass while scanning the phase parameter γ in the phase profile of the shaper $\phi_{MIIPS}(\omega)$. The right image shows the optimized pulse profile for which the unknown phase of the setup has been compensated by the phase determined during iterative MIIPS runs [130].

In the experiments presented in Chap. 9 a sinusoidal reference phase $\phi_{MIIPS}(\omega) = \alpha \sin(\beta\omega + \gamma)$ is used following the procedure described in [130]. The parameter γ was scanned while recording a complete SHG spectrum for each step keeping α and β fixed. The resulting data set forms a two dimensional image of the SHG intensity $SHG(\omega, \gamma)$. The value of $\gamma_m(\omega)$ is found for each frequency from which the second derivative of the unknown phase can be calculated $\phi''(\omega) = -\alpha\beta^2 \sin(\beta\omega + \gamma_m^n(\omega))$. Since there are multiple solutions $\gamma_m^n(\omega)$ the range of γ_m^n needs to be specified [130]. A consecutive phase scan using the derived value for $\gamma_m^n(\omega)$ is performed and the procedure is repeated until the resulting phase correction is below 3 mrad. For transform-limited pulses the traces with strongest SHG signals from parallel lines separated by π are used (Fig. 9.5(right)).

4 Influence of metallic and dielectric nanowire arrays on the photoluminescence properties of P3HT thin films

This chapter is based on the publication: **Influence of metallic and dielectric nanowire arrays on the photoluminescence properties of P3HT thin films** [135]. The optical properties of organic semiconductor thin films deposited on nanostructured surfaces are investigated using time-resolved two-photon photoluminescence (PL) microscopy. The surfaces consist of parallel metallic or dielectric nanowires forming well-defined arrays on glass substrates. Keeping the nanowire dimensions constant and varying only their spacing from 40-400 nm the range of different types of nanowire-semiconductor interactions is studied. For silver nanowires and spacings below 100 nm, the PL intensity and lifetime of P3HT and MDMO-PPV decrease rapidly due to short-ranged metal-induced quenching that dominates the PL response with respect to a possible plasmonic enhancement of optical transition rates. In the case of P3HT however, an additional longer-ranged reduction of non-radiative losses for both metallic and dielectric nanowires is detected that is not observed for MDMO-PPV. Excitation polarization dependent measurements indicate that this reduction is due to self assembling of the P3HT polymer chains along the nanowires. Nanostructured surfaces, when fabricated across large areas, could be used to control film morphologies and to improve energy transport and collection efficiencies in P3HT-based solar cells.

The sample material used for the experiments presented in this chapter were fabricated within a collaboration by the group of Prof. Schmidt-Mende and Philipp Altpeter from the group of Prof. Kotthaus.

4.1 Motivation

Organic polymers find wide application in electronics and opto-electronics due to their flexibility, low cost and non-toxicity, and appealing optical properties. [136]. A large number of polymer-based devices has been developed recently such as solar cells, transistors and organic light emitting diodes (OLED's). For organic solar cell applications P3HT (poly3-hexylthiophene) in combination with PCBM ([6,6]-phenyl C₆₁-butyric acid methylester) has been a standard material for many years, because of its comparatively good charge transport properties and high absorption coefficient (around 10^5 cm^{-1}) in thin films. Photoabsorption in conjugated polymers such as P3HT leads to the generation of singlet excitons with binding energies of 0.3 – 1 eV [137]. To increase the efficiency of these solar cells further and to make them more competitive with inorganic devices a major disadvantage of polymer materials has to be overcome: The short exciton diffusion length on the order of 10 nm that is substantially smaller than the absorption length [138]. Current device designs thus need to balance energy transport and light absorption efficiencies limiting present applications in the case of P3HT to thin films only [139].

Several strategies are currently being investigated that focus either on controlling the film morphology or on enhancing light absorption. Increased polymer chain ordering is expected to improve energy transport properties by ensuring uninterrupted percolation pathways [140,141]. Zhao et al. showed that by combining P3HT with a specially func-

tionalized fullerene electron acceptor and using an optimized annealing treatment, a power conversion efficiency of 6.48% can be reached representing the highest value reported for P3HT-based polymer solar cells at that time [5]. Film morphologies can also be influenced by tailoring the surface chemistry of the metal-oxide electrode [58,142] or by fabricating nanostructured heterojunctions using nanoporous metal films [143,144]. Light absorption, on the other hand, can be enhanced locally by introducing plasmonically active metal nanoparticles or metal nanostructures into the film permitting a considerable reduction in the physical thickness of the absorbing polymer layers [6,145–149].

In this chapter, the influence of parallel aligned nanowires on the PL characteristics of P3HT thin films using time-resolved PL microscopy and spectroscopy is investigated. To separate and identify possible plasmonic effects on the optical transition rates, the PL response for identical array configurations comprising either metallic (Ag) or dielectric (glass) nanowires is compared. Two-photon excitation of P3HT at 800 nm by a pulsed laser source was used to exploit the plasmon resonance of silver at the two-photon transition. The distance dependence of the nanowire-polymer interactions was investigated by varying the nanowire spacing. This approach uses the reduced average nanowire-polymer distance to separate different types of nanowire-polymer interactions and their range. Identical nanostructures using MDMO-PPV (poly(2-methoxy-5-(3'-7'-dimethyloctyloxy)-1,4-phenylenevinylene)) were studied for comparison. For the present silver nanowires, the PL response is observed to be dominated by short-ranged metal-induced quenching rather than plasmonic enhancement of optical transition rates. Surprisingly, P3HT shows a substantial reduction of non-radiative losses for both metallic and dielectric nanowires in case of parallel laser polarization that is not observed for MDMO-PPV. Excitation polarization dependent measurements indicate that this reduction is due to self assembling of the P3HT polymer chains along the nanowires.

4.2 Materials and methods

Nanowires with a width of 100 nm, a height of 40 nm and a length of 10 μm were fabricated in 10 μm x 10 μm arrays on standard microscope glass coverslides by electron-beam lithography. The spacing between the nanowires was systematically varied from array to array between 40 and 400 nm. On top of the structures a thin polymer film of either P3HT or MDMO-PPV was spin-coated from a chlorobenzene solution with a nominal thickness of 60 nm measured by AFM. For all samples the same spin coating procedure with the same volume of polymer solution was used.

Assuming uniform sample height and complete filling of the interwire spacing by the polymer as shown in Fig. 4.1 a). Finally, the samples were top-coated with an PMMA film of 150 nm thickness to reduce oxidation and to increase the photochemical stability of the organic polymers. Fig. 4.1 a) presents a schematic of the sample configuration together with a representative scanning electron microscope (SEM) image in Fig. 4.1 b), showing a silver nanowire array with a nanowire spacing of 120 nm.

Time-correlated single photon counting (TCSPC) was used in combination with confocal microscopy for time-resolved PL measurements. In the studied polymers, PL results from radiative exciton recombination and its intensity is proportional to the product of absorbed fluence and PL quantum yield. The combination of PL intensity and lifetime measurements thus provides access to changes in the excited state relaxation and helps to distinguish radiative and non-radiative rate modifications. Laser excitation was provided by a Ti:Sapphire oscillator operating at a photon energy of 1.55 eV (800 nm), a repetition rate of 76 MHz and a pulse duration of 150 fs. The PL signal was detected at

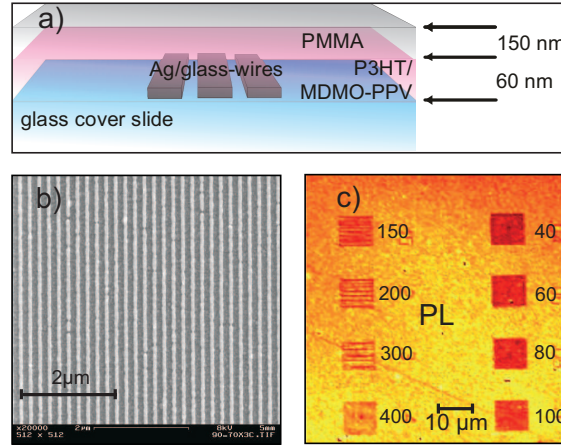


Fig. 4.1 a) Schematic of the sample layout. b) Scanning electron microscope image of an Ag nanowire array. c) PL image of Ag nanowire arrays coated with a P3HT thin film after two-photon laser excitation at 800 nm detected at higher photon energies. The nanowire spacing decreases from 400 nm (bottom left) to 40 nm (top right). Since decreasing nanowire spacing results in a reduced average nanowire-polymer separation, different distance dependent nanowire-polymer interactions can be separated by monitoring PL intensities and lifetimes. The small numbers on the right side of each array indicate the nanowire separation ($x \cdot \text{nm}$).

higher photon energies corresponding to two-photon excitation [150]. Since two-photon transition probabilities scale with the square of the local intensity, they are well suited to study plasmonically enhanced local light fields. Here, the aim is to exploit the plasmon resonance of silver at the two-photon transition.

Laser polarization along and perpendicular to the nanowires is obtained by rotating the sample accordingly. By that procedure signal variations due to polarization dependent optical components in the excitation and detection path were avoided. PL detection is non-polarized in all measurements. The inverted confocal microscope used in epi detection combined with a high numerical aperture objective ($\text{NA} = 1.3$) provides a diffraction limited excitation spot of about 400 nm. Due to the high NA and the associated large angular range of excitation and collection, no significant grating effects on the detected PL intensities and lifetimes is expected. A fast avalanche photo diode (APD) was used to detect PL transients and intensities. The instrument response function (IRF) of the system was independently measured by detecting the scattered pump laser light from the sample and had a full width at half maximum (FWHM) of 27 ps. Due to the high signal to noise ratio achieved in the presented experiments and the reproducibility of the IRF the time resolution of the setup is about 3 ps, close to 10 % of the FWHM of the IRF.

A representative PL image of silver nanowire arrays with different nanowire spacings covered by a P3HT film with a nominal thickness of 60 nm is shown in Fig. 4.1 c). Here the nanowire separation is reduced from down left to up right from 400 nm to 40 nm. To minimize fluctuations due to sample inhomogeneities, PL transients and intensity measurements were performed at several points, typically 30 - 50, within an array of fixed nanowire distance.

4.3 Results and discussion

The PL intensities and lifetimes of P3HT and MDMO-PPV for varying silver nanowire spacing are shown in Fig. 4.2 a) and b), respectively. The intensity data in Fig. 4.2 a) are normalized to the values of the studied planar polymer films measured at short distance away from the arrays where the substrate surface is flat (an example PL image is shown in Fig. 4.1 c)). For both materials the PL intensity decreases rapidly for nanowires spacings below 150 nm reaching nearly zero at about 60 nm (Fig. 4.2 a)). Remarkably, the PL intensity of P3HT peaks at about 150 nm while for MDMO-PPV it decreases monotonously. A corresponding peak at slightly smaller spacings is also seen in the lifetime data for P3HT (Fig. 4.2 b)). The lifetimes observed for MDMO-PPV, on the other hand, are seen to drop rather monotonously carrying large uncertainties due to sample inhomogeneities, faster photobleaching and reduced signal levels in particular for spacings below 200 nm.

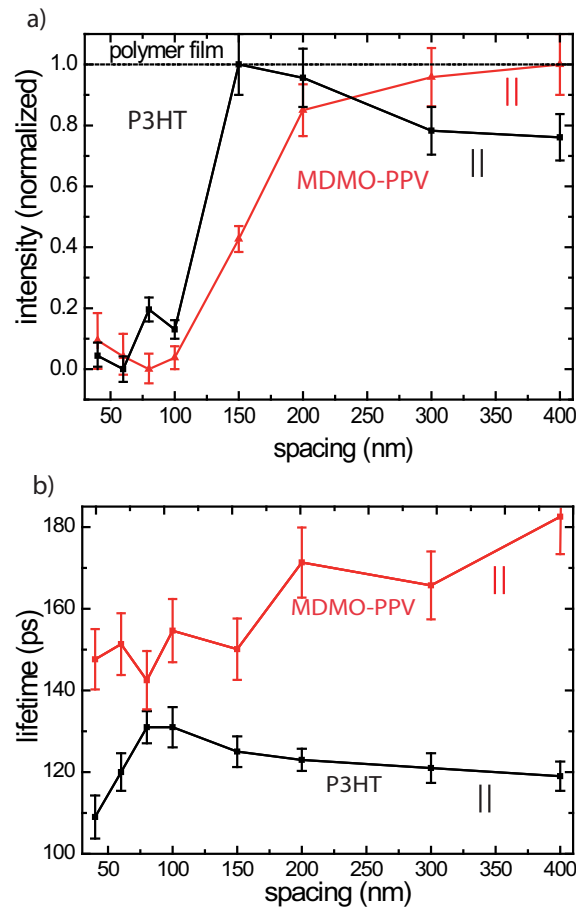


Fig. 4.2 PL intensities a) and intensity-weighted average lifetimes b) recorded for P3HT (black curves) and MDMO-PPV (red-curves) for varying silver nanowire spacing. The PL intensity of P3HT is seen to increase slowly and to peak at about 150 nm while MDMO-PPV shows a continuous decrease for decreasing nanowire spacing. A corresponding trend is observed in the PL lifetimes while the peak of P3HT shifted to smaller nanowire spacing. The intensities in a) are normalized with respect to the intensity measured next to the nanowire array of the respective polymer film. The polarization of the exciting laser light was parallel to the nanowires in a and b.

From the decreasing PL intensities and lifetimes for very small spacing it is concluded that for both P3HT and MDMO-PPV a short-ranged interaction with the metallic nanowires

becomes dominant representing an efficient non-radiative relaxation channel. The slow increase and peak in the P3HT intensity and lifetime data, on the other hand, reveals the presence of an additional longer-ranged interaction mechanism that leads to the reduction of a non-radiative relaxation channel. The origins of these two different types of nanowire-polymer interactions are the subject of the following studies.

The short-ranged decrease of the PL intensity occurring for both polymers can be attributed to energy transfer from the emissive exciton state to the Ag nanowires that is well known from literature for metal substrates (e.g. [151]). To determine the range of metal-induced quenching in the samples, MDMO-PPV and P3HT films of various thicknesses on a thin silver film (≈ 20 nm) were prepared. The results (Fig. 4.3) show that quenching plays a dominant role up to a film thickness of about 40 - 50 nm after which the lifetime observed for pristine polymer films is reached (red line in Fig. 4.3). The lifetimes shown in Fig. 4.3 are intensity-weighted average values that are determined by the interplay between energy transfer within the film and to the metal substrate that is followed by non-radiative decay [151, 152]. The measured PL lifetime of the unstructured P3HT thin film measured on glass for reference is comparable to the values reported in literature and are somewhat shorter than those observed in solution [153–155].

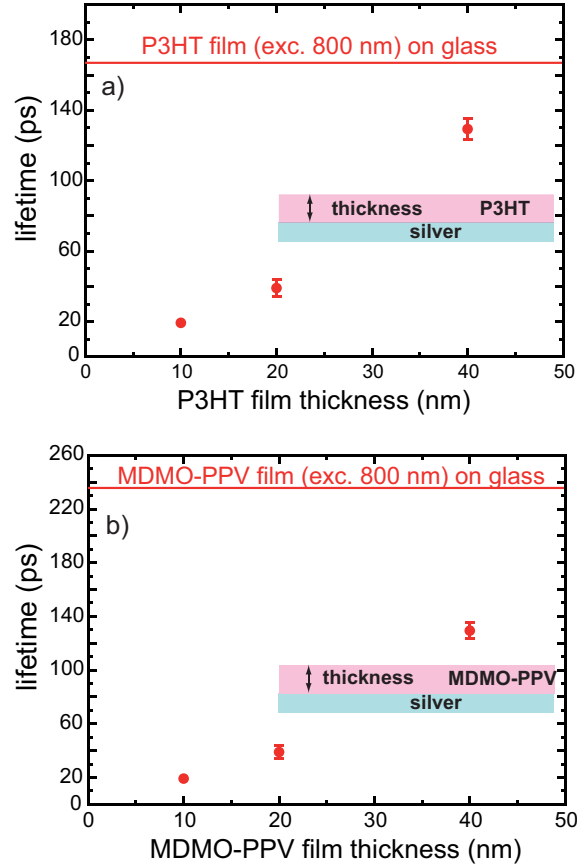


Fig. 4.3 Metal-induced PL quenching studied by varying the thickness of the polymer film deposited on a thin silver layer (20 nm) for a) P3HT and b) MDMO-PPV. Both polymers show efficient metal-induced quenching up to a distance of about 40 - 50 nm.

The longer-ranged increase of the PL intensity and lifetime observed for P3HT in Fig. 4.2 is unexpected. To determine its origin, we first studied the polarization dependence of the PL characteristics. The spacing-dependent PL lifetimes and intensities of P3HT for two orthogonal laser polarizations are shown in Fig. 4.4. To verify the reproducibility of the

features observed in Fig. 4.2, this data has been recorded on a different silver nanowire array sample with the same structural parameters. In Fig. 4.4, the polarization of the excitation laser is changed from parallel (black line) to perpendicular (green line) with respect to the nanowire orientation. For perpendicular polarization, no change in lifetime and intensity can be detected besides the short-ranged metal-induced quenching for separations below 150 nm discussed above. Parallel polarization, on the other hand, results in the same spacing dependence as observed in Fig. 4.2 for the same polarization with somewhat different absolute numbers due to sample-to-sample variations. Note that since at least one nanowire remains in the focal area even for large separations of 400 nm, the PL characteristics obtained for the two polarization directions need not to be the same in Fig. 4.4.

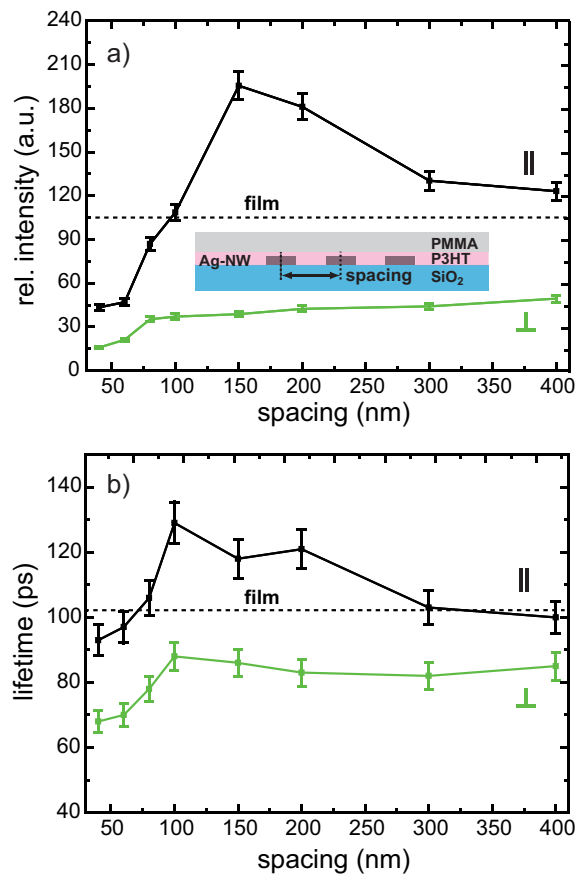


Fig. 4.4 Excitation polarization dependence of PL intensity a) and lifetime b) for P3HT covered silver nanowire arrays with different spacings. The black and green curves have been recorded at the same sample position for parallel and perpendicular excitation polarization with respect to the nanowires, respectively. The PL intensity data obtained for parallel polarization shows the competition between short-ranged metal-induced quenching and a longer-ranged effect that leads to increased PL due to reduced non-radiative losses as can be seen from simultaneously increased decay times. This increase is not observed for perpendicular polarization and is attributed to nanowire-induced ordering of the polymer chains along the nanowires (see text). Note that since at least one nanowire remains in the focal area even for large separations of 400 nm, the PL characteristics obtained for the two polarization directions need not to be the same.

Since the lifetime increases in the presence of the metal nanowire, the radiative rate enhancement is identified as the reason for the increased PL intensity for parallel polariz-

ation. The transition dipole moment of the lowest optical transition in P3HT is parallel to the polymer chain, connecting the thiophene rings. Polarized excitation is thus able to select differently oriented polymer chains within the film. The longer lifetimes observed for parallel excitation indicate that the polymer fraction oriented along the nanowires in close distance feature reduced non-radiative losses. Since no substantial variations are observed for excitation polarization perpendicular to the nanowires, losses are reduced only for polymer chains orientation along the nanowire. From the literature it is known that for P3HT films ordering of the polymer chains reduces non-radiative losses leading to longer lifetimes [141,156]. The longer-ranged increase of PL intensity and lifetime is attributed to nanowire-induced ordering of the P3HT chains along the nanowires.

To test this hypothesis, we first recorded the corresponding PL intensity and lifetime data of MDMO-PPV on Ag nanowires (data not shown). For this material, no substantial polarization contrast is observed. This indicates that either ordering along the nanowires or the correlation between ordering and non-radiative losses is less pronounced for MDMO-PPV that would be expected from literature [157,158].

In the next step and to exclude plasmonic effects induced by the metallic nanowires, identical nanowire arrays but replacing the silver by a dielectric (SiO_2) were fabricated. The polarization dependent PL lifetimes and intensities of P3HT on dielectric nanowire arrays with varying spacings are shown in Fig. 4.5. For parallel polarization (black curve in Fig. 4.5 a)) a substantial increase of the PL intensity is observed upon decreasing nanowire spacing. The range and magnitude of this increase is comparable to the one observed for the metallic nanowire array in Fig. 4.2 a). The simultaneous increase in PL lifetime indicates that the intensity variations are due to modified excited state relaxation dynamics within the film and are not caused by an increased material volume. In addition, a decreased nanowire spacing would rather be expected to reduce the amount of P3HT within the focal volume leading to weaker PL assuming a uniform sample height. The origin of the dip seen in both PL intensity and lifetime data around 100 nm nanowire spacing for parallel polarization is not clear and could reflect sample heterogeneities.

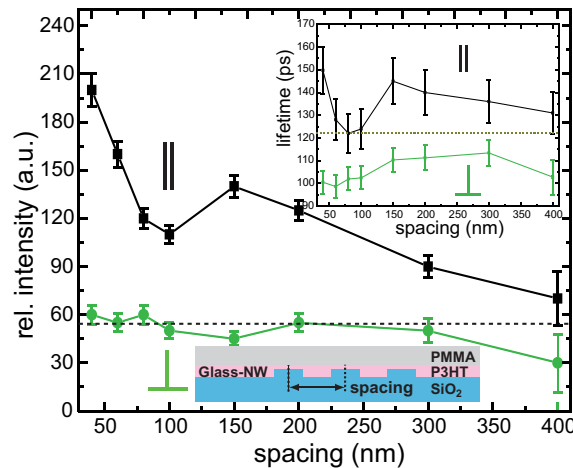


Fig. 4.5 Polarization dependent PL intensity measurement of P3HT on dielectric (glass) nanowire arrays. Black curve represents parallel polarization, while the green curve corresponds to perpendicular polarization with respect to the nanowires. PL lifetimes for both polarizations are shown in the inset. The dotted lines show the PL intensity and lifetime value for the unstructured P3HT film measured close to the structured area. Upon decreasing nanowire spacing both PL intensity and lifetime are seen to increase for parallel excitation polarization that is attributed to ordering of the polymer chains induced by the nanostructured surface (see text).

Importantly, no substantial intensity variations for perpendicular polarization (green curve in Fig. 4.4) are observed as in the metal case for larger nanowire spacings. To conclude, the presented data shows the same range and polarization dependence of the longer-ranged effect for dielectric and metallic nanowires. Its origin can hence not be plasmonic. Instead, these findings support the idea of nanowire-induced ordering of P3HT as the underlying mechanism for the PL and lifetime increase for smaller nanowire separations developed above. Substrate-induced ordering of P3HT has been observed before for samples fabricated by nanoimprint lithography and has been studied theoretically [159, 160].

For the present metallic nanowire structures, no substantial plasmonic absorption enhancement can be deduced from the PL intensity and lifetime data. In particular, no increased PL is observed at any point within the arrays including the nanowires ends that could be expected to act as optical antennas. Due to the complexity of the studied system, that involves intra-film exciton energy transfer, intrinsic non-radiative losses and distance dependent energy transfer to the metallic nanowires, a complete quantitative description or modeling of both PL intensity and lifetime is not feasible. In general, metal-induced quenching appears to be the dominant process as compared to absorption enhancement.

4.4 Conclusion

In summary, the influence of nanowire arrays on the optical properties of P3HT and MDMO-PPV thin films is studied using time-resolved photoluminescence microscopy. Possible plasmonic light absorption enhancement provided by the metallic nanowires is dominated by metal-induced quenching. On the other hand, P3HT films show a pronounced ordering effect induced by both metallic and dielectric nanowires reaching up to about 100 nm distance that leads to a substantial reduction in non-radiative losses that should result in improved energy transfer efficiencies within the polymer film. These findings underline the importance of the film morphology and its control for the optimization of polymer solar cells.

5 The interpenetrated network based photovoltaic device: charge transfer towards the included Fullerene

This chapter is based on **A Photoconductive Thienothiophene-Based Covalent Organic Framework Showing Charge Transfer Towards Included Fullerene** [161] and describes the filling of 3 nm pores in an covalent organic framework (COF) with [6,6]-phenyl-C₆₁-butyric acid methyl ester (PCBM). Since PCBM serves as electron acceptor and the thieno[2,3-b]thiophene-COF (TT-COF) as donor, this architecture is utilized to overcome one of major disadvantages of any polymer based solar cell: the short exciton diffusion length within the organic polymer. This chapter describes the chemical generation of the used TT-COF and the experimental proof that the PCBM completely filled the pores. In the last section of this chapter the working device built out of the nanostructured matrix of TT-COF and PCBM is presented and its efficiency is evaluated as a proof of principle measurement. All presented experiments have been carried out within a cooperation among chemists from the group of Prof. Bein being responsible for sample fabrication and characterization. The time resolved optical measurements proving for the filling of the pores by the polymer were carried out by using the TCSPC method introduced in Chap. 3.

5.1 Motivation

Organic bulk heterojunctions combining electron donor and acceptor phases are of great interest for designing organic photovoltaic devices [162]. While impressive advances have been achieved with these systems, so far a deterministic control of their nanoscale morphology has been elusive. It would be a major breakthrough to be able to create model systems with periodic, interpenetrating networks of electron donor and acceptor phases providing maximum control over all structural and electronic features.

Herein this section reports on a significant step towards this goal on the basis of the recently discovered class of crystalline covalent organic frameworks (COFs) which are created by condensation of molecular building blocks [163–166]. Specifically, the stacked layers of two-dimensional COFs permit charge migration through the framework [167], and several semiconducting structures [168] with high carrier mobilities [166, 169, 170] have been described. COF containing stacked thieno[2,3-b]thiophene-based building blocks serving as electron donors (TT-COF) were fabricated, with high surface area and a 3 nm open pore system. This open framework takes up the wellknown fullerene electron acceptor [6,6]-phenyl-C₆₁-butyric acid methyl ester (PCBM), thus forming a novel structurally ordered donor-acceptor network. Spectroscopic results demonstrate light-induced charge transfer from the photoconductive TT-COF donor network to the encapsulated PCBM phase in the pore system, which represents the first COF-based photovoltaic device with the above mentioned constituents. The organization of the molecular building blocks into a crystalline framework with defined conduction paths provides a promising model system for ordered and interpenetrated networks of donors and acceptors at the nanoscale.

The most prominent hole-conducting material used in organic solar cells is poly(3-hexylthiophene) (P3HT), a thiophene- containing polymer with high charge-carrier mobilities. The soluble fullerene derivative PCBM is often used as an electron acceptor in organic photovoltaics [171]. Because of the lack of structural order in the respective bulk heterojunctions it is very difficult to assess the impact of molecular building blocks, bonding motifs, and energy levels on the microscopic processes involving light-induced exciton formation, charge separation, and transport in such systems. Hence ordered charge-transporting networks with a periodicity of several nanometers are of great interest to understand the details of the light-induced processes and ultimately to obtain design rules for the creation of efficient and stable organic photovoltaic devices [172,173]. The new TT-COF was synthesized under solvothermal conditions by co-condensation of thieno[3,2-b]thiophene-2,5- diyldiboronic acid (TTBA) and the polyol 2,3,6,7,10,11- hexahydroxytriphenylene (HHTP; Fig. 5.1a).

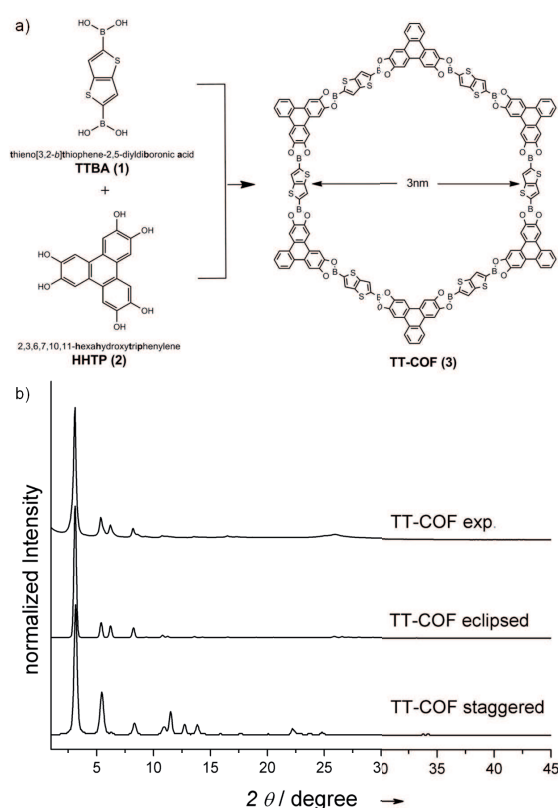


Fig. 5.1 a) Reaction scheme for the co-condensation of TT-COF. b) Comparison of the experimentally observed PXRD pattern (top) with the simulated patterns using the module Reflex of MS Studio in an AA arrangement (middle) and AB arrangement (bottom) (taken from [161]).

5.2 Materials and methods

Detailed information about the material processing is found in [161].

5.3 Results and discussion

As described in the following, the thienothiophene-based COF forms stacks in an AA arrangement, as confirmed by N₂ sorption and powder X-ray diffraction. Powder X-ray diffraction (PXRD) confirms the formation of a highly crystalline COF. Identification of the new structure was conducted by comparison of structures modeled with MS Studio [174].

Corresponding powder patterns were simulated and compared to the experimentally obtained data. For previous COF structures different stacking types of the hexagonal planar sheets were reported [162]. Hence calculations were carried out simulating an eclipsed AA arrangement and a staggered AB arrangement. The experimental PXRD pattern for TT-COF agrees very well with the simulated pattern for an eclipsed AA arrangement (Fig. 5.1b) with a hexagonal P6m symmetry. Moreover, unit-cell parameters determined from the experimental X-ray patterns match very well with those obtained from the structure simulations (peak broadening included). FT-IR spectroscopy can confirm the presence of the newly formed boronate ester functionality. As previously reported, the attenuation of the OH stretching band resulting from the ester formation is apparent, and furthermore the most characteristic modes of the C-B and C-O functionalities can be assigned to the bands at 1395 cm⁻¹ and 1353 cm⁻¹ (see Fig. S8 in [161]) [175]. The 11B MAS NMR spectrum (Fig. S9 in the supporting information of [161]) shows a trigonal-planar boron atom with a chemical shift of δ =21 ppm, which can be distinguished from the starting material (TTBA: δ =15 ppm). Transmission electron microscopy (TEM) images show the nanoscale morphology of the crystals. A slightly tilted side view shows the long ordered channels with distinct pore sizes (Fig. S12 in [161]).

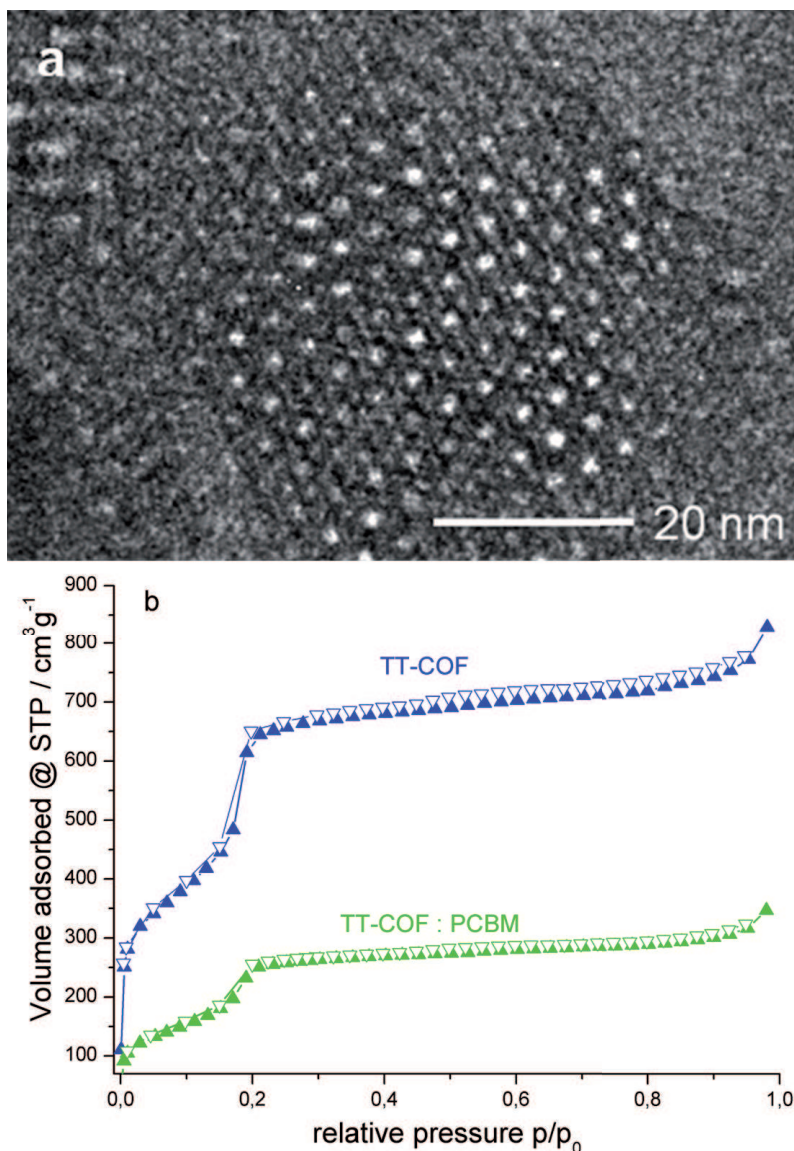


Fig. 5.2 a)TEM micrograph (top view) along the c-axis showing the hexagonal structure of TT-COF. b) Nitrogen sorption isotherm of degassed TT-COF measured at 77 K. Black spheres: adsorption TT-COF, hollow spheres: desorption TT-COF, black triangles: adsorption TT-COF:PCBM, hollow triangles: desorption TT-COF:PCBM (taken from [161]).

A top view along the c-axis shows hexagonal structures with a pore-to-pore distance of around 3 nm (Fig.5.1a)). The morphology identified by TEM can be ascertained by scanning electron microscopy (SEM), which shows small crystals with sizes of about 100 nm that grow into larger arrangement. Based on peak broadening of the PXRD patterns an average domain size of about 30 nm is obtained. The porosity of TT-COF was confirmed with N₂ sorption measurements at 77 K. The obtained type IV isotherm is characteristic for mesoporous materials (Fig.5.2b), and shows a very well-defined jump in the uptake as a result of the highly crystalline mesoporous pore system. The very high Brunauer-Emmett-Teller (BET) surface area was calculated to be 1810 m² g⁻¹ and the pore volume is 1.19 cm³ g⁻¹. Evaluation of the isotherm using the NLDFT-based kernel gives a pore size of 3 nm. The experimentally obtained surface area and pore volumes from the sorption

data were compared to theoretical values obtained with the Connolly method and they are in good agreement (Tab.5.1). In crystalline materials these values can be predicted using geometric methods [176,177]. Based on these results it can be conclude that the pores of TT-COF are not blocked by solvent molecules or by oligomeric fragments.

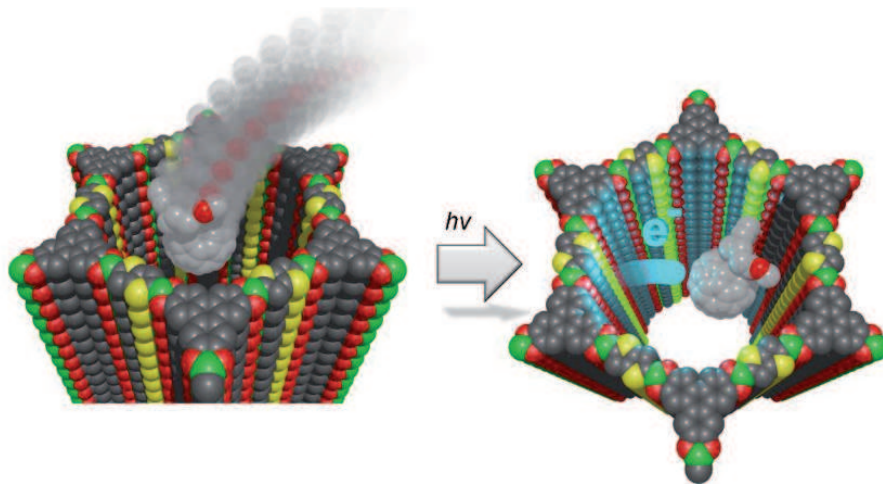


Fig. 5.3 Schematic representation of the host-guest complex of TT-COF and a PCBM molecule to scale (C grey, O red, B green), and S yellow. For clarity only one PCBM molecule is shown, whereas in the experiments described, the COF channels are loaded with the PCBM phase (taken from [161]).

All these results demonstrate that TT-COF is a well defined mesoporous crystalline material with highly organized sheets resulting in high surface areas.

Table 5.1 Theoretical and experimental values for surface area and pore volume of TT-COF

	Pore size [nm]	Surface area [m ² g ⁻¹]	Pore volume [cm ³ g ⁻¹]
TT-COF	3.0	1810	1.19
Connolly	3.0	1810	1.17
TT-COF:PCBM	2.4	700	0.49

Semiconducting polymers based on the thieno[2,3-b]thiophene building block are known and these polymers exhibit high charge-carrier mobilities and are stable under ambient conditions [177]. Moreover, photoinduced charge transfer from polymerized thienothiophene derivatives to fullerene-based acceptor molecules is known [178]. This prompted us to study the electronic interactions between TT-COF and PCBM. The large pores of TT-COF allow for the uptake of the fullerene molecules (because of attractive van derWaals interactions between the host and the guest molecules) and thus for the investigation of the resulting host-guest interaction(Fig. 5.3). Fig. 5.2b) shows a significant reduction of the absorbed amount of nitrogen after loading TT-COF with PCBM. The BET surface area of pure TT-COF decreases from 1800 m² g⁻¹ to 700 m² g⁻¹ for TT-COF:PCBM. Furthermore, the average pore size distribution shows a broad range of pores up to 3 nm (see Fig. S7 in the supporting information of [161]). The pore volume decreases significantly from 1.19 cm³ g⁻¹ to 0.49 cm³ g⁻¹ (Tab. 5.1). Furthermore the amount of PCBM

adsorbed in the TT-COF using UV/Vis spectroscopy is evaluated (see Fig. S17 in the supporting information of [161]). From a 16 mg mL^{-1} PCBM solution in chlorobenzene 1.7 mg PCBM are adsorbed into 5 mg COF.

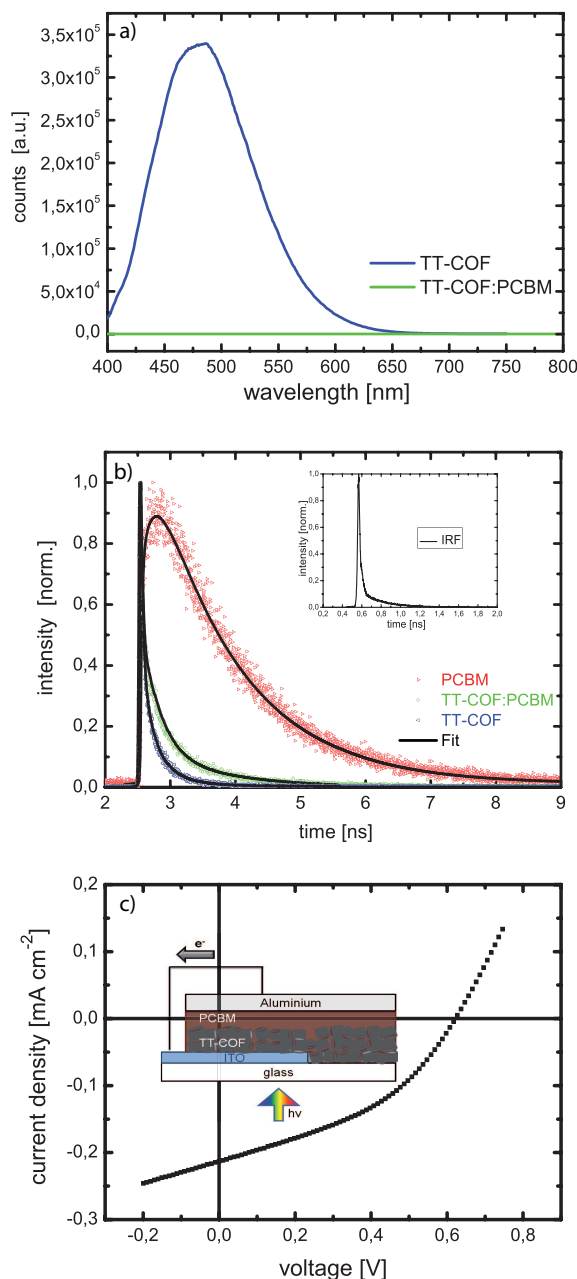


Fig. 5.4 a) Fluorescence emission of TT-COF (blue) upon excitation at $\lambda = 380 \text{ nm}$. The fluorescence of TT-COF filled with PCBM (green) is quenched. b) PL-lifetime transients of PCBM (red symbols), TT-COF (blue symbols) and PCBM:TT-COF (green symbols) thin films using a TCSPC technique under femtosecond pulsed excitation at $\lambda = 800 \text{ nm}$. c) I-V characteristics of the TT-COF-based photovoltaic cell measured under illumination with simulated solar light.

Normalizing the amount adsorbed obtained by UV/Vis measurements to 1 g of TTCOF would give an uptake of 340 mg of PCBM. Thus the pore volume of TT-COF:PCBM should be corrected by the amount of PCBM (a factor of 1.34), and this results in a pore

volume of $0.66 \text{ cm}^3 \text{ g}^{-1}$ of TT-COF. Therefore 0.53 cm^3 of the volume is displaced by PCBM. The calculated density for 0.53 cm^3 PCBM is 0.64 g cm^{-3} , half of the bulk crystal density (1.3 g cm^{-3}), thus indicating that PCBM is not densely packed in the 3 nm pores of TT-COF.

The absorption spectra obtained for thin films of pure TTCOF, TT-COF:PCBM, and PCBM (see Fig. S18 in the supporting information of [161]) confirm the existence of the small thienothiophene and triphenylene units in the framework. The notable optical density over the full visible spectrum is partially caused by light scattering [177]. The fluorescence emission spectrum of TT-COF shows that the framework exhibits a blue emission upon excitation at $\lambda = 380 \text{ nm}$ (Fig. 5.4a). Blue-emissive polymers based on boronate ester condensation have been described by Lavigne et al., and recently the blue-emissive TP-COF has been reported [175]. Once the electron acceptor PCBM is loaded into the TT-COF, the emission band at $\lambda = 487 \text{ nm}$ is completely quenched. In the literature, very efficient light-induced electron transfer on the order of femtoseconds has been reported for PCBM:P3HT blends [178]. In the PCBM:TT-COF system, the photoinduced charges can dissociate at the nanostructured interface between TT-COF and PCBM. In bulk heterojunctions, short diffusion pathways on the order of 10-20 nm are necessary to reach the electron acceptor PCBM within the lifetime of the photoinduced charges [138,139]. Given the ordered nanochannels of the donor material TT-COF, having about 3 nm channel diameter and thin molecular walls, such short diffusion pathways are clearly available in the interpenetrating system PCBM:TT-COF. Therefore the observation of PL-quenching confirms the interpenetrated structure of TT-COF and PCBM. Time-resolved photoluminescence (PL) was studied to learn more about the light-induced interactions between the TT-COF host and PCBM. The PL transients and their respective fit-functions of PCBM and TT-COF loaded with PCBM are shown in Fig. 5.4b).

In the bulk, PCBM shows biexponential PL decay on the nanosecond time scale, while TT-COF decays tri-exponentially with an average lifetime of 117 ps (Tab. 5.1). When included in the channels of TT-COF, the PCBM contribution can be modeled by a single exponential decay component of 1070 ps, which is close to the intensity weighted average lifetime of 1206 ps of the bulk material. Importantly, the decay of TT-COF with a lifetime below 50 ps (46 and 18 ps) is substantially faster than the average decay in the bulk, thus indicating an efficient additional relaxation channel in agreement with the quenching observed in the PL-spectra (see Fig. 5.4a)) [179]. To further explore the capabilities of the TT-COF:PCBM system, a COF film of about $d=200 \text{ nm}$ thickness is incorporated into a ITO/TT-COF:PCBM/Al device structure. Spincoating a rather concentrated PCBM solution on the COF film not only leads to filling of the COF pores, but also produces an overlayer, which ensures that the aluminum top contact does not short-circuit the cell. Under simulated AM1.5G full sun illumination an open-circuit voltage of 622 mV, a short-circuit current density of 0.213 mA cm^{-2} , and 40% fill factor, thus giving rise to a power conversion efficiency of 0.053% (Fig. 5.4c)) is measured¹. Illumination density-dependent I-V measurements (see Fig. S15 in the Supporting Information) prove that the current scales almost linearly with the light intensity. The external quantum efficiency of the device, that is, the number of extracted electrons per number of incident photons, reveals that the majority of the photocurrent is generated from wavelengths below $\lambda = 530 \text{ nm}$, which is in line with the absorption spectrum of the COF film. A maximum EQE of 3.4% is observed at $\lambda = 405 \text{ nm}$. The tail at longer wavelengths exhibits the characteristic feature of PCBM above $\lambda = 700 \text{ nm}$, which indicates that both interpenetrating networks are photoelectrically active. Structural disorder of the donor

¹electrical characterization by F. Auras from the group of Prof. T. Bein

and the acceptor phases can limit charge-carrier mobility and the charge separation in organic bulk heterojunctions and hence can decrease the performance of organic solar cells. The creation of a crystalline semiconducting framework such as a hole transporter whose pores can be filled with the respective acceptor might ultimately overcome these limitations. The novel thienothiophene-based TT-COF described herein exhibits a significant photoresponse. Furthermore, the TT-COF structure is thermally stable and can be handled under ambient conditions. To increase the efficiency of organic solar cells it would be desirable to overcome the disadvantage of the very short exciton diffusion lengths in organic polymers like PCBM, P3HT, or MDMO-PPV.

5.4 Conclusion

The novel interpenetrated TTCOF:PCBM structure realized by M. Dogru from the group of Prof. Bein presented in the sections above supports efficient charge transfer within the lifetime of the excitons. First studies of a COF-based photovoltaic device with an electron donor in the walls and the complementary electron acceptor in ordered periodic channels show that light-induced charge-separation and collection is clearly feasible with these systems. Hence it can be proposed that interpenetrated networks of crystalline porous semiconducting COFs with electron acceptor phases such as PCBM present promising model architectures for the understanding and further development of efficient photovoltaic devices.

6 Increasing crystallinity for improved electrical conductivity of TiO_2 blocking layers

This chapter is based on the publication **Increasing crystallinity for improved electrical conductivity of TiO_2 blocking layers** [180]. The results on the optimization of the TiO_2 blocking layer to improve the efficiency of organic and hybrid solar cells and make them more competitive with standard silicon devices are presented. The major aim of the present work is to increase the electrical conductivity within the TiO_2 blocking layer (BL) to guarantee for efficient charge carrier transport and separation. This is realized by optimizing the calcination processes towards an increase in particle/domain size to increase the unpercolated pathways for charge carriers and to get deeper insight into the morphology of the sol-gel produced films. The sample fabrication and characterization via HR-TEM and REM presented in this chapter were realized by the cooperation partners of the group of Prof. Scheu. Electrical measurements to proof for the influence of the grain size on the charge transport properties of the different films were carried out by 4 probe measurements with and without illumination.

6.1 Motivation

In recent years titanium dioxide thin films have attracted more and more research interest due to their chemical, electrical and optical properties allowing various applications in different fields such as micro-electric devices and solar cells [181]. Especially in solar cells such as dye sensitized or extremely thin absorber solar cells, TiO_2 thin films are applied as blocking layers to prevent short circuiting [182–184]. Numerous studies have shown that the use of a blocking layer has a positive effect on the solar cell performance [185, 186]. Various techniques can be used to grow TiO_2 blocking layers such as electrodeposition [183], magnetron-sputtering [187], chemical vapor deposition, atomic layer deposition [188], chemical spray pyrolysis [189, 190], and the sol-gel method [181, 191]. Many investigations were done on differently prepared films regarding their structure, optical and electrical properties and the influence on solar cell efficiency [135, 190, 192]. Also, experiments were conducted concerning the effect of layer thickness and calcination temperatures on the blocking layer performance [181, 193]. The sol-gel method has some benefits compared to other techniques like controllability and reproducibility and is convenient for the preparation of nano-structured thin films due to nanometer sized sol-particles [194, 195]. This method is cheap, easy to apply and could be processed at low temperatures, which is important for manufacturing multilayered organic solar cells [196]. Different deposition methods on substrates e.g. dip and spin coating can be used [191, 197]. The synthesis of TiO_2 blocking layers prepared via a sol-gel method is reported in literature with different precursors, solvents or catalysts [198, 199]. The effect of different parameters like the pH value of the sol-gel system, catalyst concentration and calcination temperature on the particle size, crystal phase or structure was investigated [181, 198, 200–202]. The TiO_2 blocking layers were synthesized in Anatase modification via a sol-gel method, using a calcination temperature of 450 °C. The deposition on fluorine-doped tin oxide

(FTO) coated glass was done by spin-coating. The strong influence of the dwell time during calcination on the particle size and electric conductivity of the films is demonstrated throughout the experiments presented. The particle size within the obtained Anatase layers was characterized with High Resolution Transmission Electron Microscopy (HRTEM). In addition, the film thicknesses after spin-coating with two different speeds were investigated by Transmission Electron Microscopy (TEM). The electrical conductivity of the blocking layers was studied via I-V measurements.

6.2 Materials and methods

All used chemicals were of analytical grade and used without further purification. Fluorine-doped tin oxide conductive glass (Pilkington) with a dimension of 20 x 15 x 2 mm³ was taken as substrate for the deposition of the TiO₂ films. The FTO was ultrasonicated in a solution of one part extrane and five parts double-distilled water for 15 min. A second ultrasonication was done with ethanol for another 15 min. Afterwards, the substrates were dried with compressed air and treated in an O₂-plasma cleaner for 10 min. For the synthesis of the TiO₂ layers a modified version of the synthesis route of Mandlmeier et al. [199] was used. A highly diluted tetrahydrofuran sol-gel solution was prepared by giving 0.186 ml concentrated hydrochloric acid to 0.275 ml tetraorthoethyltitanate while stirring and diluting the incurred sol-gel solution with 3.5 ml tetrahydrofuran. For the deposition of the TiO₂ layers on the cleaned FTO substrates a spin coater was used. 0.130 ml of the prepared sol-gel solution was given on the FTO substrates. The spin coating parameters were 3000 rpm for 1.5 min leading to thinner films or 1500 rpm for 1.5 min leading to thicker films. After spin coating, the layers were heated up to a temperature of 450 °C at a heating rate of 0.65 °/min, kept at this temperature for 30 (film 1), 60 (film 2), 90 (film 3), 120 (film 4), 200 (film 5) and 300 (film 6) min and then cooled slowly down to room temperature within 11.0 h. The obtained TiO₂ films showed a homogeneous, transparent surface. All films synthesized with different dwell times were prepared with spin coating speeds of either 3000 rpm or 1500 rpm. To characterize the films, different analytical techniques were applied. To get insight into morphology of the TiO₂ according film thicknesses and crystal grain sizes, a FEI Titan 80-300 (S)TEM, equipped with a Gatan Tridiem image filter and an EDAX Energy Dispersive X-Ray (EDX) detector for analytical measurements, was used. Cross-sectional TEM specimens were prepared as described by Strecker et al. [203]. Electron diffraction experiments were performed to determine the crystal phase of the film. The data were evaluated using a calibrated camera constant obtained using a Si standard leading to high accuracy (error less than 2%). To investigate the conductivity of the films, I-V curves were measured with a Keithley source-meter 2636a.

6.3 Results and discussion

TEM measurements were performed to investigate the influence of the different calcination times on the structure of the TiO₂ films prepared at 450 °C and to determine the thickness of the films with different spin coating parameters. Fig. 6.1 shows exemplary TEM bright field images of two films. The bright field images in Fig. 6.1(a) displays film 4, which was left at 450 °C for 120 min and spin coated with 3000 rpm and film 6 (b) left at 450 °C for 300 min and spin coated with 1500 rpm. It can be seen that the films are polycrystalline. The relatively high surface roughness is due to the fabrication process of

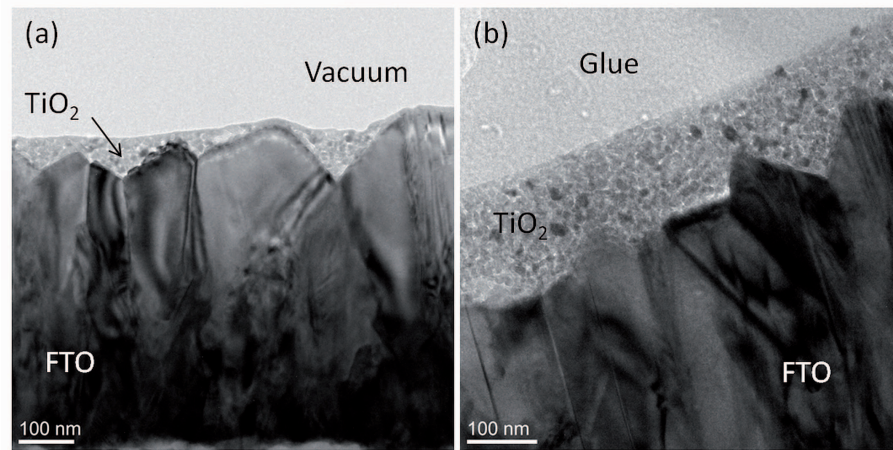


Fig. 6.1 (a) shows a TiO_2 film spin coated at 3000 rpm. The resulting layer thickness is between 14 – 20 nm in thinner regions. The film depicted in (b) was spun at 1500 rpm and increased in thickness by a factor of 4 compared to (a) (taken from [180]).

the FTO substrate (CVD method). In contrast the prepared film shows a flat surface [204]. The local roughness of the FTO substrate was around 50 – 75 nm.

Furthermore, it can be observed that the thinner film (Fig. 6.1(a)) only fills the gaps of the rough FTO surface and exhibits a minimum film thickness of about 14 – 20 nm and a maximum thickness of about 100 nm while the film shown in Fig. 6.1 (b), which was spin coated with 1500 rpm shows a minimum film thickness of about 70 – 75 nm and a maximum film thickness of about 180 nm. This can be attributed to higher spin coating speeds resulting in higher centripetal forces, removing excess material. To investigate the influence of the different calcination times on the grain size in the films HRTEM images were realized. Examples are shown in Fig. 6.2. In Fig. 6.2 (a) film 1, (b) film 2, (c) film 3, (d) film 4, (e) film 5 and (f) film 6 is depicted. All films are polycrystalline, with the crystal grains embedded in an amorphous matrix. An orientation relationship with the FTO substrate could not be found. The analysis of the average grain size of the different films was obtained from cross sectional HRTEM images depicted in Fig. 6.3. They increase from 8.9 ± 0.5 nm to 13.1 ± 0.5 nm for film 1 to film 6.

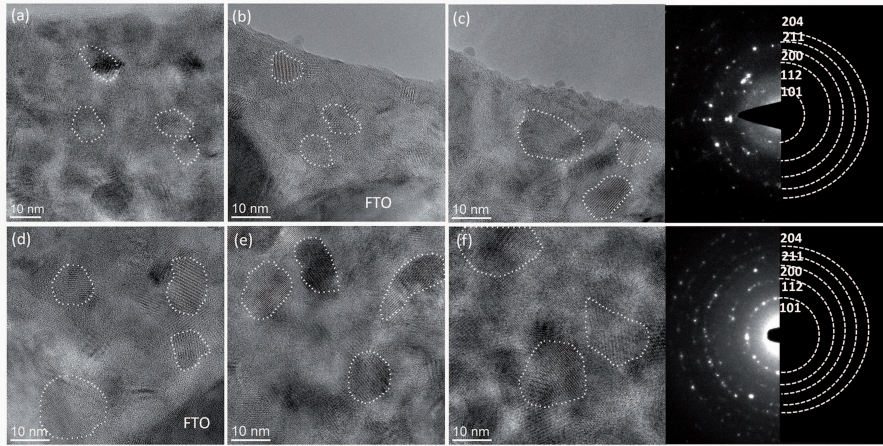


Fig. 6.2 From (a) to (f) the calcination time is increased from 30 min to 300 min. In every HRTEM image some respective particles are labeled by a white ring as a guide to the eye. With increasing calcination time the particle size increases from 8.9 nm to 13.1 nm in average. The diffraction pattern next to (c) and (f) show reflections of TiO₂ in Anatase modification belonging to (101), (112), (200), (211) and (204) lattice planes of film 3 (next to (c)) and film 6 (next to (f)). The patterns were taken with an aperture with a diameter of 150. Here reflections of TiO₂ in Anatase modification belonging to (101), (112), (200), (211) and (204) lattice planes were found. Each film has the same film thickness of ≈ 100 nm (taken from [180]).

These results indicate that longer calcination times lead to increased grain sizes within the films. In Fig. 6.3 the grain sizes are plotted against the calcination times. It can be seen that the grain size in the first four films follows an almost linear behavior, indicating continuous growth. Further investigations of the HRTEM images reveals that the film 1 – 4 show amorphous areas between the grains which are no longer observed in film 5 (calcination time 200 min). This indicates that the crystal grains grow into the amorphous areas explaining the decrease in growth speed at a certain point.

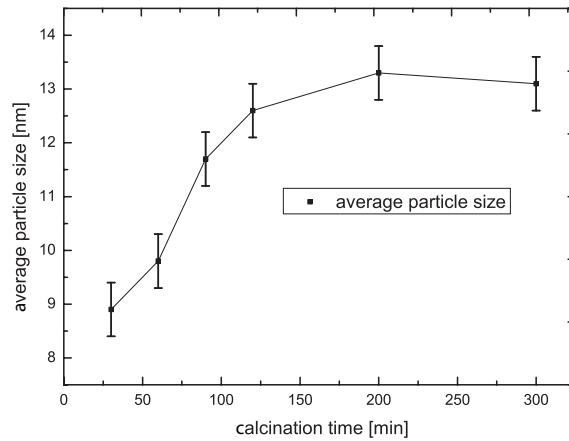


Fig. 6.3 Grain size within the TiO₂ film (14 – 20 nm) increases with calcination time. From 30 min to 120 min an almost linear increase in size with time is visible. The deviation from the linear increase in particle size towards saturation is due to the reduced amount of amorphous areas between the crystal grains (see text).

The diffraction pattern in Fig. 6.2(c)(inset) was taken at film 6 (upper part) and film 3 (lower part) from an aperture of about 150 nm diameter. The pattern proves that the film

is polycrystalline, without a preferred orientation and shows the (101), (112), (200), (211) and (204) reflections of TiO_2 in the Anatase modification. Beside reflections of the FTO substrate no additional reflections related to impurities or other TiO_2 modifications were found. The analysis of the diffraction pattern taken from the films 1 – 6 showed the same results. However, a diffuse scattering in the diffraction pattern of film 3 is observed which is due to the amorphous matrix. To correlate electrical resistance and grain size within the TiO_2 film, I-V curves of films prepared with a spin coating speed of 1500 rpm were measured. Several films from each calcination times were measured. Example I-V curves for different calcination times are displayed in Fig. 6.4. Here the TiO_2 film thickness was kept constant at 180 nm to reduce the risk of creating short circuits by contacting the sample, which were observed regularly in the thin films. The inset in Fig. 6.4 shows the resulting resistance for each calcination time. The extracted resistances correspond with the measured grain size within the film (see Fig. 6.3). With linear increasing grain size the resistance drops also linearly. After a calcination time of approximately 120 – 200 min the minimum value for the resistance is reached. This is exactly where the biggest grain sizes have been recorded (see Fig. 6.3).

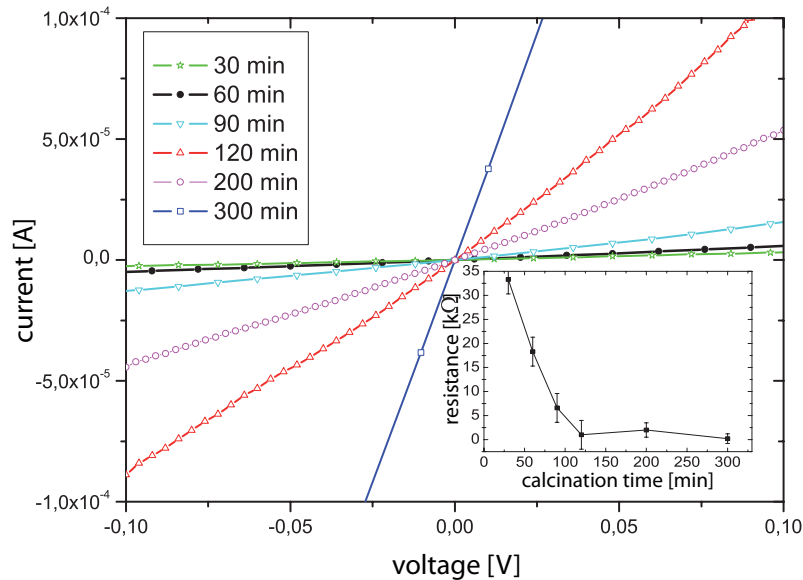


Fig. 6.4 I-V characteristics of different TiO_2 films. Every film consists of the same thickness. The calcination time is increased from 30 min up to 300 min. The inset shows the calculated resistance of each film. Here the resistance drops linearly for calcination times of 30 min to 120 min.

The results show that a longer dwell time at 450 °C during the calcination of the TiO_2 films leads to an increase of the grain size and consequently to an increase of the conductivity. Also the decrease of the amorphous areas in the films can have an influence on the improved conductivity. The findings are in good accordance with quantum mechanical calculations of polycrystalline metallic materials by Reiss et al. [205]. They showed an exponential decrease of the calculated conductivity with respect to the number of grain boundaries per mean free path. Their calculations are in good agreement with an empirical model proposed by Vancea et al. [206, 207] which is based on experimental investigations of Cu, Al, Ag, Au, Ni and Pt films. Sun et al. [193] investigated the effect of the film thickness on the power conversion efficiency of TiO_2 blocking layers of organic solar cells. The TiO_2 layers were synthesized by spray pyrolysis at a temperature of 450 °C. Resistance analysis

of their films revealed that charge transport is not limited even for 500 nm thick films but that the light intensity limits the device's performance. They found an optimal thickness of 100 nm for their investigated solar cells. This thickness is reached at a spin coating speed of 1500 rpm. The conductivity seems not to be influenced by the film thickness but it is found that it can be increased by the calcination time. In conclusion it can be proposed that a higher conductivity of the TiO₂ blocking layers should have a positive influence on the solar cell performance. This should be further investigated in different types of solar cells for example extremely thin absorber, thin film or organic solar cells.

6.4 Conclusion

In conclusion, six different TiO₂ films were prepared with a sol-gel synthesis and deposited on FTO substrates by spin coating and calcinating with varying dwell times (30, 60, 90, 120, 200 and 300 min) at 450 °C. TEM investigations were realized focusing on the grain size, the crystal phase to the FTO. Additionally, investigations on the influence of the spin coating speed on the film thickness were done. Bright field images reveal a thickness of 14 – 20 nm in the thinnest region for films prepared with a faster spin coating speed (3000 rpm) and 70 – 75 nm for films prepared with a slower spin coating speed (1500 rpm). Furthermore these bright field TEM images show a good adaption of the TiO₂ films to the rough surface of the FTO substrate and that they have a flat surface. Electron diffraction experiments reveal TiO₂ in Anatase modification for all films. No reflections which indicate impurities were found. Additionally the electron diffraction pattern indicates polycrystallinity and the presence of an amorphous phase for dwell times ≤ 120 min. The investigations of the HRTEM images show a random orientation without preference of the grains. The analysis of the HRTEM images regarding the grain size in the films with different dwell times yielded in an increase from 8.9 ± 0.5 nm for film 1 (30 min) to 13.1 ± 0.5 nm for film 6 (300 min). Also a decrease of amorphous areas between the grains with longer dwell times can be observed. Following these findings I-V curves were measured to investigate the influence of the grain size on the conductivity of the films. The results show an increase of the particle size with longer dwell time at 450 °C during the calcination and a simultaneously decrease of amorphous areas between the particles up to calcination times of 120 – 200 min. Consequently an increase of the conductivity with an increase of particle size of the layers was observed. After 120 min no significant increase of grain size is detected (Fig. 6.3). An optimum balance between resistance and grain size is reached after 120 – 200 min which leads to an increase in electrical conductivity by a factor of ≈ 150 compared to the shortest dwell time. A calcination time of more than 120 min is proposed to increase the efficiency of organic and hybrid organic solar cells utilizing TiO₂ blocking layer.

7 The influence of blocking layers on the performance of TiO_2 nanowire hybrid photovoltaic device

7.1 Motivation

As a consequence from the results on the influence of ordering of the P3HT molecules (see Chap. 4) and the need of electron donor and acceptor in close proximity (Chap. 5) in combination with the crucial role of the blocking layer (see Chap. 6) on the performance of the resulting photovoltaic device further steps towards the optimization of the photovoltaic device are realized.

In this chapter the combination of the three already realized studies presented in the previous chapters on the performance of organic solar cells is investigated. TiO_2 nanowires were grown on a conductive substrate (fluor tin oxide) and embedded in a thin P3HT film, which was top contacted by silver coating. Two different types of samples, with and without an ALD fabricated blocking layer on the surface of the nanowires were supposed to proof for the influence of the blocking layer. The resulting influence of ordering and improved charge transfer within the organic polymer is investigated using time resolved PL spectroscopy, while the difference in morphology of the used materials is made visible by high resolution TEM (HR-TEM) imaging. This project was realized in a cooperation of the group of Prof. Christina Scheu, Prof. Lukas Schmidt-Mende and Prof. Thomas Bein being responsible for HR-TEM imaging, sample preparation and the I-V measurements under standard illumination.

7.2 Materials and methods

Free standing TiO_2 nanowires on an fluor tin oxide (FTO) covered substrate were embedded in P3HT like schematically shown in Fig. 7.1. The top electrode was realized by a thin silver contact on the surface of the P3HT film. The blocking layer ensuring for charge carrier transport from P3HT towards the electrode and preventing the system from short circuiting was fabricated by atomic layer deposition (ALD) from pristine TiO_2 .

Charge separation occurs at the TiO_2 /P3HT interfaces. The blocking layer of compact TiO_2 prevents holes in the polymer from reaching the conductive oxide. A key advantage of the TiO_2 nanowire array electron-accepting network is that it prevents the electron-donating material (P3HT) and electron-accepting materials TiO_2 from both being in contact with anode and cathode of the resulting device.

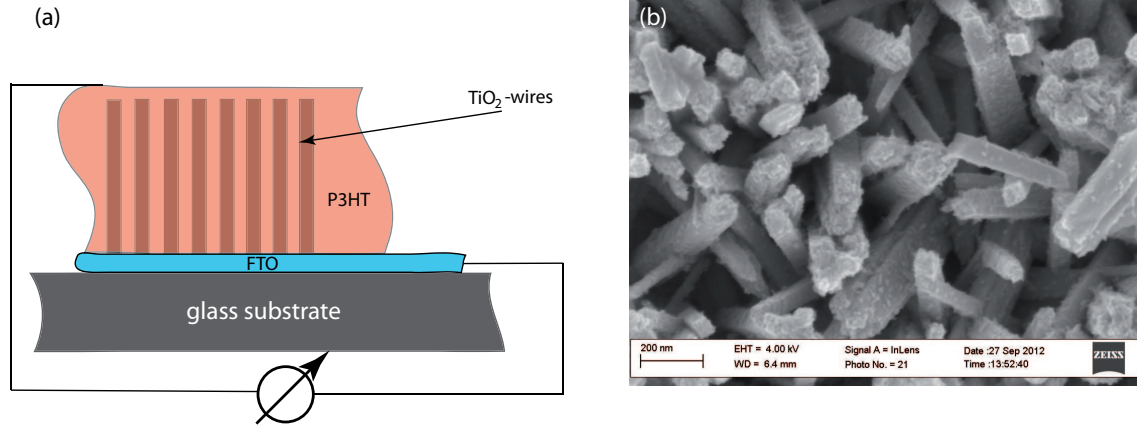


Fig. 7.1 (a) Is showing a sketch of the sample layout. Vertical free standing TiO₂ nanowires of an average diameter of ≈ 65 nm and a length of 800 nm are embedded in P3HT. The top contact is realized by a thin silver film, while the thin FTO layer serves as the bottom electrode. Figure (b) shows a SEM image of the grown nanowires. They are randomly distributed regarding their distance, but pointing mainly upwards.

An additional effect of doping the nanowires was tried to realize by rinsing the pristine TiO₂ wires in TiCl₄ solution. Since detailed respective energy dispersive X-ray spectroscopy (EDX) studies have proven for the lack of any doping effects this sample material is estimated to be intrinsic without blocking layer Fig. 7.3. The corresponding electron diffraction pattern is depicted in Fig. 7.3 b). The detailed analysis of the respective EDX data to extract information about the constituents of the wires and the blocking layer is shown in Fig. 7.3 h). This analytical procedure showed no significant differences of both sample types. To further estimate the influence on the performance of the blocking layer on the resulting device the thickness of the respective ALD-fabricated layer was varied from 4 to 8 nm.

Time-correlated single photon counting (TCSPC) was used in combination with confocal microscopy for time-resolved PL measurements presented in this chapter. In P3HT, PL results from radiative exciton recombination and its intensity is proportional to the product of absorbed fluence and PL quantum yield. The combination of PL intensity and lifetime measurements thus provides access to changes in the excited state relaxation and helps to distinguish radiative and non-radiative rate modifications. Laser excitation was provided by a Ti:Sa oscillator operating at a photon energy of 1.55 eV (800 nm), a repetition rate of 76 MHz and a pulse duration of 150 fs. The PL signal was detected at higher photon energies corresponding to two-photon excitation [135, 150]. This was due to the lack of laser sources operating at the one-photon transition energy and had no further physical motivation.

7.3 Results and discussion

The efficiency η of a resulting device is calculated by:

$$\eta = \frac{P_{max}}{P_0} = \frac{V_{oc} J_{sc} FF}{P_0} \quad (7.1)$$

Here V_{oc} represents the open circuit voltage, J_{sc} the short circuit current and FF is supposed to be the fill-factor. To investigate the morphology of the blocking layers at first scanning electron microscopy images at different magnifications were compared

(see Fig. 7.2). From there it becomes clear that nanowires have a length of approximately 800 nm and an average diameter of 65 ± 12 nm.

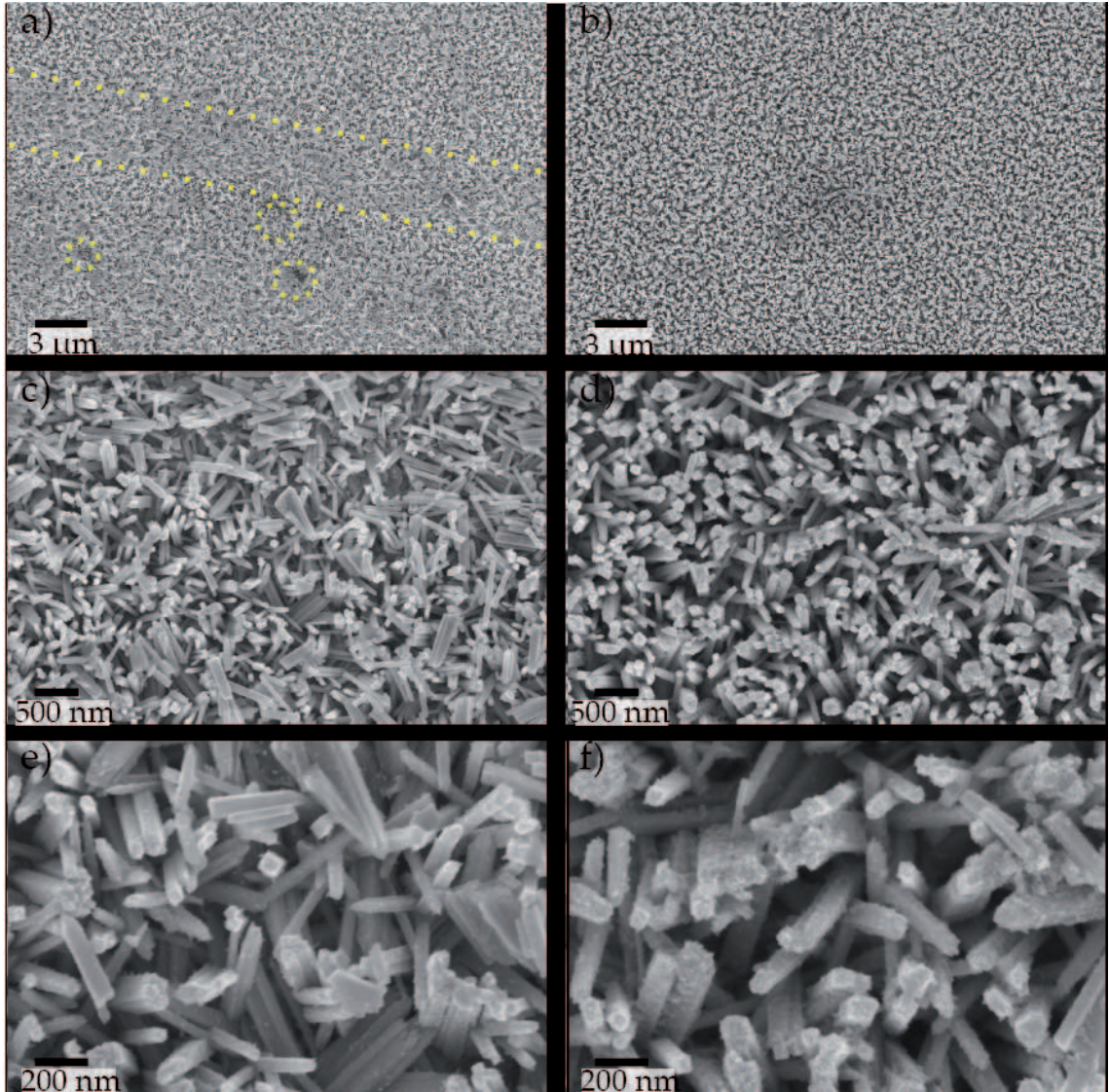


Fig. 7.2 SEM micrographs of TiO_2 (a, c, e) and $\text{TiO}_2 8 \text{ nm}$ (b, d, f) at different magnifications: 10000x (a, b), 50000x (c, d), 150000x (e, f). The yellow dotted line in a) highlights some special morphology features, which do not influence the electro-optical properties.

To gain further insight into the morphology of the resulting blocking layer detailed TEM studies were carried out. In Fig. 7.3 a) the respective TEM image of a single TiO_2 nanowire is shown. In this image the wire-like structure within the amorphous matrix can be seen, while the dashed yellow circle indicates the area used for the detection of the EDX spectra to check for significant doping effects triggered by the fabrication method mentioned above.

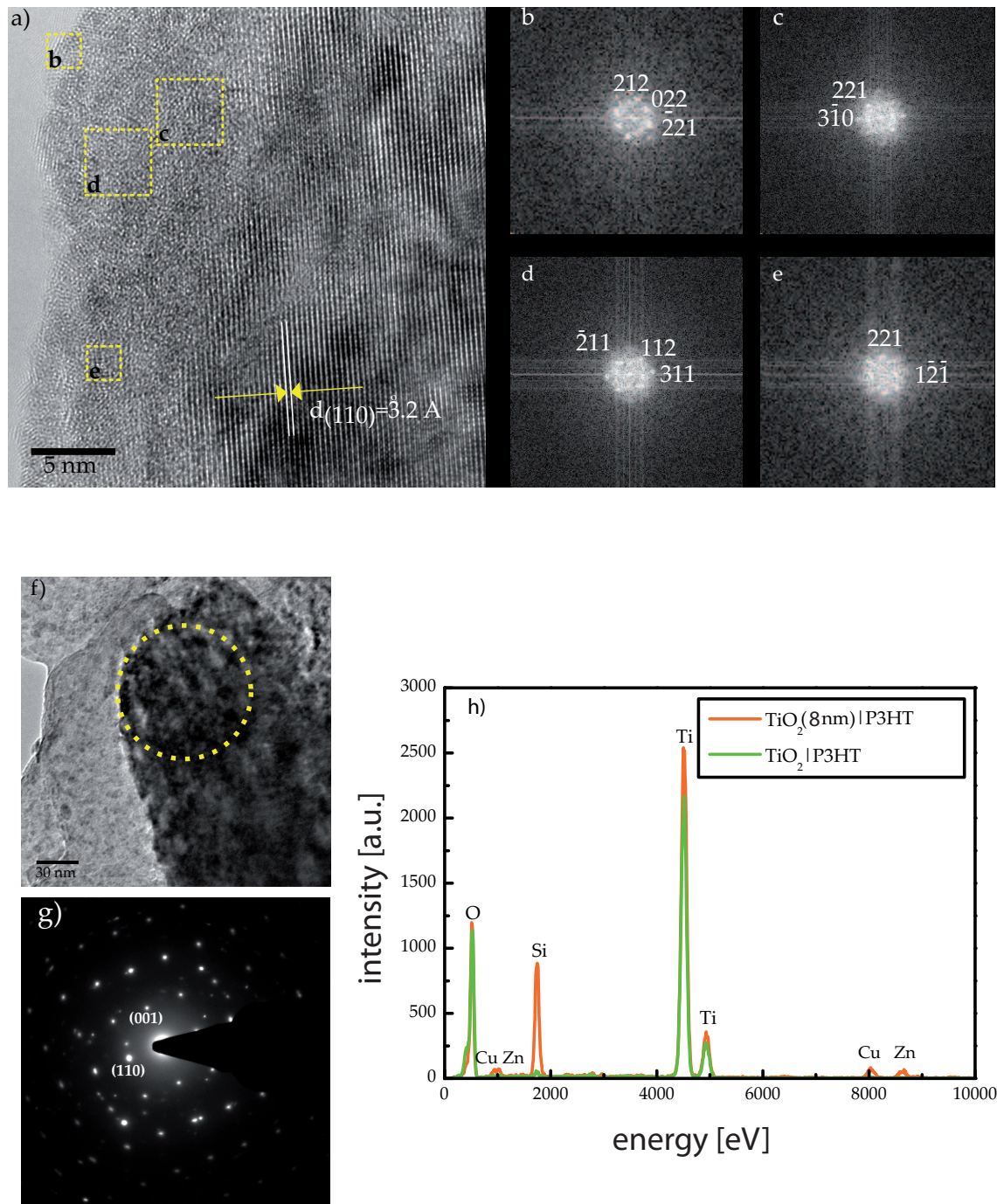


Fig. 7.3 a) HR TEM micrograph of TiO₂/P3HT with a rutile TiO₂ core and a semi-crystalline shell. The yellow dashed lines highlight some of the crystalline parts. They are analyzed calculating the respective FFT. The resulting, indexed FFTs are shown in b-e. Image f) shows the TEM micrograph of TiO₂(8 nm)/P3HT and g) the corresponding electron diffraction pattern. The dashed yellow circle in g) highlights the irradiated area for the EDX measurement visible in h). This EDX spectra of TiO₂(8 nm)/P3HT (orange) and TiO₂/P3HT (green) are almost equal and clarify that both sample types consists of the same constituents. The unlabeled peak around 4.8 keV matches with no element and might be a superposition of others.

The TEM image shown in Fig. 7.3 f) of the imaged wire consists of a highly crystalline core surrounded by a semi-crystalline shell. The measured (110)-plane of the rutile TiO_2 core is (Fig. 7.3 f)) 3.2 Å and in good accordance to the values reported in literature [208]. Since the crystalline areas are very limited in size the FFT patterns of these areas were calculated, which show different orientations characteristics (compare Fig. 7.3 b-e). These findings further clarify that the blocking layer and the wire consists only of TiO_2 which is in good accordance to the previously discussed EDX results. Another remarkable result of the HR-TEM analysis is that the blocking layer and the core of the wires consists of rutile crystal structure. While the sample without the blocking layer is found to show mainly brookite formation within the capping layer (few nanometers).

To further investigate the influence of the blocking layer the light to energy conversion efficiency is measured. This is realized by recording the I-V characteristics during light exposure of each sample material. Here P_0 used for the measurements shown in Fig. 7.4 is equal to 1 sun or AM1.5 G spectrum [209]. This standard procedure is used to allow for comparable results.

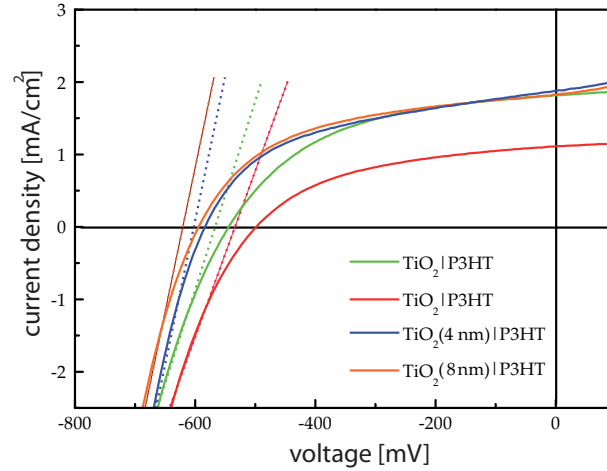


Fig. 7.4 J - V -curves of four different types of solar cells: $\text{TiO}_2|\text{P3HT}$ (green and red), $\text{TiO}_2(4 \text{ nm})|\text{P3HT}$ (blue) and $\text{TiO}_2(8 \text{ nm})|\text{P3HT}$ (orange). The slope of the dotted lines is an indication for the series resistance within the system.

The corresponding I-V curves under standard illumination of 1 sun are shown in Fig. 7.4. With this data and Eqn. 7.1 the efficiency of each sample is extracted leading to the values shown in Tab. 7.1.

Table 7.1 Characterization of the used solar cells: η , FF , J_{sc} and V_{oc} of $\text{TiO}_2|\text{P3HT}$, $\text{TiO}_2(4 \text{ nm})|\text{P3HT}$ and $\text{TiO}_2(8 \text{ nm})|\text{P3HT}$

	η [%]	fill factor [%]	J_{sc} [mA/cm ²]	V_{oc} [mV]
$\text{TiO}_2(4 \text{ nm}) \text{P3HT}$	0.527	48.1	1.877	584
$\text{TiO}_2(8 \text{ nm}) \text{P3HT}$	0.548	50.4	1.830	594
$\text{TiO}_2 \text{P3HT}$	0.478	48.4	1.815	544

The most important electrical parameter depending mostly on optical parameters of the device is the short current density J_{sc} . This value is a direct indicator for the amount of absorbed light within the photovoltaic device. The absorption is a material parameter and is mainly triggered by the amount of the used polymer. The slight variations of efficiency TiO₂(4 nm)|P3HT, TiO₂(8 nm)| P3HT and TiO₂|P3HT might be due to small variations in charge carrier collection efficiency of the different blocking layers. The open circuit voltage V_{oc} is determined by the energy difference between the HOMO Level of P3HT [210] and the valence band of the TiO₂. The fill factor FF depends on the resistance of the device. The slope of the recorded I-V curves shown in Fig. 7.4 dotted lines varies indicating a lower series resistance of the samples containing the nanowires covered by the ALD fabricated blocking layer.

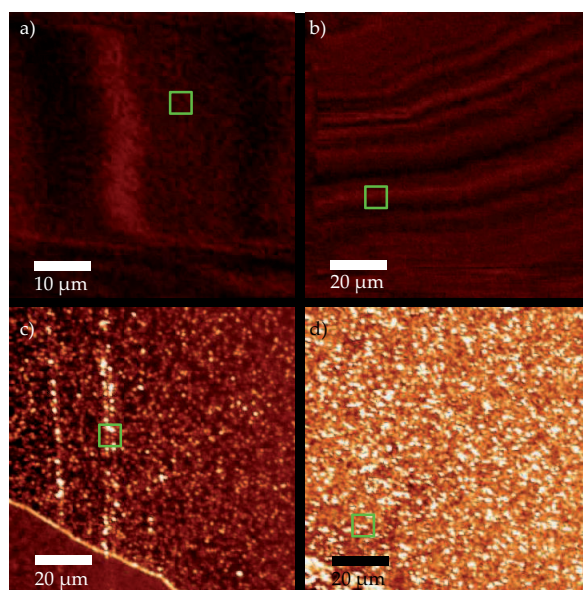


Fig. 7.5 PL images of four different types of solar cells: a) TiO₂|P3HT, b) TiO₂|P3HT c) TiO₂(8 nm)|P3HT with an interface to the silver contact at the lower left and d) TiO₂(4 nm)|P3HT. The green mark indicates the spot, which was used for time-resolved PL measurements. The PL-intensity of the samples with ALD-fabricated blocking layer is ≈ 10 times higher (samples have not been electrically contacted). All presented measurements are equally scaled.

In P3HT the PL results from radiative exciton recombination and its intensity is proportional to the product of absorbed fluence and PL quantum yield. As a consequence the combination of PL intensity and lifetime measurements provides access to changes in the excited state relaxation and helps to distinguish radiative and non-radiative rate modifications. This procedure is intended to be a versatile tool to further investigate the influence of the blocking layer on charge carrier transport. At first the PL-intensity of each device is mapped (see Fig. 7.5). It is remarkable that the PL-intensity of the samples consisting an ALD fabricated blocking layer is ≈ 10 times higher than of the devices without blocking layer. By electrically contacting the device the PL-intensity dropped significantly due to efficient carrier transport (data not shown). The four PL spectra (see Fig. 7.5) show a strong emission from 600 nm to 700 nm, which corresponds to a photon energy of 1.8 eV and is in good accordance with PL spectra reported in literature [211–214]. Although all solar cells emit in the same range, the PL spectra show an additional shoulder around 650 nm (see Fig. 7.6 indicated by arrows). This feature is attributed to interchain coup-

ling between the P3HT chains. As interchain coupling occurs only in ordered P3HT, the shoulder is an indication for highly ordered P3HT areas within this type of solar cell. The correlation of highly regioregular P3HT and a red shift of the 0-0 PL was also shown in the work of Baghgar et al. and Yamagata et al. [215,216]

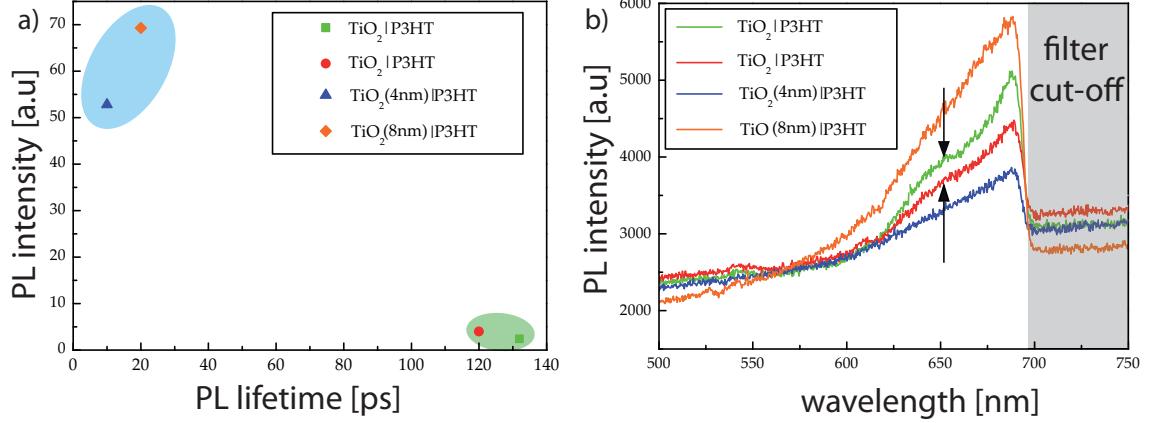


Fig. 7.6 a) averaged PL intensities and intensity averaged PL lifetimes of four different types of solar cells: TiO₂|P3HT (green and red), TiO₂(4 nm)|P3HT (blue) and TiO₂(8 nm)|P3HT (orange). The graph b) shows PL spectra of four different types of solar cells from 500 nm to 750 nm obtained from a line scan over the sample: TiO₂|P3HT (green and red), TiO₂(4 nm)|P3HT (blue) and TiO₂(8 nm)|P3HT (orange). The arrow indicates a shoulder, which is typical for ordered P3HT areas.

The underlying charge carrier relaxation process causing the PL-intensity variations is further investigated utilizing the already introduced time-correlated single photon counting (TCSPC) technique (for technical details see Chap.3). The recorded intensity weighted PL-intensity decay times were recorded while raster-scanning the sample surface to guarantee for reliable values due to averaging (see Fig. 7.6 a)). The lifetime values were extracted by bi-exponentially fitting of the PL-decay like described in Chap.4. This photoluminescence lifetime information support the PL-intensity findings described above, since the PL-decay time τ of the devices with blocking layer is ≈ 6 times faster than the lifetime of the samples without blocking layer (close to the reported lifetime for the pristine P3HT-film [135]). PL-intensity and lifetime analysis (Fig. 7.6) showed significant variations between both sample types. The samples with blocking layer (rutile) showed a reduced PL-lifetime and an increase in PL-intensity compared to the samples without blocking layer. The data in Fig. 7.6 can be interpreted as follows: The increase in PL-intensity of the sample is due to the reduction of non-radiative losses within the material. This might be due to the higher tendency for self-induced ordering of P3HT or by improved electrical transport properties within this sample type. Induced by the synthesis brookite consists of porous aggregates and a higher surface area, resulting in a major difference of rutile and brookite formation. This is the relatively low surface area material of rutile formation compared to brookite. The resulting flatness of the rutile blocking layer supports on one hand side the self-induced ordering effects and with that the amount of ordered polymer chains and on the other hand supports the electrical transport within the sample. From the literature it is known that for P3HT films ordering of the polymer chains lead to longer PL-lifetimes [141,156]. This contradicts the described findings. To fully explain the present data other effects have to be considered. On the rough surface of the nanowires of brookite formation the density of trapped states is significantly higher leading to lower

lifetime [217]. This effect competes with the increase in lifetime due to self assembling of molecules leading to the resulting values of 15 – 20 ps visible in Fig. 7.6.

7.4 Conclusion

This work underlines the significant role and influence on the performance of hybrid solar cells on the used blocking layer. It is shown by electrical transport measurements and time resolved optical studies that an ALD (rutile formation) fabricated blocking layer improves the electric transport properties and the charge carrier separation efficiency. From the combination of the self induced ordering of the P3HT molecules along the nanowire axis presented also in Chap. 4 and the improved electrical transport properties by the design of the blocking layer and short distance sequential stacking of electron donor and acceptor future device designs can benefit.

8 Non-linear photoluminescence from graphene

8.1 Motivation

Since graphene is known to be a zero gap semiconductor the strong photoluminescence signal discovered in 2010 by several research groups [73–75,218,219] was rather unexpected by the community. In this year the non-linear photoluminescence (NL-PL) from single and multilayer graphene flakes after femtosecond laser excitation was explained by two competing models. The first model explaining this remarkable effect was the so called two temperature model put forward by T. Heinz and his co-workers [73,220] based on Planck’s law treating the system a black body radiation emitter. Here the NL-PL effect is explained by two different regimes with respect to time and temperature [221,222], while the second model identifies intraband Coulomb scattering of electrons as the underlying responsible mechanism for the spectral broadening the NL-PL of graphene [74,75,218]. In this section the NL-PL of exfoliated kish graphene flakes is experimentally demonstrated. Therefore the obtained spectra were recorded after femtosecond laser excitation. The influence on the NL-PL intensity and spectra of varying excitation energy and power is investigated by recording the broadband NL-PL spectra.

8.2 Materials and methods

Exfoliated kish graphene flakes are transferred onto a thin glass substrate (thickness $\approx 150\ \mu\text{m}$) by the PMMA transfer method by the group of Prof. Ferrari [16]. The optical response after femtosecond laser excitation of the resulting sample material is investigated by the use of a confocal laser scanning inverted optical microscope (see details in Chap. 3).

8.3 Results and discussion

The respective confocal NL-PL image of single an bi-layer graphene after femtosecond laser excitation detected at wavelengths larger than 860 nm is shown in Fig.8.1. Since intrinsic graphene is semi-metal or a zero gap semiconductor consisting of highly linear band structure without any band-gap [223] the effect of the broadband NL-PL arised unexpectedly to the community.

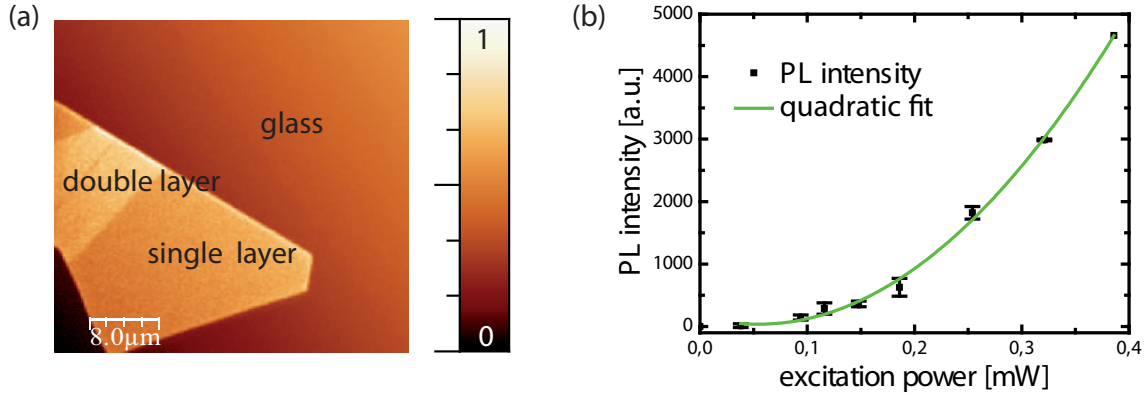


Fig. 8.1 NL-PL image of a graphene flake on a glass substrate recorded in epi-detection with a confocal laser scanning microscope after pulsed excitation at 800 nm detected at wavelengths longer than 860 nm in a). The relatively high background on glass is due to residual laser scattering. In the lower left part of a) a thick graphite flake is visible which appears dark [75]. Figure b) shows the almost quadratic dependency of the PL-signal of graphene on the excitation power (almost quadratic (2.14) fit represented by green line) and is further explained in Eqn. 8.1.

To further understand this non-linearity of the detected signal the simplified rate equation has to be considered [224]:

$$\frac{dn(E)}{dt} \approx \gamma_1(E) \cdot (\alpha_0 I_0)^2 - \gamma_2(E) \cdot (\alpha_0 I_0) \cdot n(E) - \gamma_3(E) \cdot (E) \quad (8.1)$$

In Eqn. 8.1 the first two terms represent the generation and depletion rate of $n(E)$ due to scattering of excited carriers, while the last term is due to relaxation processes independent of I_0 . The generated holes are described equally. Since the excitation pulse duration is much longer than the recombination time [218] the signal strength L_ω is properly described by [225]:

$$L(\omega) \propto \left[\frac{\gamma_3^{-1}(E) \gamma_1(E) \alpha_0^2 I_0^2}{1 + \gamma_3^{-1}(E) \gamma_1(E) \alpha_0 I_0} \right]^2 R_r(\omega) \quad (8.2)$$

Here $R_r(\omega)$ represents the radiative recombination rate. From Eqn. 8.2 it is clear that the signal strength L is proportional to $\approx I_0^4$ for relatively low excitation power I_0 . In case of high excitation power the signal strength in Eqn. 8.2 is proportional to I_0^2 [224].

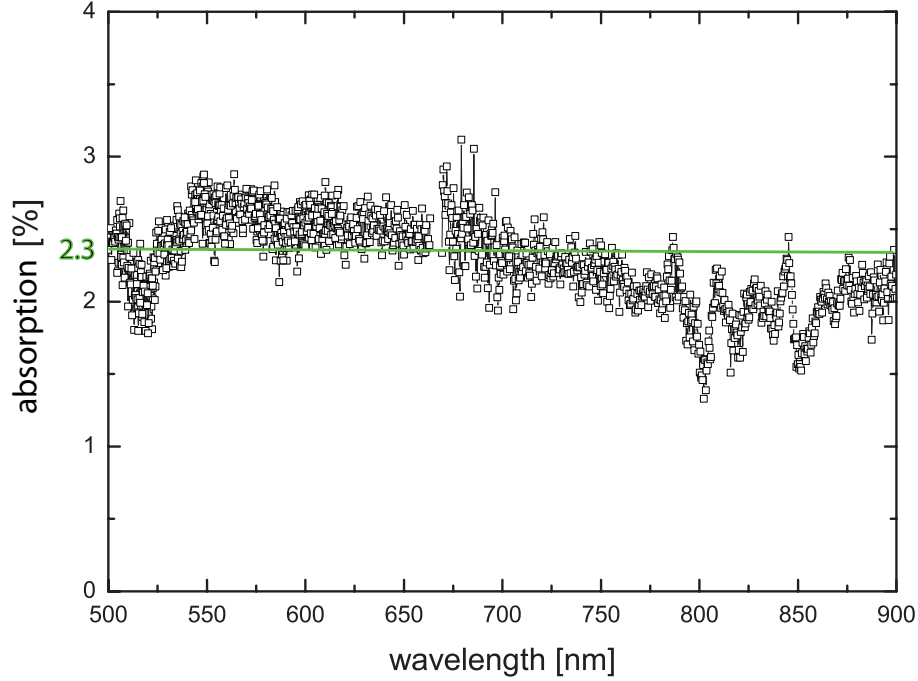


Fig. 8.2 The well known absorption of $\approx 2.3\%$ of a single layer graphene recorded from 500 – 900 nm. The data was recorded using the continuum white light source described in Chap. 3 by extracting $I_{\text{glass}} - I_{\text{graphene}}/I_{\text{glass}}$. The data corrected for the detection sensitivity (also see Chap. 3).

Due to the linear electronic bands crossing at the Fermi-level graphene absorbs across the whole visible and IR range almost equally 2.3% [75, 226]. Treating every graphene layer as a single emitter consisting of a certain refractive index the NL-PL intensity as a function of number of layers can be calculated summing up Fabry-Perot like reflections of different interfaces. Up to 10 layers the NL-PL intensity is found to increase almost linearly, saturates up to 20 layers and drops from a further increase of the number of layers on [75]. This explains the visual contrast in Fig. 8.1 for thick and thin graphene flakes. With that knowledge the NL-PL from graphene on certain substrates is used to identify the thickness of investigated graphene and graphite flakes. Here the detection on the blue-side with respect to the excitation beam is necessary to avoid the influence of non-linear effects (i.e impurities, dopants,...) [75].

Raman spectroscopy is another powerful tool to identify graphene on different substrates [61, 62, 227–234]. This data allows for the detailed analysis of the graphene flake, such as thickness, impurities, mechanical deformation and many others. From the recorded Raman spectra of the used exfoliated kish graphene and multi-layer graphene the material is identified to be intrinsic without any significant dopants or impurities. The corresponding Raman spectra is shown in Fig. 8.3. For detailed analysis the ratio of absolute intensity of 2D and G band and the FWHM of each band has to be considered [228].

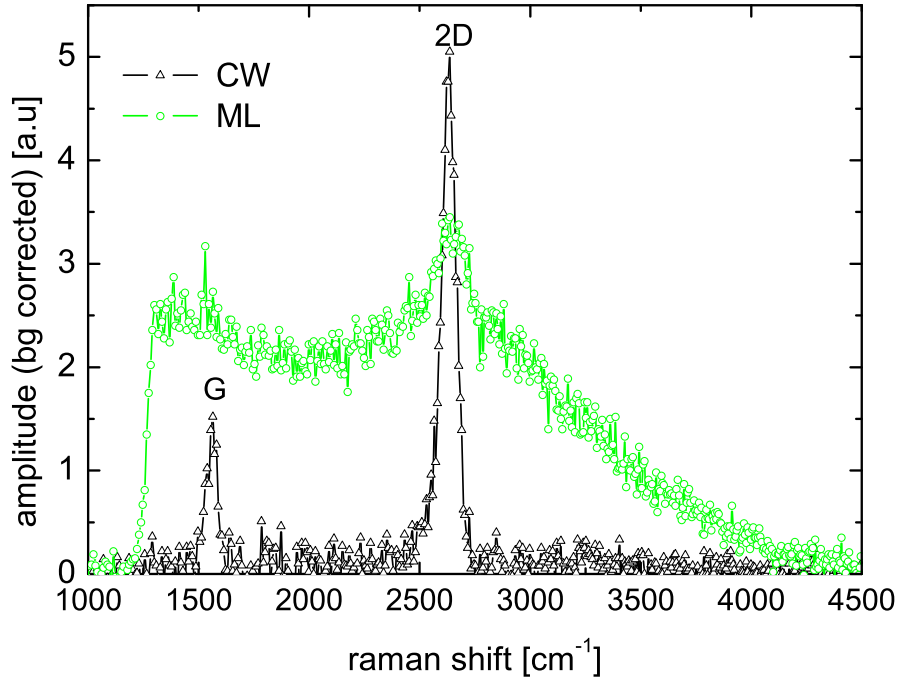


Fig. 8.3 Raman and PL-spectra obtained for modelocked and continuous wave laser excitation of single layer graphene at a center wavelength 800 nm.

By switching the exciting Ti:Sa oscillator from continuous wave (CW) to mode-locked (ML) the uprising photoluminescence signal from graphene is clearly seen (green in Fig. 8.3). To investigate the origin of the NL-PL further the power dependence of the excitation on the spectral response of the photoluminescence of graphene is recorded (Fig. 8.4 a)). The graphene was therefore excited at 690 nm with femtosecond laser pulses (duration ≈ 150 fs) and the signal was detected at wavelengths longer than 700 nm. Despite the change in amplitude (discussed in previous text and in Eqn. 8.2) the spectral characteristic of the NL-PL is not influenced by the excitation power. The small peak-like structures at 780 nm are due to Raman scattering as visible in Fig. 8.3.

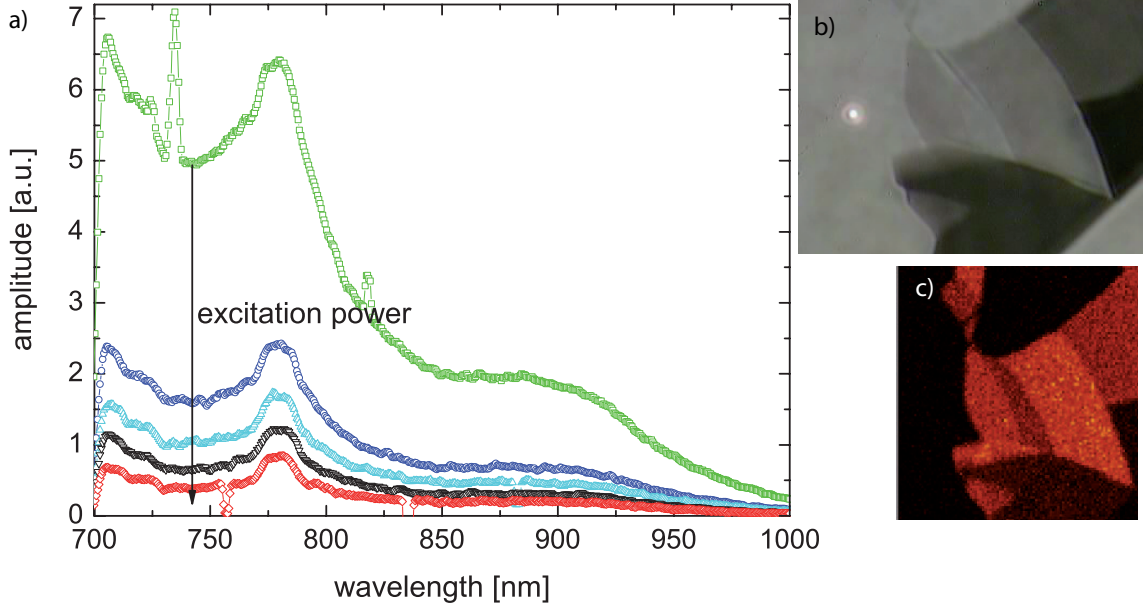


Fig. 8.4 In a) the respective NL-PL spectra of the multilayer graphene flakes as a function of excitation power is depicted. The sample was excited at 690 nm at a pulse duration of 150 fs. The small residual peaks at the laser center wavelength are caused by residual laser light. A snapshot b) through the microscope objective gives an impression of the visible contrast of thin graphene flakes on the glass substrate. The corresponding NL-PL map of graphene layers of varying thickness is shown in c). The thick layer visible in b) lower right side, appears dark in the PL image due to the Fabry-Perot like reflections at each interface [75] (see text).

In a first attempt literature described the effect of the NL-PL from single- and multilayer graphene by thermal induced emission based on the description of black body radiation [73].

$$I(\nu, T) = \frac{2h\nu^3}{c^2} \frac{1}{e^{\frac{h\nu}{kT}} - 1} \quad (8.3)$$

Where $I(\nu, T)$ is the energy per unit time radiated per unit area of the emitting surface per unit frequency by a black body temperature T and h is the Planck constant. c is the speed of light, k is the Boltzmann constant and ν the absolute frequency of the electromagnetic radiation emitted by the black body at an absolute temperature T . Here the spectral dependence on the excitation power is immediately obvious, since the excitation power is directly proportional to the temperature T of the emitter assuming no saturation effects. This relation is due to the Wien's displacement law, given by $\lambda_{max} = \frac{b}{T}$. Here b is the Wien's displacement constant. A consequence is that the wavelength of the emission is a function only of the temperature T . The theoretical spectra obtained by using Eqn. 8.3 in combination with the Wien's displacement law is plotted in Fig. 8.5.

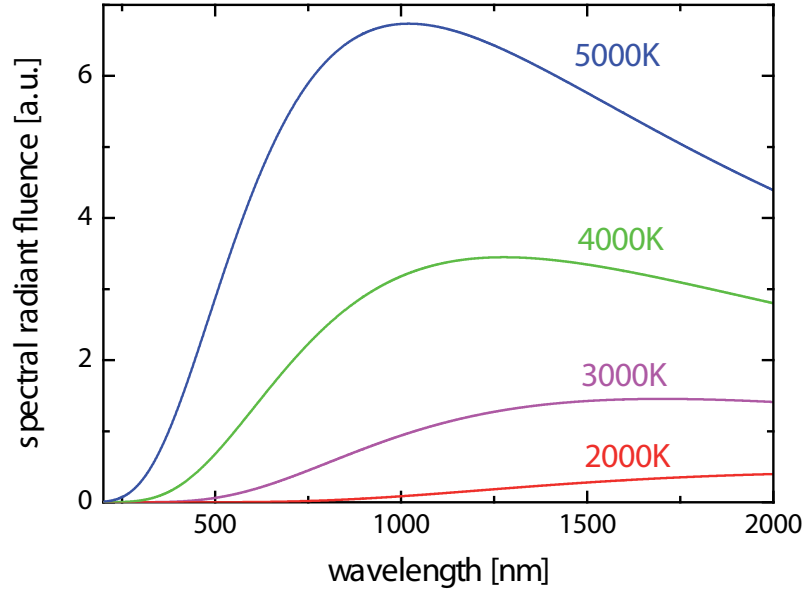


Fig. 8.5 Theoretical spectra based on the Eqn. 8.3. Variations of the excitation power lead to a shift of the spectral maximum, due to the resulting temperatures of the emitter. These strong dependence of the spectrum on the excitation power is not observed experimentally in Fig. 8.4.

Since the spectral characteristic of the NL-PL show no significant changes on variations of the excitation power it can be excluded that this effect is fully described by Planck's law (Eqn. 8.3) only. Variations of the excitation energy ranging from 1,34 eV to 1,64 eV shifts the obtained spectra but do not influence the spectral characteristic (see Fig. 8.6).

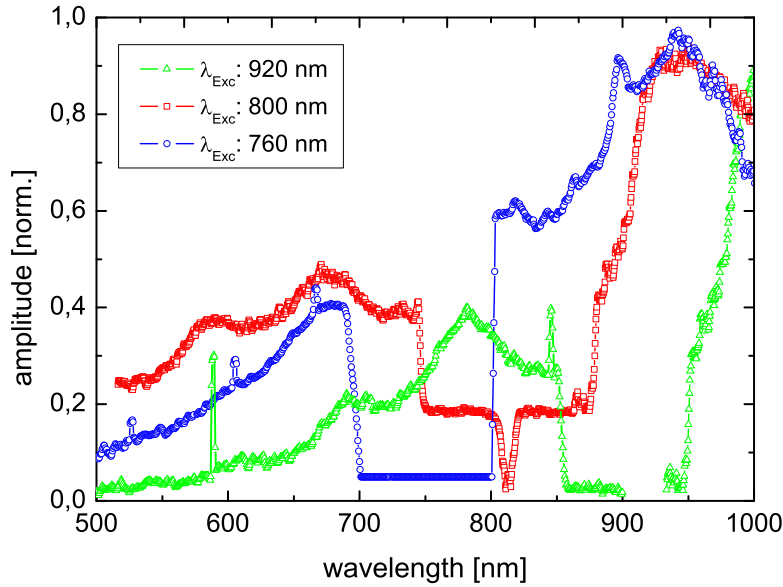


Fig. 8.6 By tuning the excitation wavelength the obtained NL-PL emission of graphene follows the excitation frequency. The shown data is corrected for differences in detection sensitivity of different wavelength.

These findings and the influence of the excitation energy on the obtained NL-PL spectra (Fig. 8.6) triggered the need of other explanations.

Another approach to explain the spectral broadening visible in Fig. 8.6 around the excitation laser energy is explained by inter- and intraband scattering of charge carrier (CC) and carrier-phonon (CP) [74, 75, 219].

The verification of theoretical explanation triggers the need of deeper insight into inter- and intraband excitation and relaxation processes. The used experimental system is limited to a time resolution of ≈ 150 fs due to the provided pulse duration. This is not sufficient to investigate these ultrafast dynamics occurring in graphene. To further investigate the ultrafast single femtosecond timescales of the intraband dynamics in the described 2D model system polarization resolved pulse shaping experiments have been carried out in Chap. 9.

8.4 Conclusion

The NL-PL of graphene on glass is demonstrated after femtosecond laser excitation at fixed pulse durations of 150 fs. The spectral characteristic of the NL-PL is not influenced by the excitation power. This excludes thermal induced radiation (black-body) as the only origin of the broadband NL-PL. Since the NL-PL spectra shift with excitation energy broadening by intraband Coulomb scattering is considered to be the responsible effect. To gain insight into the ultrafast (single fs) time scales an increase in time resolution is necessary. This is realized throughout Chap. 9 by ultrafast polarization resolved pulse shaping experiments.

9 Controlling charge carrier relaxation and photoluminescence in graphene using chirped laser pulses

9.1 Motivation

In this chapter the NL-PL from single and few layer graphene based on the findings presented in Chap. 8 is further investigated. Since this effect is explained by two competing models [73–75] the strong photoluminescence of graphene is in the focus of current research. To fully understand the radiative recombination of the created electrons and holes it is necessary to get insight into the timespan after the excitation and before the recombination of the charge carriers. This intraband scattering processes which cause a thermalization of the electron and hole population within the bands and the respective time regime (heterodynamic regime) is visualized by polarization resolved measurements and the simultaneous control of the excitation electric field on a femtosecond time scale. The findings and models presented in this section are based on the publication: **"Controlling charge carrier relaxation and photoluminescence in graphene using chirped laser pulses"**². In the course of this section it is shown that the control of the optical excitation of graphene leads to a control over the coupled coherence and the respective population dynamics of charge carriers. Therefore the NL-PL created by chirped broadband femtosecond laser pulses is detected either energy or polarization resolved. These experimental results provide insight into the microscopic polarization and its relaxation. Positively chirped excitation pulses for which the lower energy of the pulse interacts first with the sample maximizes the NL-PL intensity. The theoretical models applied within this chapter are developed by E. Malic and his co-workers [28, 29, 76, 77, 106] which are in overall agreement with the experimental results presented.

9.2 Materials and methods

9.2.1 Sample preparation

The samples are prepared as follows. Single layer (SLG), bilayer (BLG) and few layer graphene (FLG) are placed by micromechanical cleavage [235] on Si wafers covered with 300 nm SiO₂. The number of layers is identified by a combination of optical microscopy [236] and Raman spectroscopy [61, 62]. Glass substrates are coated with a layer of gold (25 nm) deposited by thermal evaporation. Subsequently a layer (25nm) of Al₂O₃ is placed onto the gold by atomic layer deposition (ALD)(see Fig. 9.1).

²manuscript under preparation

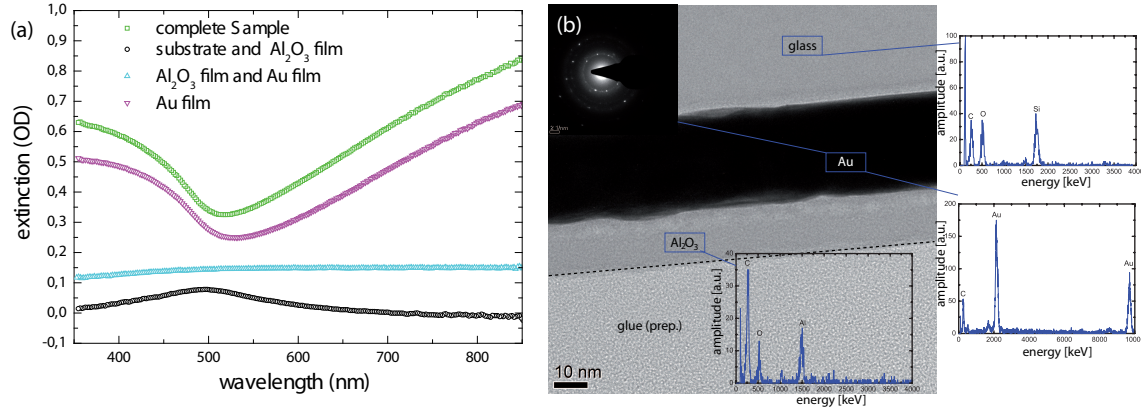


Fig. 9.1 In (a) the contribution of extinction of each of the sections of the used sample material is shown. Figure (b) shows a Transmission electron microscopy (TEM) image to control for the correct thickness and flatness of the used Au and Al₂O₃ substrate. The energy dispersive X-ray (EDX) spectra clearly showed the high purity and allowed for identification of the respective film.

This additional dielectric spacer prevents the NL-PL from being completely quenched by the metal film, while allowing for efficient SPP launch (Fig. 9.2c)). Graphene flakes are then transferred onto the glass-gold-Al₂O₃ stack by a polymer-based wet transfer process [16, 24]. PMMA (molecular weight 950 K) is spin coated onto the sample, which is then immersed in de-ionized water, resulting in the detachment of the polymer film because of water intercalation at the PMMA-SiO₂ interface. Graphene flakes attach to the polymer and are therefore removed from the Si/SiO₂. The polymer and graphene film is then placed onto the glass-gold-Al₂O₃ substrate and, after complete drying of the water, PMMA is removed by acetone. Control samples are also prepared by depositing graphene on uncoated glass substrates. Success of the transfer is confirmed both optically and by Raman spectroscopy. Analysis of position, full width at half maximum (FWHM), intensities and areas ratios of the G and 2D peaks allows estimation of doping [62, 63, 230, 237]. The initial SLG on Si/SiO₂ is slightly p-doped $\sim 3 \times 10^{12} \text{ cm}^{-2}$. After transfer the samples appear $\sim 5 \times 10^{12} \text{ cm}^{-2}$ n-doped.

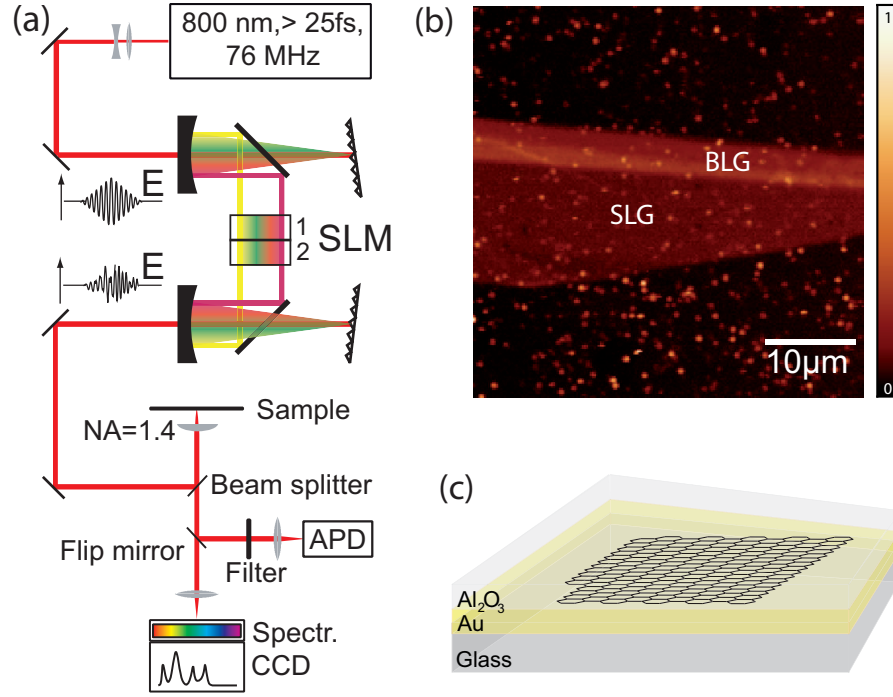


Fig. 9.2 (a) Schematic of the setup based on an inverted confocal microscope. The broadband laser pulses are spectrally dispersed and their spectral phase profile is controlled by a spatial light modulator (SLM). (b) NL-PL image of SLG and BLG $\text{Al}_2\text{O}_3/\text{Au}$ after femtosecond laser excitation at a center wavelength of 800 nm, recorded at the red side of the excitation pulse between 900 and 1000 nm. The bright spots result from imperfections in the $\text{Al}_2\text{O}_3/\text{Au}$ substrate. (c) Schematic of the sample layout.

The samples are measured with a confocal laser scanning optical microscope combined with a pulse shaper based³ on a spatial light modulator [92] to control the spectral phase profile of a linearly polarized broadband laser pulse (Fig. 9.2(a)). The excitation pulse provided by a Ti:Sa oscillator has a spectral FWHM ~ 60 nm and a minimum temporal duration of $t_p \approx 25$ fs. The excitation pulse can be described by the vector potential:

$$\mathbf{A}(t) = \mathbf{A}_C \exp\left(-t^2/2\sigma_C^2\right) \cos[\omega + \tilde{C}t]t \quad (9.1)$$

with the normalized chirp C , the duration $\sigma_C = \sigma\sqrt{1+C^2}$ and amplitude $\mathbf{A}_C = \mathbf{A}_0/\sqrt[4]{1+C^2}$ of the chirped pulse, the chirp $\tilde{C} = \frac{1}{2\sigma^2} \cdot \frac{C}{1+C^2}$, the Gaussian duration $\sigma = t_p/\sqrt{2\ln(2\sqrt{2})}$ and amplitude \mathbf{A}_0 of the unchirped pulse, and the central photon energy $\hbar\omega$. Therewith, the pulse spectrum and fluence is chirp independent (further details in Sec. 2.2.5).

To compensate for phase distortions created by optical elements in the beam path an iterative correction based on multi-photon intrapulse interference phase scans (MIIPS) is applied [130] using $\text{Fe}_2(\text{IO}_3)_3$ nanocrystals as reference material [134]. A brief experimental overview can be found in Sec. 3.2.3 of chapter Chap. 3

Optical dipole transitions in graphene are connected to carrier excitations with momentum mainly perpendicular to the electric field polarization (Fig. 9.3(b)) [76].

³For further technical details about the used SLM see Sec. 3.2.2

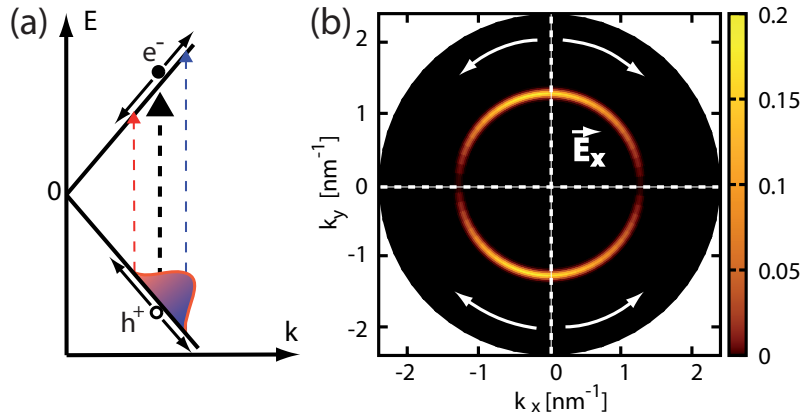


Fig. 9.3 (a) Linear band dispersion around the Dirac point. The dashed arrows indicate optical pumping for (black) the center wavelength of the pulse, (red) longer and (blue) shorter wavelengths. The solid arrows represent the relaxation via c-c scattering. (b) Theoretical snapshot of the carrier occupation after x-polarized excitation projected on the k_x - k_y -plane, neglecting c-c scattering. The white arrows indicate the relaxation via optical and acoustic phonons.

Absorbed photons initially create optically excited (“hot”) carriers. Their non-equilibrium dynamics has been studied by ultrafast pump-probe spectroscopy [26,27,54,55,65,218,238]. The non-equilibrium (non-thermal) distribution of electrons in conduction band and holes in valence band created by an ultrafast pulse relaxes, eventually reaching thermal equilibrium with the lattice, due to various processes [26–29,70–72,76], including carrier-carrier (c-c) and carrier-phonon (c-ph) scattering, as well as radiative electron-hole (e-h) recombination (non-linear photoluminescence, NL-PL [73,224,239]). In the sub-ps time-frame two main processes occur: first, the initial peak produced by the pump laser broadens, due to c-c collisions, converging towards a hot Fermi-Dirac (FD) shape on an ultrashort time scale [26,27,68,69,240–243], see Fig. 9.3(a). The Coulomb interaction prefers scattering along the Dirac cone, which preserves the initial anisotropic carrier distribution. The scattering across the Dirac cone is partially suppressed and even completely vanishes in the case of back-scattering [77]. Subsequently, optical phonon emission [244,245] drives a cooling in which the FD distribution shifts towards the Dirac point. The phonon interaction with the electrons causes the carriers to move also along the circumference of the cone by gaining or losing momentum \mathbf{k} (Fig. 9.3(b)). These processes lead to orientational relaxation and an isotropic carrier distribution [77].

On thin metal films dipole emission is known to launch propagating surface plasmon polaritons (SPPs) mainly in the direction of the dipole orientation such that Fourier imaging of the SPP-coupled NL-PL can be used to visualize its degree of polarization [118–120,122,246]. The experimental details of imaging the back focal plane of the objective [120–122] to conserve the spatial distribution of the emission is found in Sec. 3.1.1 of Chap. 3. In the following sections it is shown that the carrier relaxation dynamics in graphene on glass and on thin gold films can be controlled by chirping the excitation laser pulse on femtosecond time scales by monitoring the NL-PL intensity and polarization contrast.

9.3 Results and discussion

9.3.1 NL-PL intensity dependence on normalized chirp

The chirp dependence of the NL-PL intensity of FLG on $\text{Al}_2\text{O}_3/\text{Au}$ detected on the blue and on the red side of the excitation energy is shown in Fig. 9.4. NL-PL traces were derived by integrating the emission spectra shown in Fig. 9.4 from 600 - 690 nm and 880- 1000 nm, respectively. Both curves peak at positive chirp between $C = 1 - 2$ as observed in the intensity profiles recorded using an avalanche photo diode (APD) after spectral filtering between 900 and 1000 nm shown in Fig. 9.5, although at somewhat smaller value $C = 1$.

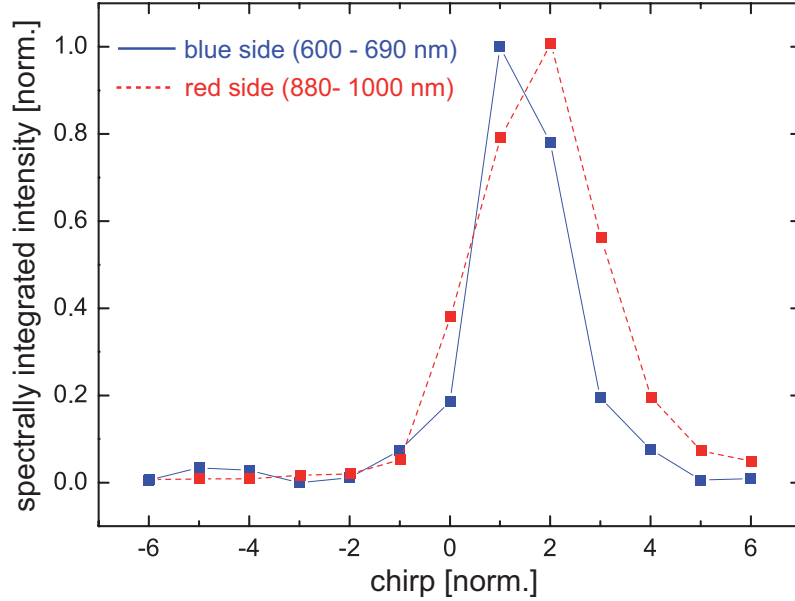


Fig. 9.4 Chirp dependence of the spectrally integrated NL-PL intensity detected on the blue side (600 – 690 nm) and on the red side (880 – 1000 nm) of the laser excitation energy. Chirp 0 corresponds to a pulse duration of 25 fs.

Fig. 9.5(a,b) show the dependence of the NL-PL intensity of few layer graphene (FLG) detected between 900 and 1000 nm on the chirp C of the excitation laser pulse. While the intensity increases for shorter pulses, as expected for a multi-photon process, the highest intensity is observed for a positively chirped pulse with $C = 1.0 \pm 0.2$ for graphene on $\text{Al}_2\text{O}_3/\text{Au}$. For graphene on glass, Fig. 9.5(b) shows a slightly smaller chirp for the maximum NL-PL intensity, indicating an influence of plasmonic field enhancement. As reference, the second harmonic signal (SHG) of $\text{Fe}_2(\text{IO}_3)_3$ nanocrystals between 380 – 420 nm is recorded [134]. The SHG-signal is maximized for the shortest pulse ($C = 0$, $t_p \approx 25$ fs) as expected for an instantaneous two-photon process [89]. The chirp dependence of the NL-PL intensity can also be seen in the corresponding spectra detected at the same sample position on both sides of the excitation energy (Fig. 9.5(c,d)). The highest NL-PL intensity is obtained for chirp C between 1 and 2.

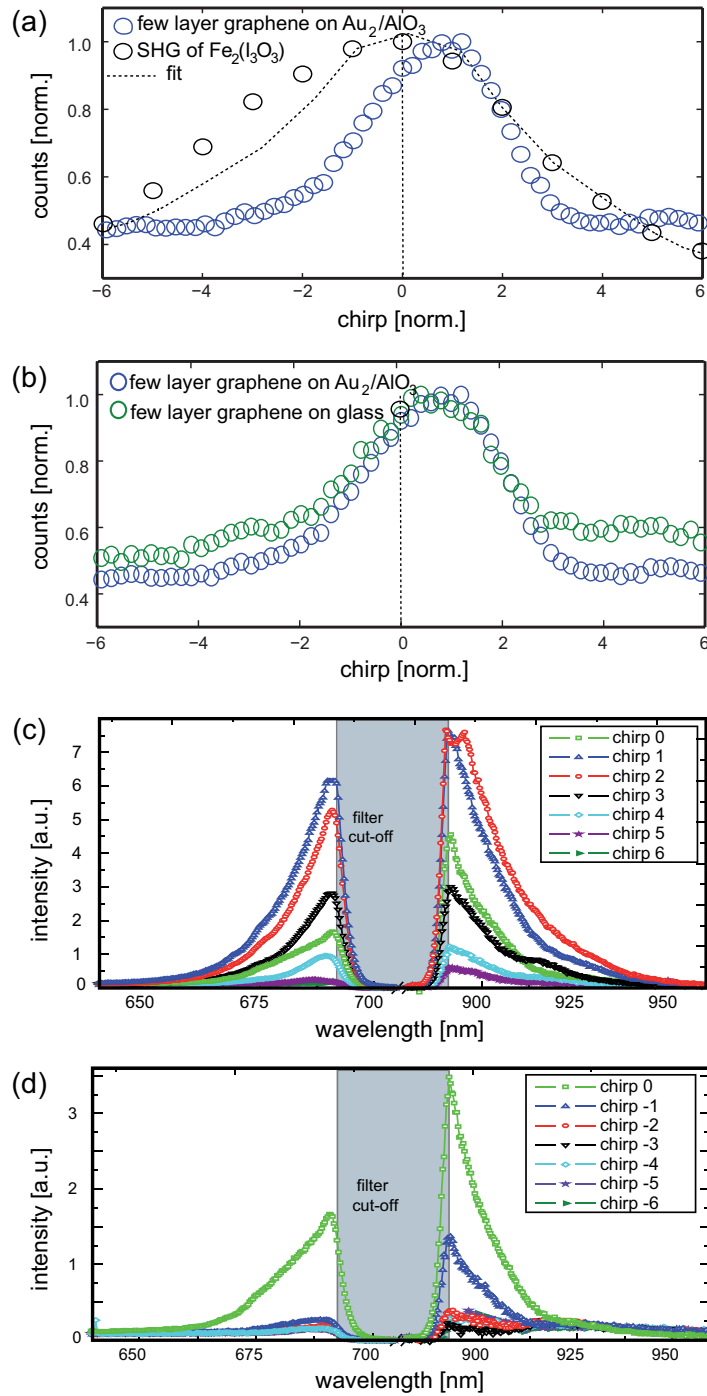


Fig. 9.5 (a,b) (blue circles) FLG NL-PL intensity detected between 900 and 1000 nm for varying normalized chirp. The highest intensity is detected for positive chirp $C = 1.0 \pm 0.3$ for flakes on $\text{Al}_2\text{O}_3/\text{Au}$, while the maximum NL-PL intensity for flakes on glass is observed for $C = 0.9 \pm 0.3$. (black circles) SHG-signal of $\text{Fe}_2(\text{IO}_3)_3$ detected between 380 – 420 nm as reference. (c,d) Chirp dependent NL-PL spectra of graphene recorded at the same sample position for varying positive and negative chirp, respectively. The spectra are normalized to the maximum intensity recorded in the respective series and are corrected for a signal background from the substrate detected without flakes while the intensity traces in (a) and (b) show raw data.

9.3.2 NL-PL polarization dependence on normalized chirp

Imaging the objective BFP for dipole emitters on a thin metal film can be used to retrieve information on the polarization of the dipoles, as discussed above. For uniform dipole orientation parallel to the film two bright arcs would be detected, while an isotropic distribution would lead to a continuous ring [120, 122, 246].

The detected emission pattern (see Fig. 9.6) obtained by back focal plane imaging (experimental details can be found Fig. 3.5) can be understood as the physical connection between photon ($k_{||,x}, k_{||,y}$) and carrier occupation (k_x, k_y).

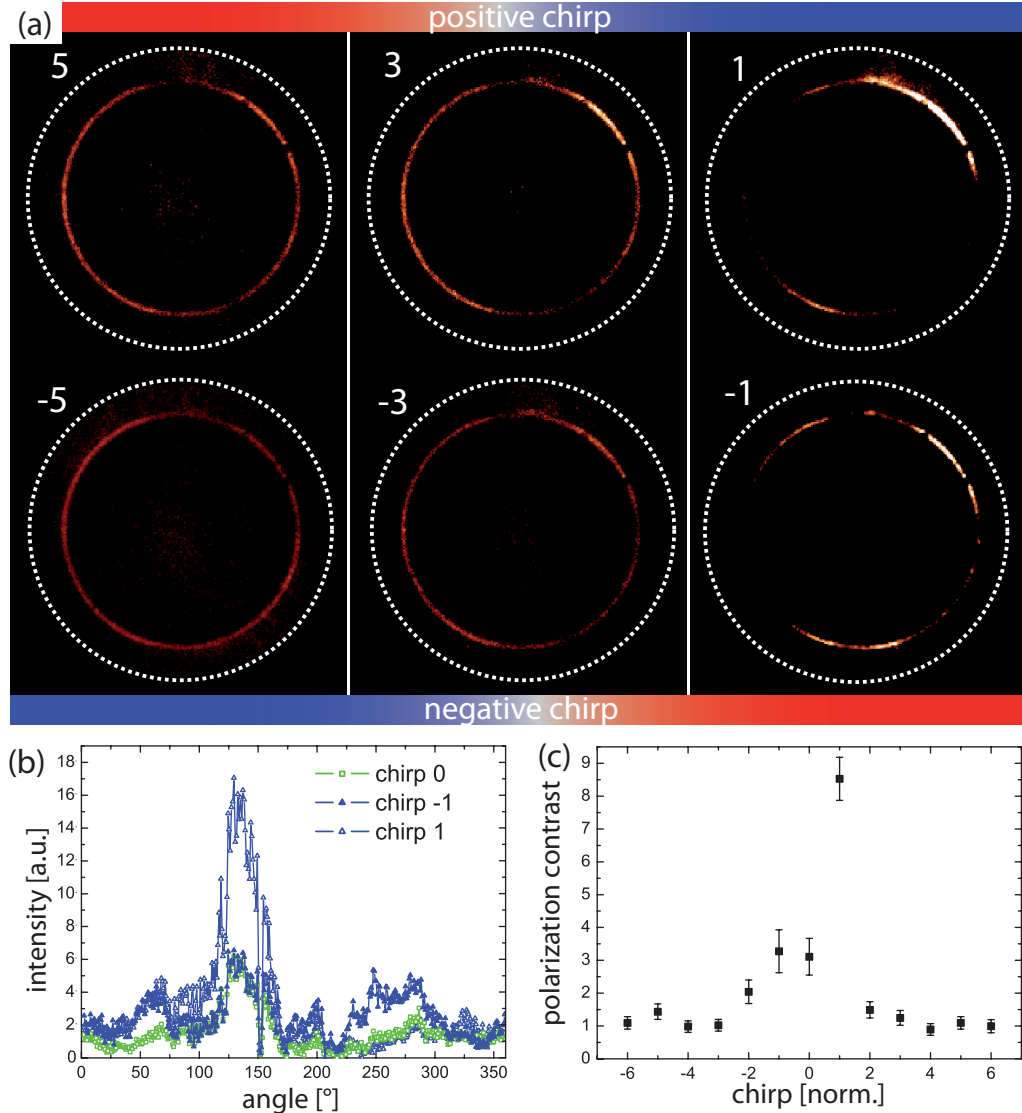


Fig. 9.6 (a) BFP images of NL-PL from SLG on $\text{Al}_2\text{O}_3/\text{Au}$ for differently chirped pulses detected on the red side of the excitation pulse between 900 and 1000 nm. The white dashed ring corresponds to $\text{NA} = 1.4$. All images are scaled equally and recorded at the same sample position. (b) Angular-resolved NL-PL profiles for $C = 1, 0, -1$. (c) Polarization contrast (maximum/minimum within the ring-like pattern) as a function of chirp. For larger chirp corresponding to longer pulse length the detected pattern becomes radially symmetric indicating the angular relaxation of carriers [72].

The emission energy, that is proportional to the carrier momentum k in case of the linear dispersion in graphene, determines $|k_{SPP}| = |k_{||,resonance}|$, the radius of highest intensity in the detected emission pattern. At about 900 nm the ratio between the radii $|k_{||,resonance}|$ and k is roughly v/v_F where v is the speed of light in glass and v_F the Fermi-velocity of carriers in graphene. The angular distribution of the emission pattern, on the other hand, reflects the angular dependence of the carrier occupation. The carrier occupation can be approximated by a \cos^2 -relation results from a dipolar transition. For a dipolar emitter the intensity can be calculated according to eqn. 3.1 where the angle dependence also follows a \cos^2 -relation although rotated by 90° due to the optical matrix element. Loss of orientational memory in the carrier occupation after linearly polarized pulsed excitation thus results in a ring-like BFP pattern. Fig. 9.6(a) shows BFP-images of the NL-PL from graphene for varying chirps, decreasing from $C = 5$ to -5 (upper row to lower row). For long pulses, as created by large absolute chirps, the NL-PL forms a continuous ring corresponding to isotropic emission polarization. This shows that NL-PL emission happens during the formation of a quasi uniform angular distribution of the carrier population as a result of c-ph scattering. For shorter pulses, in particular for $C = 1$, on the other hand, strongly anisotropic emission is observed, indicating that ph-induced scattering across the Dirac cone is not finished during the short pulse. As a result, the optically generated anisotropy in carrier occupation and polarization remains partially conserved. Our modeling confirms the increase of the polarization contrast for positive chirp, as shown in Fig. 9.7(b). This directly reflects the scattering-induced chirp dependence of the NL-PL intensity and follows the anisotropy of the electron-light coupling, as also indicated in Fig. 9.7(a) and the inset of Fig. 9.2(a). In the experiment, the observed difference between upper and lower arcs could be assigned to spatial heterogeneities in the gold film, that lead to different SPP propagation.

Since in SLG the polarization reflects the angular distribution of the carrier population, BFP images are thus a means to visualize the angular dependence of the microscopic polarization and the carrier population in SLG, see Fig. 9.7(b).

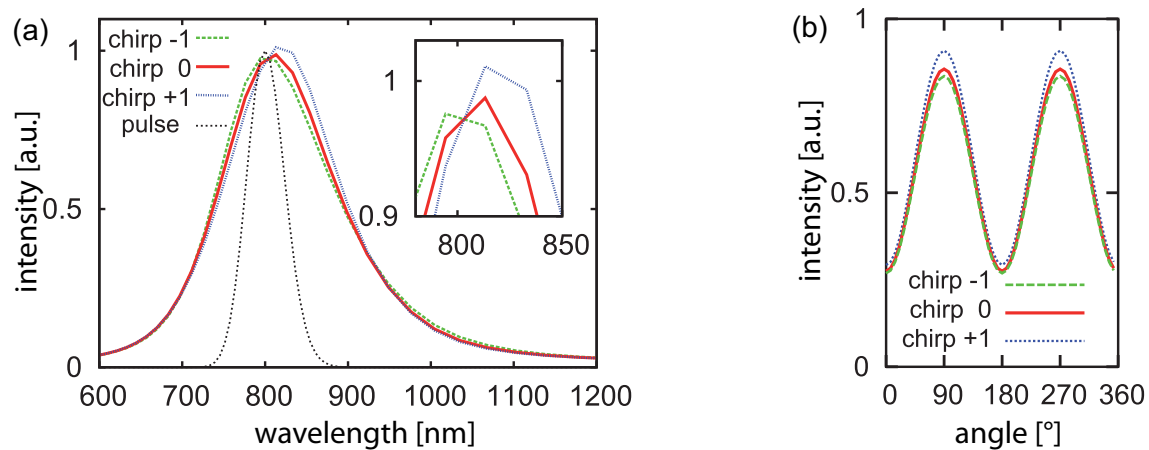


Fig. 9.7 (a) Theoretically evaluated NL-PL from SLG for different chirps. A slight red-shift of the maximum is observed and an increase in intensity for positive chirps. (b) Theoretically modeled angular resolved NL-PL profiles, which show highest contrast and intensity for positive chirp.

The theoretically evaluated NL-PL spectrum from SLG graphene according to Eqn. 9.7 agrees very well with the measured spectrum, indicating that the scattering processes that

broaden the NL-PL are well captured by the modeling (Fig. 9.7⁴). Although the pulse fluence and pulse spectrum is independent of the chirp, the calculations reveal a decrease in intensity for negative chirps. This can be understood as follows: The phonon-induced broadening of the excited carrier distribution occurs more efficiently towards the Dirac point than towards higher energies. Consequently, the damping of the microscopic $p_{\mathbf{k}}$ due to diagonal dephasing is stronger below the excitation energy, Eqn. 2.51. As a result, the absorption of the lower energy-side of the excitation pulses with negative chirp is suppressed by the ultrafast dephasing, giving rise to a lower intensity of the NL-PL.

In contrast, for positive chirps, the higher energy-side of the excitation pulse comes with a delay. At higher energies, the phonon-induced scattering is weaker, resulting in a smaller dephasing and higher NL-PL intensities. Thus, the theoretically predicted NL-PL chirp dependence shows qualitatively the same trend as the experimentally measured one. The quantitatively more pronounced changes in intensity in Fig. 9.5 may be due to coupling to the substrate, in particular NL coupling between the PL of graphene and the SPPs. Furthermore, the calculations show a slight red-shift of the PL maximum for positive chirp (see inset, Fig. 9.7), indicating that the NL-PL excited by the initial tail of the pulse is more efficient.

9.3.3 Modeling of the NL-PL

To understand the chirp dependence qualitatively from a microscopic point of view, the dynamics of the microscopic polarization $p_{\mathbf{k}}(t)$ in intrinsic SLG within the Bloch equations for $C = -1, 0, 1$ [76] is calculated, by our cooperation partners E. Malic and T. Winzer⁵: The photoluminescence $I_{PL}(\mathbf{q}, t)$ of the photon mode \mathbf{q} is given by the photon flux [247]:

$$I_{PL}(\mathbf{q}, t) \propto \frac{\partial}{\partial t} \langle c_{\mathbf{q}}^{\dagger} c_{\mathbf{q}} \rangle(t), \quad (9.2)$$

where $c_{\mathbf{q}}^{\dagger}$ and $c_{\mathbf{q}}$ are photon creation and annihilation operators. Exploiting the electron-photon Hamilton operator H_{c-pt}

$$H_{c-pt} = \sum_{\mathbf{k}, \mathbf{q}} \left[\mathcal{M}_{\mathbf{k}, \mathbf{q}}^{vc} a_{\mathbf{k}}^{v\dagger} a_{\mathbf{k}}^c c_{\mathbf{q}}^{\dagger} + \mathcal{M}_{\mathbf{k}, \mathbf{q}}^{cv} a_{\mathbf{k}}^{c\dagger} a_{\mathbf{k}}^v c_{\mathbf{q}} \right], \quad (9.3)$$

The equation of motion for the photon occupation is derived by:

$$i\hbar \frac{d}{dt} \langle c_{\mathbf{q}}^{\dagger} c_{\mathbf{q}} \rangle(t) \Big|_{H_{c-pt}} = \sum_{\mathbf{k}} \mathcal{M}_{\mathbf{k}, \mathbf{q}}^{vc} \left[\langle a_{\mathbf{k}}^{v\dagger} a_{\mathbf{k}}^c c_{\mathbf{q}}^{\dagger} \rangle(t) - \langle a_{\mathbf{k}}^{c\dagger} a_{\mathbf{k}}^v c_{\mathbf{q}} \rangle(t) \right] \quad (9.4)$$

with the electron-photon matrix element $\mathcal{M}_{\mathbf{k}, \mathbf{q}}^{\lambda\lambda'}$ and the photon-assisted quantities $\langle a_{\mathbf{k}}^{\lambda\dagger} a_{\mathbf{k}}^{\lambda'} c_{\mathbf{q}}^{(\dagger)} \rangle(t)$. To close the system of equations a further equation of motion is needed for these quantities. Neglecting the dynamics of coherent photons, i.e. $\langle \dot{c}_{\mathbf{q}}^{(\dagger)} \rangle = 0$, and the stimulated emission is described by:

$$i\hbar \frac{d}{dt} \langle a_{\mathbf{k}}^{v\dagger} a_{\mathbf{k}}^c c_{\mathbf{q}}^{\dagger} \rangle(t) = (\varepsilon_{\mathbf{k}}^c - \varepsilon_{\mathbf{k}}^v - \hbar\omega_{\mathbf{q}}) \langle a_{\mathbf{k}}^{v\dagger} a_{\mathbf{k}}^c c_{\mathbf{q}}^{\dagger} \rangle(t) - \mathcal{M}_{\mathbf{k}, \mathbf{q}}^{vc} \left(\rho_{\mathbf{k}}^c(t) [1 - \rho_{\mathbf{k}}^v(t)] + |p_{\mathbf{k}}(t)|^2 \right) \quad (9.5)$$

⁴calculated by T. Winzer from the group of Prof. E. Malic

⁵Detailed information about the theoretical modeling of the ultrafast relaxation dynamics after femto-second laser excitation in graphene is found in the Dissertation of Torben Winzer (2013) [112]

Treating Eq. (9.5) within the Markov approximation [76], Eq.(9.5) can be analytically solved. Furthermore, assuming that the surface plasmons measured in the experiment only couple to the polarization, the equation of motion for the photon occupation reads:

$$\frac{d}{dt}\langle c_{\mathbf{q}}^\dagger c_{\mathbf{q}} \rangle(t) = \frac{\pi}{\hbar} \sum_{\mathbf{k}} |\mathcal{M}_{\mathbf{k},\mathbf{q}}^{vc}|^2 |p_{\mathbf{k}}(t)|^2 \delta(\varepsilon_{\mathbf{k}}^c - \varepsilon_{\mathbf{k}}^v - \hbar\omega_{\mathbf{q}}). \quad (9.6)$$

Accounting for the polarization $\mathbf{e}_{\mathbf{q}}$ of the photon mode \mathbf{q} , the electron-photon matrix element has the same symmetry as the semi-classical electron-field matrix element, i.e. $\mathcal{M}_{\mathbf{k},\mathbf{q}}^{vc} \propto \mathbf{e}_{\mathbf{q}} \cdot \mathbf{M}_{\mathbf{k}}^{vc}$. Finally the integration over the detection time, Eq. (9.6) give access to the photoluminescence:

$$I_{PL}(\omega, \phi) \propto \int dt \sum_{\mathbf{k}} |p_{\mathbf{k}}(t)|^2 \left| M_{\mathbf{k}}^\phi \right|^2 \delta(\omega - v_F k), \quad (9.7)$$

where $M_{\mathbf{k}}^\phi$ is the projection of the matrix element along the ϕ direction in the Brillouin zone. Since the polarization may also be influenced by the number of excited charge carriers one can add the the following interaction term to eqn. 9.7 based on the graphene Bloch equations presented in Sec. 2.2.7 of Chap. 2:

$$I_{PL}(\omega, \phi) \propto \int dt \sum_{\mathbf{k}} |p_{\mathbf{k}}(t)|^2 \left| M_{\mathbf{k}}^\phi \right|^2 [\rho_{\mathbf{k}}^c(t) \rho_{\mathbf{k}}^v(t) + p_{\mathbf{k}}(t) p_{\mathbf{k}}^*(t)] \delta(\omega - v_F k). \quad (9.8)$$

With the carrier occupation $\rho_k(t)$ and $M_{\mathbf{k}}^\phi$ again representing the optical matrix element in ϕ -direction.

9.3.4 High and low power limit of the excitation

From the experimental results presented in the previous chapter 8 and the experimental results within this chapter it became clear that excitation energy and the respective energy density significantly influences the creation of the NL-PL of graphene. In the section the presented theoretical model is applied on an scenario in which the excitation energy is fixed at 1.55eV (800nm), while the power was changed from 12μJ(low power regime) to 5.7mJ(high power regime). In combination with the simplified equations of motion, which are identical to the well-known Bloch equations for the off-diagonal, $\hat{\phi}_\lambda$, and diagonal \hat{n}_λ , elements of the density matrix of a two level atom based on the findings in [106] and the equations in 2.2.7:

For not too strong optical excitation phase space filling, screening and band gap renormalization is neglected [107–109]. From the Coulomb interaction term V only the mutual attraction between electrons and holes is considered. These assumption lead to the following description of the expectation values introduced in 2.2.7.

$$\frac{\partial}{\partial t} p_k^* = i[\epsilon_e^s(k) + \epsilon_h^s(k)] p_k^* - i \sum_{q(\neq 0)} V(q) p_{k+q}^* - i \mu_k^* E(t)^* (1 - n_{e,k} - n_{h,k'}) \quad (9.9)$$

$$\frac{\partial}{\partial t} \hat{\phi}_\lambda = i \epsilon_\lambda \hat{\phi}_\lambda - i \mu^* E^*(t) (1 - 2\hat{n}_\lambda), \quad (9.10)$$

The full mathematical description of the SBEs can be found elsewhere [106]. The microscopic polarization becomes macroscopic because of the applied external field. Finally it is necessary to mention that the optical response of a semiconductor follows its macroscopic polarization P as a function of the electric field E that excites it. While the macroscopic

polarization is described by the microscopic polarization p_k for the low power coherent regime:

$$P = \mu \sum_k \langle a_k^\dagger b_{-k}^\dagger \rangle + c.c. \quad (9.11)$$

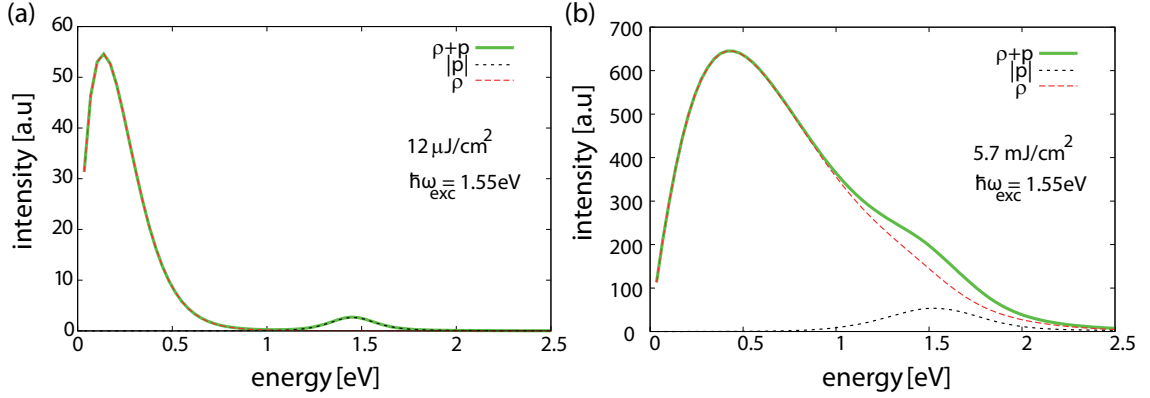


Fig. 9.8 The polarization p and the density of states ρ show a significant difference in (a) for the low power regime. Here the polarization is the major contribution to the signal, since the scattering rate is negligible in this regime (red dashed line shows no contribution around the excitation energy of 1.55 eV). In (b) the excitation power is increased by a factor of almost 500 (high power regime). The microscopic polarization p is decreased by the increased Coulomb scattering rate induced by the high amount of charge carriers ρ and the structure of the PL spectrum is triggered by scattering of charge carriers.

The resulting contribution based on the calculation the graphenes' Bloch equations of the polarization p and charge carrier density ρ for high and low pump fluences on the resulting PL intensity is shown in Fig. 9.8⁶. Therefore the excitation energy is again kept constant at 1.55 eV . By increasing the pump fluence by a factor of ≈ 500 the PL spectrum gets broadened due to scattering, while only a small contribution of polarization remains (9.8 b)). Obviously the PL characteristics depend strongly on the pump fluence. The emission of single layer graphene excited at high fluences can be described by the model of T. Heinz and co-workers [73] and is independent from the excitation energy while for low fluences the NL-PL can be properly described by the microscopic polarization [74, 218], which is sensitive towards excitation energy. The presented full model based on the graphene Bloch equations describing microscopic polarization p , carrier density ρ and phonon induced scattering [248] lead to a detailed description of inter- and intraband processes [68, 69]. The applied model is in overall agreement with the introduced experimental findings covering the full range of excitation time, power and energy.

However, the chirp dependence observed in experiment is stronger pronounced than theory predicts although only the contribution of polarization is taken into account to fully describe the NL-PL chirp dependence. This is also remarkable since all used chirped excitation pulses have the same spectrum and pump fluence.

Since the quantitative discrepancy is quite large, so that other or additional effects have to be taken into account. Quantum or plasmonic effects could play a crucial role. Also doping effects by the the substrate have to be considered, since the graphene is supported on

⁶graph by the group of Prof. E. Malic

Al₂O₃/Au/glass film. At last the excitation of graphene surface plasmons could eventually influence the measurement.

Following eqn. 9.8 a huge contribution on the excitation fluence should be visible which is not supported by the presented experimental findings.

9.4 Conclusion

In summary the charge carrier relaxation dynamics in graphene induced by ultrafast chirped laser pulses by recording the non-linear photoluminescence were studied. It is found in case of a positive chirp for which the red part of the laser spectrum interacts first with the graphene the NL-PL intensity is maximized while for negative chirp it is substantially suppressed. The intensity and the polarization contrast of the NL-PL is found to be increased substantially when the chirp is tuned to match the relaxation dynamics. Leakage radiation microscopy [118,119] detection together with back-focal plane (BFP) imaging [120–122] was utilized to investigate the carrier relaxation with momentum (k_x, k_y) resolution in the presented experiments. It is remarkable that for short excitation pulse length (≤ 50 fs) the polarization is maintained indicating that the emission process is essentially completed before efficient orientational relaxation occurs. These observations are in overall agreement with theoretical modeling that predicts the damping of the microscopic polarization due to stronger diagonal dephasing below the excitation energy leading to reduced absorption of the lower energy-side of the excitation pulses. The observed chirp dependence could be used to improve and control the efficiency of photonic graphene devices, such as saturable absorbers, and contribute to the overall understanding of the charge carrier relaxation in graphene.

10 Summary and outlook

In the course of this work several studies on the charge carrier dynamics within organic polymers and graphene are presented. This fundamental key knowledge is necessary to design future electronic and optoelectronic devices, like solar cells, transistors, LEDs and many others. In the first part of this thesis several methods to improve the efficiency of organic or hybrid/organic photovoltaic devices are presented. Each major drawback of organic polymers currently used for the fabrication of solar cell devices is addressed separately and an approach to overcome this material disadvantage is presented. These approaches consist of the improvement of the blocking layer to allow for efficient charge carrier separation and transport by controlling the morphology either by the fabrication method Chap. 7 or by the calcination time Chap. 6 to expand the grain size of the TiO_2 single crystals. The control of morphology addresses the drawback of the high exciton binding energy within the organic polymer. The second major drawback of this materials is the short exciton diffusion length ranging from 10 to ≈ 100 nm. This disadvantage vanishes by controlling the morphology of the molecules within the polymer film to allow for unpercolated pathways for the charge carriers. This is realized by self-induced ordering within a P3HT thin film by nano-patterning of the utilized substrate described in Chap. 4. Another approach to eliminate this disadvantage is the sequential stacking of electron donor and acceptor within the range of the excitation diffusion length. This is realized in Chap. 5, where a photoconductive thienothiophene-based covalent organic framework (TT-COF) is interpenetrated by PCBM. The pore size of the TT-COF serving as electron donor is ≈ 3 nm allowing for efficient separation and transport of generated charges.

Another important topic in the development of optoelectronic and electronic devices is the choice of the contact material which needs to be transparent in many applications. A perfect candidate to realize transparent contact electrodes is graphene due to its outstanding material properties described in Chap. 8 and in Chap. 9.

The second part of this thesis is dedicated to the ultrafast charge carrier dynamics in intrinsic graphene investigated by the NL-PL excited by femtosecond laser pulses in Chap. 8 and in Chap. 9. Since the charge carrier dynamics in graphene occur on femtosecond time scales ultrafast polarization resolved pulse shaping experiments have been carried out to extract the contribution and time scales of carrier-carrier and carrier-phonon scattering within the inter- and intraband excitation and relaxation processes.

For future device designs the presented approaches within this work should be combined to allow for maximum efficiency.

Bibliography

- [1] E. Becquerel, “Untersuchung über die Hervorrufung der Phosphoreszenz und über verschiedene Eigenschaften des elektrischen Funkens,” *Annalen der Physik* **124**, 540–549 (1839).
- [2] A. Einstein, “Über einen die Erzeugung und Verwandlung des Lichtes betreffenden heuristischen Gesichtspunkt,” *Annalen der Physik* **322**, 132–148 (1905).
- [3] R. S. Ohl, “Light Sensitive Electric Device,” USPTO (1941).
- [4] “1962-ALPHA EPSILON 1,” US Space Objects Registry **Retrieved 2012-07-15** (2012).
- [5] G. Zhao, Y. He, and Y. Li, “6.5 % Efficiency of Polymer Solar Cells Based on poly(3-hexylthiophene) and Indene-C 60 Bisadduct by Device Optimization,” *Adv. Mat.* **22**, 4355–4358 (2010).
- [6] H. A. Atwater and A. Polman, “Plasmonics for improved photovoltaic devices,” *Nat. Mat.* **9**, 205–213 (2010).
- [7] X. Wang, L. Zhi, and K. Müllen, “Transparent, Conductive Graphene Electrodes for Dye-Sensitized Solar Cells,” *Nano Lett.* **8**, 323–327 (2008).
- [8] L. Kavan, J. Yum, and M. Grätzel, “Optically Transparent Cathode for Dye-Sensitized Solar Cells Based on Graphene Nanoplatelets,” *ACS Nano* **5**, 165–172 (2011).
- [9] G. Eda, Y.-Y. Lin, S. Miller, C.-W. Chen, W.-F. Su, and M. Chhowalla, “Transparent and conducting electrodes for organic electronics from reduced graphene oxide,” *Appl. Phys. Lett.* **92**, 233 305 (2008).
- [10] N. Yang, J. Zhai, D. Wang, Y. Chen, and L. Jiang, “Two-Dimensional Graphene Bridges Enhanced Photoinduced Charge Transport in Dye-Sensitized Solar Cells,” *ACS Nano* **4**, 887–894 (2010).
- [11] P. Wallace, “The Band Theory of Graphite,” *Physical Review* **71**, 622–634 (1947).
- [12] J. W. McClure, “Diamagnetism of Graphite,” *Phys. Rev.* **104**, 666–671 (1956).
- [13] J. Slonczewski and P. Weiss, “Band Structure of Graphite,” *Phys. Rev.* **109**, 272 – 279 (1958).
- [14] K. S. Novoselov, D. Jiang, F. Schedin, T. J. Booth, V. V. Khotkevich, S. V. Morozov, and A. K. Geim, “Two-dimensional atomic crystals,” *PNAS* **102**, 10 451–10 453 (2005).
- [15] C. Berger, Z. Song, T. Li, X. Li, A. Y. Ogbazghi, R. Feng, Z. Dai, A. N. Marchenkov, E. H. Conrad, P. N. First, and W. A. de Heer, “Ultrathin Epitaxial Graphite: 2D Electron Gas Properties and a Route toward Graphene-based Nanoelectronics,” *J. Phys. Chem. B* **108**, 19 912 (2004).

- [16] F. Bonaccorso, A. Lombardo, T. Hasan, Z. Sun, L. Colombo, and A. C. Ferrari, “Production and processing of graphene and 2d crystals,” *Mater. Today* **15**, 564–598 (2012).
- [17] K. S. Novoselov, A. K. Geim, S. V. Morozov, D. Jiang, Y. Zhang, S. V. Dubonos, I. V. Grigorieva, and A. A. Firsov, “Electric field effect in atomically thin carbon films,” *Science* **306**, 666–669 (2004).
- [18] K. Klitzing, G. Dorda, and M. Pepper, “New Method for High-Accuracy Determination of the Fine-Structure Constant Based on Quantized Hall Resistance,” *Phys. Rev. Lett.* **45**, 494–497 (1980).
- [19] Y. Zhang, Y.-W. Tan, H. L. Stormer, and P. Kim, “Experimental observation of the quantum Hall effect and Berry’s phase in graphene,” *Nature* **438**, 201–204 (2005).
- [20] K. Novoselov, E. McCann, S. Morozov, V. I. Falko, M. Katsnelson, U. Zeitler, D. Jiang, F. Schedin, and A. K. Geim, “Unconventional quantum Hall effect and Berry’s phase of 2π in bilayer graphene,” *Nature Physics* **2**, 177–180 (2006).
- [21] K. S. Novoselov, Z. Jiang, Y. Zhang, S. V. Morozov, H. L. Stormer, U. Zeitler, J. C. Maan, G. S. Boebinger, P. Kim, and A. K. Geim, “Room-Temperature Quantum Hall Effect in Graphene,” *Science* **315**, 1379 (2007).
- [22] A. Geim and K. Novoselov, “The rise of graphene,” *Nature Mater.* **6**, 183–191 (2007).
- [23] A. H. Castro Neto, F. Guinea, N. M. R. Peres, K. S. Novoselov, and A. K. Geim, “The electronic properties of graphene,” *Reviews of Modern Physics* **81**, 109–162 (2009).
- [24] F. Bonaccorso, Z. Sun, T. Hasan, and A. C. Ferrari, “Graphene photonics and optoelectronics,” *Nature Photonics* **4**, 611–622 (2010).
- [25] F. Koppens, D. E. Chang, and F. J. García de Abajo, “Graphene Plasmonics: A Platform for Strong Light-Matter Interactions,” *Nano Lett.* **11**, 3370 (2011).
- [26] D. Brida, A. Tomadin, C. Manzoni, Y. Kim, A. Lombardo, S. Milana, R. R. Nair, K. Novoselov, A. C. Ferrari, G. Cerullo, and M. Polini, “Ultrafast collinear scattering and carrier multiplication in graphene,” *Nature Comm.* **4**, 1987 (2013).
- [27] A. Tomadin, D. Brida, G. Cerullo, A. C. Ferrari, and M. Polini, “Non-equilibrium dynamics of photo-excited electrons in graphene: collinear scattering, Auger processes, and the impact of screening,” *arXiv* **1305.5943** (2013).
- [28] T. Winzer and E. Malic, “Impact of Auger processes on carrier dynamics in graphene,” *Phys. Rev. B Rapid Comm.* **85**, 241 404 (2012).
- [29] T. Winzer, A. Knorr, and E. Malic, “Carrier Multiplication in Graphene,” *Nano Lett.* **10**, 4839 (2010).
- [30] J. Mertens, A. L. Eiden, D. Sigle, A. Lombardo, Z. Sun, R. Sundaram, A. Colli, C. Tserkezis, J. Aizpurua, S. Milana, A. Ferrari, and J. Baumberg, “Controlling Sub-nm Gaps in Plasmonic Dimers using Graphene,” *arXiv* **1305.5367** (2013).
- [31] T. Dürkop, S. A. S. A. Getty, E. Cobas, and M. S. Fuhrer, “Extraordinary Mobility in Semiconducting Carbon Nanotubes,” *Nano Lett.* **4**, 35–39 (2004).

-
- [32] S. Morozov, K. S. Novoselov, M. I. Katsnelson, F. Schedin, D. C. Elias, J. A. Jaszczak, and A. K. Geim, “Giant Intrinsic Carrier Mobilities in Graphene and Its Bilayer,” *Phys. Rev. Lett.* **100**, 016 602 (2008).
- [33] P. Kim, L. Shi, A. Majumdar, and P. L. McEuen, “Thermal Transport Measurements of Individual Multiwalled Nanotubes,” *Phys. Rev. Lett.* **87**, 215 502 (2001).
- [34] A. A. Balandin, S. Ghosh, W. Bao, I. Calizo, D. Teweldebrhan, F. Miao, and C. N. Lau, “Superior Thermal Conductivity of Single-Layer Graphene,” *Nano Lett.* **8**, 902–907 (2008).
- [35] M. M. J. Treacy, T. W. Ebbesen, and J. M. Gibson, “Exceptionally High Young’s modulus observed for individual carbon nanotubes,” *Nature* **381**, 678–680 (1996).
- [36] C. Lee, X. Wei, J. W. Kysar, and J. Hone, “Measurement of the Elastic properties and Intrinsic Strength of Monolayer Graphene,” *Science* **321**, 385–388 (2008).
- [37] V. Geringer, M. Liebmann, T. Echtermeyer, S. Runte, M. Schmidt, R. Rückamp, M. C. Lemme, and M. Morgenstern, “Intrinsic and extrinsic corrugation of monolayer graphene deposited on SiO₂,” *Phys. Rev. Lett.* **102**, 076 102 (2009).
- [38] “Scientific Background on the Nobel Prize in Physics 2010,” The Royal Swedish Academy of Sciences (2010).
- [39] S. Reich, C. Thomsen, and J. Maultzsch, *Carbon Nanotubes: Basic Concepts and Physical Properties* (Wiley-VCH Verlag, Weinheim, 2004).
- [40] C. H. Lui, L. Liu, K. F. Mak, G. W. Flynn, and T. F. Heinz, “Ultraflat graphene,” *Nature* **462**, 339–341 (2009).
- [41] P. Avouris, “Graphene: Electronic and Photonic Properties and Devices,” *Nano Lett.* **10**, 4285–4294 (2010).
- [42] A. Geim, “Graphene: Status and Prospects,” *Science* **324**, 1530–1534 (2009).
- [43] F. Bonaccorso, Z. Sun, T. Hasan, and A. C. Ferrari, “Graphene photonics and optoelectronics,” *Nature Photonics* **4**, 611–622 (2010).
- [44] J. Charlier, P. Eklund, J. Zhu, and A. Ferrari, “Electron and Phonon Properties of Graphene: Their Relationship with Carbon Nanotubes,” *Topics Appl. Phys.* **111**, 673–709 (2008).
- [45] R. Martel, T. Schmidt, H. R. Shea, T. Hertel, and P. Avouris, “Single- and multi-wall carbon nanotube field-effect transistors,” *Appl. Phys. Lett.* **73**, 2447–2449 (1998).
- [46] S. J. Tans, A. R. M. Verschueren, and C. Dekker, “Room-temperature transistor based on a single carbon nanotube,” *Nature* **393**, 49–52 (1998).
- [47] L. Vicarelli, M. S. Vitiello, D. Coquillat, A. Lombardo, A. Ferrari, W. Knap, M. Polini, V. Pellegrini, and A. Tredicucci, “Graphene field-effect transistors as room-temperature terahertz detectors,” *Nature Mater.* **11**, 865–871 (2012).
- [48] W. B. Choi, D. S. Chung, J. H. Kang, H. Y. Kim, Y. W. Jin, I. T. Han, Y. H. Lee, J. E. Jung, N. S. Lee, G. S. Park, and J. M. Kim, “Fully sealed, high-brightness carbon-nanotube field-emission display,” *Appl. Phys. Lett.* **75**, 3129–3131 (1999).

- [49] F. Xia, T. Mueller, Y. Lin, A. Valdes-Garcia, and P. Avouris, “Ultrafast graphene photodetector,” *Nature Nanotechnology* **4**, 839–843 (2009).
- [50] T. Mueller, F. Xia, and P. Avouris, “Graphene photodetectors for high-speed optical communications,” *Nature Photonics* **4**, 297–301 (2010).
- [51] F. Xia, T. Mueller, Y. M. Lin, A. Valdes-Garcia, and P. Avouris, “Ultrafast graphene photodetector,” *Nature Nanotech.* **4** (2009).
- [52] X. Wang, L. Zh, and K. Müllen, “Transparent, Conductive Graphene Electrodes for Dye-Sensitized Solar Cells,” *Nano Lett.* **8**, 323–327 (2008).
- [53] Z. Yin, S. Wu, X. Zhou, X. Huang, Q. Zhang, F. Boey, and H. Zhang, “Electrochemical Deposition of ZnO Nanorods on Transparent Reduced Graphene Oxide Electrodes for Hybrid Solar Cells,” *Small* **6**, 307–312 (2010).
- [54] Z. Sun, T. Hasan, F. Torrisi, D. Popa, G. Privitera, F. wang, F. Bonaccorso, D. M. Basko, and A. Ferrari, “Graphene Mode-Locked Ultrafast Laser,” *ACS Nano* **4** (2010).
- [55] P. A. Obraztsov, M. Rybin, A. Tyurnina, S. V. Garnoc, E. D. Obraztsova, O. A. N., and Y. P. Svirko, “Broadband light-induced absorbance change in multilayer graphene,” *Nano Lett.* **11**, 1540–1545 (2011).
- [56] M. A. Gluba, D. Amkreutz, G. V. Troppenz, J. Rappich, and N. H. Nickel, “Embedded graphene for large-area silicon-based devices,” *Appl. Phys. Lett.* **103**, 073 192 (2013).
- [57] K. F. Mak, L. Ju, F. Wang, and T. F. Heinz, “Optical spectroscopy of graphene: From the far infrared to the ultraviolet,” *Solid State Comm.* **152**, 1341–1349 (2012).
- [58] D. Chen, A. Nakahara, W. Dongguang, D. Nordlund, and T. P. Russel, “P3HT/PCBM Bulk Heterojunction Organic Photovoltaics: Correlating Efficiency and Morphology,” *Nano Lett.* **11**, 561–567 (2011).
- [59] L. M. Malard, M. A. Pimenta, G. Dresselhaus, and M. S. Dresselhaus, “Raman spectroscopy in graphene,” *Physics Reports* **473**, 51–87 (2009).
- [60] A. M. Rao, E. Richter, S. Bandow, B. Chase, P. C. Eklund, K. A. Williams, S. Fang, K. R. Subbaswamy, M. Menon, A. Thess, R. E. Smalley, G. Dresselhaus, and M. S. Dresselhaus, “Diameter-Selective Raman Scattering from Vibrational Modes in Carbon Nanotubes,” *Science* **275**, 187–190 (1997).
- [61] A. C. Ferrari, J. C. Meyer, V. Scardaci, C. Casiraghi, F. M. Lazzeri, S. Piscanec, D. Jiang, K. S. Novoselov, S. Roth, and A. K. Geim, “Raman Spectrum of Graphene and Graphene Layers,” *Phys. Rev. Lett.* **97**, 187 401 (2006).
- [62] A. C. Ferrari and D. M. Basko, “Raman spectroscopy as a versatile tool for studying the properties of graphene,” *Nature Nanotech.* **8**, 235–246 (2013).
- [63] D. M. Basko, S. Piscanec, and A. C. Ferrari, “Electron-electron interactions and doping dependence of the two-phonon Raman intensity in graphene,” *Phys. Rev. B* **80**, 165 413 (2009).

-
- [64] H. Yang, X. Feng, Q. Wang, H. Huang, W. Chen, A. Wee, and W. Ji, “Giant Two-Photon Absorption in Bilayer Graphene,” *Nano Lett.* **11**, 2622–2627 (2011).
 - [65] P. A. George, J. Strait, J. Dawlaty, S. Shivaraman, M. Chandrasekhkar, F. Rana, and G. Spencer, “Ultrafast Optical-Pump Terahertz-Probe Spectroscopy of the Carrier Relaxation and Recombination Dynamics in Epitaxial Graphene,” *Nano Lett.* **8**, 4248–4251 (2008).
 - [66] N. Bonini, J. Garg, and N. Marzari, “Acoustic Phonon Lifetimes and Thermal Transport in Free-Standing and Strained Graphene,” *Nano Lett.* **12**, 2673–2678 (2012).
 - [67] T. Li, L. Luo, M. Hupalo, J. Zhang, C. Tringides, J. Schmalian, and J. Wang, “Femtosecond Population Inversion and Stimulated Emission of Dense Dirac Fermions in Graphene,” *Phys. Rev. Lett.* **108**, 167 401 (2012).
 - [68] F. Rana, “Electron-hole generation and recombination rates for Coulomb scattering in graphene,” *Phys. Rev. B* **76**, 155 431 (2007).
 - [69] F. Rana, P. A. George, J. H. Strait, J. Dawlaty, M. Shivaraman, S. Chandrashekar, and M. G. Spencer, “Carrier recombination and generation rates for intravalley and intervalley phonon scattering in graphene,” *Phys. Rev. B* **79**, 115 447 (2009).
 - [70] F. Rana, J. H. Strait, H. Wang, and C. Manolatou, “Ultrafast carrier recombination and generation rates for plasmon emission and absorption in graphene,” *Phys. Rev. B* **84**, 045 437 (2011).
 - [71] R. Kim, V. Perebeinos, and P. Avouris, “Relaxation of optically excited carriers in graphene,” *Phys. Rev. B* **84**, 075 449 (2011).
 - [72] T. Winzer, E. Malic, and A. Knorr, “Microscopic mechanism for transient population inversion and optical gain in graphene,” *Phys. Rev. B* **87**, 165 413 (2013).
 - [73] C. Lui, K. F. Mak, J. Shan, and T. F. Heinz, “Ultrafast Photoluminescence from Graphene,” *Phys. Rev. Lett.* **105**, 127 404 (2010).
 - [74] W.-T. Liu, S. W. Wu, P. J. Schuck, Y. R. Shen, and F. Wang, “Nonlinear broadband photoluminescence of graphene induced by femtosecond laser irradiation,” *Phys. Rev. B* **82**, 081 408–081 412 (2010).
 - [75] R. Stoehr, R. Kolesov, J. Pflaum, and J. Wrachtrup, “Fluorescence of laser created electron-hole plasma in graphene,” *Phys. Rev. B* **82**, 121 408 (2010).
 - [76] E. Malic, T. Winzer, E. Bobkin, and A. Knorr, “Microscopic theory of absorption and ultrafast many-particle kinetics in graphene,” *Phys. Rev. B* **84**, 205 406 (2011).
 - [77] E. Malic, T. Winzer, and A. Knorr, “Efficient orientational carrier relaxation in optically excited graphene,” *Appl. Phys. Lett.* **101**, 213 110 (2012).
 - [78] D. M. Chapin, C. S. Fuller, and G. L. Pearson, “A New Silicon pn Junction Photocell for Converting Solar Radiation into Electrical Power,” *J. Appl. Phys.* **25**, 676 (1954).
 - [79] S. M. Sze, *Physics of semiconductor devices* (Wiley and Sons, London, 1982), 2 edn.
 - [80] J. Connolly and D. Mencaraglia, “III-V Solar Cells,” *arXiv* **1301.1278** (2013).

- [81] M. A. Green, “Crystalline and thin-film silicon solar cells: state of the art and future potential,” *Sol. Energy* **74**, 181–192 (2003).
- [82] D. E. Carlson and C. R. Wronski, “Amorphous silicon solar cell,” *Appl. Phys. Lett.* **28**, 671 (1976).
- [83] M. Grätzel, “Dye-sensitized solar cells,” *Photochemistry Reviews, J. of Photochemistry and Photobiology C: Photochemistry Reviews* **4**, 145–153 (2003).
- [84] D. Wöhrle and D. Meissner, “Organic solar cells,” *Adv. Mat.* **3**, 3 (1991).
- [85] R. R. King, D. C. Law, K. M. Edmondson, C. M. Fetzer, G. S. Kinsey, H. yoon, R. A. Sherif, and N. H. Karam, “40% efficient metamorphic GaInP/GaInAs/Ge multijunction solar cells,” *Appl. Phys. Lett.* **90**, 183 516 (2007).
- [86] M. S. Leite, R. L. Woo, J. N. Munday, W. D. Hong, S. Mesropian, D. C. Law, and H. A. Atwater, “Towards an optimized all lattice-matched InAlAs/InGaAsP/InGaAs multijunction solar cell with efficiency >50%,” *Appl. Phys. Lett.* **102**, 033 901 (2013).
- [87] H. Hoppe and N. S. Sariciftci, “Organic solar cells: An overview,” *J. Mater. Res.* **19**, 1924–1945 (2004).
- [88] S. A. Akhmanov, V. A. Vysloukh, and A. S. Chirkin, *Optics of Femtosecond Laser Pulses* (American Institute of Physics, New York, USA, 1992), 1 edn.
- [89] R. W. Boyd, *Nonlinear Optics* (Academic Press, Elsevier, Corporate Drive, Suite 400, Burlington, MA 01803, USA, 2008).
- [90] G. S. Smith, *An Introduction to Classical Electromagnetic Radiation* (Cambridge University Press, The Edinburgh Building, Cambridge CB2 2RU, UK, 1997), 1 edn.
- [91] T. Brixner and G. Gerber, “Femtosecond polarization pulse shaping,” *Optics Letters* **26**, 557–559 (2001).
- [92] A. M. Weiner, “Femtosecond pulse shaping using spatial light modulators,” *Rev. Sci. Instrum.* **71**, 1929 (2000).
- [93] S. Aktürk, “Extending Ultrashort-Laser-Pulse Measurement Techniques To New Dimesnions, Time Scales, and Frequencies,” School of Physics, Gerogia Institute of Technology p. Dissertation (2005).
- [94] A. Monmayrant, S. Weber, and B. Chatel, “A newcomer’s guide to ultrashort pulse shaping and characterization,” *J. of Phys. B* **43**, 103 001 (2010).
- [95] J. A. Voll, “Quanten-Kontroll-Spektroskopie photochemischer Prozesse in biologischen Modellsystemen,” Dissertation LMU Munich (2010).
- [96] G. Piredda, C. Gollub, R. de Vivie-Riedle, and A. Hartschuh, “Controlling near-field optical intensities in metal nanoparticle systems by polarization pulse shaping,” *Applied Physics B* **100**, 195–206 (2010).
- [97] A. Villamarin, I. J. Sola, M. V. Collados, J. Atencia, O. Varela, B. Alonso, C. Mendez, J. san Roman, I. Arias, L. Roso, and M. Quintanilla, “Compensation of second-order dispersion in femtosecond pulses after filamentation using volume holographic transmission gratings recorded in dichromated gelatin,” *Appl. Phys. B* **106**, 135–141 (2012).

-
- [98] J. M. Gunn, M. Ewald, and M. Dantus, “Polarization and Phase Control of Remote Surface-Plasmon-Mediated Two-Photon-Induced Emission and Waveguiding,” *Nano Lett.* **6**, 2804–2809 (2006).
- [99] M. Dantus and V. Lozovoy, “Experimental Coherent Laser Control of Physicochemical Processes,” *Chem. Rev.* **104**, 1813–1859 (2004).
- [100] F. J. Duarte, “Generalized multiple-prism dispersion theory for laser pulse compression: higher order phase derivatives,” *Appl. Phys. B* **96**, 809–814 (2009).
- [101] F. J. Duarte, “Prismatic pulse compression: beam deviations and geometrical perturbations,” *Optical and Quantum Electronics* **22**, 467–471 (1990).
- [102] V. K. Chauhan, J. Cohen, P. M. Vaughan, P. Bowlan, and R. Trebino, “Distortion-Free Single-Prism/Grating Ultrashort Laser Pulse Compressor,” *IEEE Journal of Quantum Electronics* **46**, 1726–1731 (2010).
- [103] R. Szipocs and A. Kohazi-Kis, “Theory and design of chirped dielectric laser mirrors,” *Appl. Phys. B* **65**, 115–135 (1997).
- [104] G. Steinmeyer, “A review of ultrafast optics and optoelectronics,” *J. Opt. A: Pure Appl. Optics* **5**, R1–R5 (2003).
- [105] K. Ohmori, Y. Sato, E. E. Nikitin, and S. Rice, “Highprecision molecular wavepacket interferometry with HgAr dimers,” *Phys. Rev. Lett.* **91**, 243 003 (2003).
- [106] M. Lindberg and S. W. Koch, “Effective Bloch equations for semiconductors,” *Phys. Rev. B* **38**, 3342–3350 (1988).
- [107] A. Stahl and I. Balsev, *Electrodynamics of the Semiconductor Band Edge*, Vol. 110 (Springer, Berlin, 1987).
- [108] C. Klingshirn and H. Haug, *Optical Nonlinearities and Instabilities in Semiconductors* (Academic, New York, 1988).
- [109] K. Zimmermann, K. Kilimann, W. D. Kraeft, D. Kremp, and C. Röpke, “Dynamical screening and self-energy of excitons in the electron hole plasma,” *Phys. Status Solidi B* **90**, 175 (1978).
- [110] T. Winzer, E. Malic, and A. Knorr, *Low-Dimensional Functional Materials* (Springer, Berlin, 2013).
- [111] S. Winnerl, M. Orlita, P. Plochocka, P. Kossacki, M. Potemski, T. Winzer, E. Malic, A. Knorr, M. Sprinkle, C. Berger, W. A. de Heer, H. Schneider, and M. Helm, “Carrier Relaxation in Epitaxial Graphene Photoexcited Near the Dirac Point,” *Phys. Rev. Lett.* **107**, 237 401–237 406 (2011).
- [112] T. Winzer, “Ultrafast Carrier Relaxation Dynamics in Graphene,” Dissertation Technischen Universität Berlin (2013).
- [113] T. Gokus, “Time-Resolved Photoluminescence and Elastic White Light Scattering Studies of Individual Carbon Nanotubes and Optical Characterization of Oxygen Plasma Treated Graphene,” Dissertation LMU munich (2011).
- [114] K. R. Spring and M. W. Davidson, “Concepts in Digital Imaging Technology: Avalanche Photodiodes,” learn.hamamatsu.com/articles/avalanche.html (2006).

- [115] D. Renker and E. Lorenz, “Advances in solid state photon detectors,” *J. Inst.* **4**, 04 004 (2009).
- [116] “US Patent 3,792,322,” (1974).
- [117] W. S. Boyle and G. E. Smith, “B.S.T.J. Briefs: Charge Coupled Semiconductor Devices,” *Bell Sys. Tech. J.* **49**, 587–593 (1970).
- [118] N. Calandar, “Leakage radiation microscopy,” *Anal. Chem.* **76**, 2168–2173 (2004).
- [119] A. Bouhelier, T. Huser, H. Tamaru, H.-J. Günterodt, and D. W. Pohl, “Plasmon optics of structured silver films,” *Phys. Rev. B* **63**, 155 404 (2001).
- [120] N. Hartmann, G. Piredda, J. Berthelot, G. Colas des Francs, A. Bouhelier, and A. Hartschuh, “Launching Propagating Surface Plasmon Polaritons by a Single Carbon Nanotube Dipolar Emitter,” *Nano Lett.* **12**, 177–181 (2012).
- [121] O. Mollet, S. Huant, and A. Drezet, “Scanning plasmonic microscopy by image reconstruction from the Fourier space,” .
- [122] A. Hohenau, J. R. Krenn, A. Drezet, O. Mollet, S. Huant, C. Genet, B. Stein, and T. W. Ebbesen, “Surface plasmon leakage radiation microscopy at the diffraction limit,” *Optics Express* **19**, 25 749–25 762 (2011).
- [123] A. Drezet, A. Hohenau, D. Koller, A. Stephanov, H. Ditlbacher, B. Steinberger, F. R. Aussenegg, A. Leitner, and J. Krenn, “Leakage radiation microscopy of surface plasmon polaritons,” *Materials Science and Engineering: B* **149**, 220–229 (2008).
- [124] A. Archambault, T. Teperik, F. Marquier, and J. Greffet, “Surface plasmon Fourier optics,” *Phys. Rev. B* **79**, 195 414 (2009).
- [125] N. Hartmann, *Coupling of Emitters to Surface Plasmons Investigated by Back Focal Plane Microscopy* (2013).
- [126] *The bh TCSPC Handbook* (Becker&Hickl GmbH, 12277 Berlin, 2008), 3 edn.
- [127] L. M. Bollinger and G. E. Thomas, “Measurement of the Time Dependence of Scintillation Intensity by a Delayed-Coincidence Method,” *Rev. Sci. Instrum.* **32**, 1044 (1961).
- [128] D. V. O’Connor and D. Phillips, *Time Correlated Single Photon Counting* (Academic Press, London, 1984).
- [129] C. Fröhly, B. Colombeau, and V. M., “Shaping and analysis of picosecond light pulses,” *Prog. opt.* **20**, 65–153 (1983).
- [130] B. Xu, J. M. Gunn, J. M. Dela Cruz, V. V. Lozovoy, and M. Dantus, “Quantitative investigation of the MIIPS method for phase measurement and compensation of femtosecond laser pulses,” *J. Opt. Soc. Am. B* **23**, 750–759 (2006).
- [131] J. M. Dela Cruz, I. Pastirk, V. V. Lozovoy, K. A. Walowicz, and M. Dantus, “Multiphoton Intrapulse Interference 3: Probing Microscopic Chemical Environments,” *J. Phys. Chem. A* **108**, 53–58 (2004).

-
- [132] M. Hacker, R. Netz, M. Roth, G. Stobrawa, T. Feurer, and R. Sauerbrey, "Frequency doubling of phase-modulated, ultrashort laser pulses," *Appl. Phys. B* **73**, 273–277 (2001).
- [133] K. A. Walowicz, I. Pastirk, V. V. Lozovoy, and M. Dantus, "Multiphoton Intrapulse Interference 1: Control of Multiphoton Processes in Condensed Phases," *J. Phys. Chem. A* **106**, 9369–9373 (2002).
- [134] L. Bonacina, Y. Mugnier, F. Courvoisier, R. L. Dantec, J. Extermann, Y. Lambert, V. Boutou, C. Galez, and J. Wolf, "Polar $\text{Fe}(\text{IO}_3)_3$ nanocrystals as local probes for nonlinear microscopy," *Appl. Phys. B* **87**, 399 (2007).
- [135] M. Handloser, R. Dunbar, P. Altpeter, C. Scheu, L. Schmidt-Mende, and A. Hartschuh, "Influence of metallic and dielectric nanowire array on the photoluminescence properties of P3HT thin films," *Nanotechnology* **23**, 305 402–305 408 (2012).
- [136] C. Brabec, V. Dyakonov, J. Parisi, and N. S. Sariciftci, *Organic Photovoltaics* (Springer, Berlin, 2007), 2 edn.
- [137] U. Zhokhavets, T. Erb, G. Gobsch, M. Al-Ibrahim, and O. Ambacher, "Relation between absorption and crystallinity of poly(3-hexylthiophene)/fullerene films for plastic solar cells," *Chem. Phys. Lett.* **418**, 347–350 (2006).
- [138] J. E. Kröze, T. J. Savenije, M. J. W. Vermeulen, and J. W. Warman, "Contactless Determination of the Photoconductivity Action Spectrum, Exciton Diffusion Length, and Charge Separation Efficiency in Polythiophene-Sensitized TiO_2 Bilayers," *Phys Chem. B* **107**, 7696–7705 (2003).
- [139] D. Duche, E. Drouard, J. Simon, L. Escoubas, P. Torchio, J. Le Rouzo, and S. Vedraïne, "Light harvesting in organic solar cells," *Sol. En. Mat.* **95**, 18–25 (2011).
- [140] S. D. Oosterhout, M. M. Wienk, S. S. Bavel, R. Thiedmann, L. J. A. Koster, J. Gilot, J. Loos, V. Schmidt, and R. A. J. Janssen, "The effect of three-dimensional morphology on the efficiency of hybrid polymer solar cells," *Nat. Mat.* **8**, 818–824 (2009).
- [141] A. R. Marsh, J. M. Hodgkiss, S. Albert-Seifried, and R. H. Friend, "Effect of Annealing on P3HT:PCBM Charge Transfer and Nanoscale Morphology Probed by Ultrafast Spectroscopy," *Nano Lett.* **10**, 923–930 (2010).
- [142] J. W. P. Hsu and M. T. Lloyd, "Organic/Inorganic Hybrids for Solar Energy Generation," *MRS Bulletin*. **35**, 422–428 (2010).
- [143] M. D. McGehee, "Nanostructured Organic-Inorganic Hybrid for Solar Cells," *MRS Bulletin*. **34**, 95–100 (2009).
- [144] M. F. Calhoun, "Electronic functionalization of the surface of organic semiconductors with self-assembled monolayers," *Nat. Mat.* **7**, 84–89 (2008).
- [145] R. B. Dunbar, H. C. Hesse, D. S. Lembke, and L. Schmidt-Mende, "Light-trapping plasmonic nanovoid arrays," *Phys. Rev. B* **85**, 035 301 (2012).
- [146] M. A. Mahmoud, A. J. Poncheri, R. L. Phillips, and M. A. El-Sayed, "Plasmonic Field Enhancement of the Exciton-Exciton Annihilation Process in a Poly(p-phenyleneethynylene) Fluorescent Polymer by Ag Nanocubes," *J. Am. Chem. Soc.* **132**, 2633–2641 (2010).

- [147] J. A. Schuller, E. S. Barnard, W. Cai, Y. Chul Jun, J. S. White, and M. L. Brongersma, "Plasmonics for extreme light concentration and manipulation," *Nat. Mat.* **9**, 193–204 (2010).
- [148] D. H. Wang, K. H. Park, J. H. Seo, J. Seifter, J. H. Jeon, J. Kim, J. H. Park, O. O. Park, and A. Heeger, "Enhanced Power Conversion Efficiency in PCDTBT/PC₇₀ BM Bulk Heterojunction Photovoltaic Devices with Embedded Silver Nanoparticle Clusters," *Adv. En. Mat.* **1**, 766–770 (2011).
- [149] V. E. Ferry, L. A. Sweatlock, D. Pacifici, and H. A. Atwater, "Plasmonic Nanostructure Design for Efficient Light Coupling into Solar Cells," *Nano Lett.* **8**, 4391–4397 (2008).
- [150] S. Trotzky, T. Hoyer, W. Tuszynski, C. Lienau, and J. Parisi, "Femtosecond up-conversion technique for probing the charge transfer in a P3HT:PCBM blend via photoluminescence quenching," *J. Phys. D. Appl. Phys.* **42**, 055 105 (2009).
- [151] R. R. Chance, A. Prock, and R. Silbey, "Lifetime of an excited molecule near a metal mirror: Energy transfer in the Eu³⁺/ silver system," *J. Chem. Phys.* **60**, 2184–2185 (1974).
- [152] U. Gomez, H. Port, and H. Wolf, "Fluorescence quenching of ultrathin MePTCDI films by inorganic substrates," *J. of Lum.* **72-74**, 496–498 (1997).
- [153] S. Cook, A. Furube, and R. Katoh, "Analysis of the excited states of regioregular polythiophene P3HT," *Energy Environ. Sci.* **1**, 294–299 (2008).
- [154] L. Magnani, G. Rumbles, I. Samuel, K. Murray, S. Moratti, A. Holmes, and R. Friend, "Photoluminescence studies of chain interactions in electroluminescent polymers," *Synthetic Metals* **84**, 899–900 (1997).
- [155] B. Kraabel, D. Moses, and A. Heeger, "Direct observation of the intersystem crossing in poly(3-octylthiophene)," *J. Chem. Phys.* **103**, 5102 (1995).
- [156] J. A. Labastide, M. Baghgar, I. Dujovne, H. B. Venkatraman, D. C. Ramsdell, D. Venkataraman, and M. D. Barnes, "Time- and Polarization-Resolved Photoluminescence of Individual Semicrystalline Polythiophene (P3HT) Nanoparticles," *Phys Chem. Lett.* **2**, 2089–2093 (2009).
- [157] S. van Bavel, E. Sourty, G. de With, K. Frolic, and J. Loos, "Relation between Photoactive Layer Thickness, 3D Morphology, and Device Performance in P3HT/PCBM Bulk-Heterojunction Solar Cells," *Macromolecules* **42**, 7396–7403 (2009).
- [158] D. Olson, J. Piris, R. Collins, S. Shaheen, and D. Ginley, "Hybrid photovoltaic devices of polymer and ZnO nanofiber composites," *Thin Solid Films* **496**, 26–29 (2006).
- [159] M. Aryal, K. Trivedi, and W. Hu, "Nano-Confinement Induced Chain Alignment in Ordered P3HT Nanostructures Defined by Nanoimprint Lithography," *ACS Nano* **3**, 3085–3090 (2009).
- [160] C. Melis, L. Colombo, and A. Mattoni, "Self-Assembling of Poly(3-hexylthiophene)," *J. Phys. Chem.C* **115**, 576–581 (2011).

-
- [161] M. Dogru, M. Handloser, F. Auras, T. Kunz, D. Medina, A. Hartschuh, P. Knochel, and T. Bein, "A Photoconductive Thienothiophene-Based Covalent Organic Framework Showing Charge Transfer Towards Included Fullerene," *Angew. Chem. Int. Ed.* **52**, 2920–2924 (2013).
- [162] A. P. Cote, A. I. Benin, N. W. Ockwig, M. O’Keeffe, A. J. Matzger, and O. M. Yaghi, "Porous, Crystalline, Covalent Organic Frameworks," *Science* **310**, 1166–1170 (2005).
- [163] H. M. El-Kaderi, J. Hunt, J. Mendoza-Cortès, A. Cotè, R. Taylor, M. O’Keeffe, and O. M. Yaghi, "Designed Synthesis of 3D Covalent Organic Frameworks," *Science* **316**, 268–272 (2007).
- [164] A. P. Cotè, H. M. El-Kaderi, H. Furukawa, and O. M. Hunt, J.H. and Yaghi, "Reticular Synthesis of Microporous and Mesoporous 2D Covalent Organic Frameworks," *J. Am. Chem. Soc.* **129**, 12 914–12 915 (2007).
- [165] E. L. Spitler, B. T. Koo, J. L. Novotney, J. W. Colson, F. J. Uribe-Romo, G. D. Gutierrez, P. Clancy, and W. R. Dichtel, "A 2D Covalent Organic Framework with 4.7-nm Pores and Insight into Its Interlayer Stacking," *J. Am. Chem. Soc.* **133**, 19 416–19 421 (2011).
- [166] E. Spitler, C. J. W., J. Uribe-Romo, A. R. Woll, M. R. Giovino, A. Saldivar, and W. . Dichtel, "Lattice Expansion of Highly Oriented 2D Phthalocyanine Covalent Organic Framework Films," *Angew. Chem. Int. Ed.* **51**, 2623–2627 (2012).
- [167] S. Wan, J. Guo, J. Kim, H. Ihee, and D. Jiang, "A Belt-Shaped, Blue Luminescent, and Semiconducting Covalent Organic Framework," *Angew. Chem. Int. Ed.* **48**, 3207 (2009).
- [168] S. Wan, J. Guo, J. Kim, H. Ihee, and D. Jiang, "A Photoconductive Covalent Organic Framework: Self-Condensed Arene Cubes Composed of Eclipsed 2D Polypyrene Sheets for Photocurrent Generation," *Angew. Chem. Int. Ed.* **48**, 5439–5442 (2009).
- [169] X. Ding, J. Guo, X. Feng, Y. Honsho, J. Guo, S. Seki, P. Maitarad, A. Saeki, S. Nagase, and D. Jiang, "Synthesis of Metallophthalocyanine Covalent Organic Frameworks That Exhibit High Carrier Mobility and Photoconductivity," *Angew. Chem. Int. Ed.* **50**, 1289–1293 (2011).
- [170] S. Wan, F. Gandara, A. Asano, H. Furukawa, A. Saeki, S. K. Dey, L. Liao, M. W. Ambrogio, Y. Y. Botros, X. Duan, S. Seki, J. Stoddart, and O. M. Yaghi, "Covalent Organic Frameworks with High Charge Carrier Mobility," *Chem. Mater.* **23**, 4094–4097 (2011).
- [171] C. deibel and V. Dyakonov, "Polymer-Fullerene Bulk-Heterojunction Solar Cells," *Rep. Prog. Phys* **73**, 096 401 (2010).
- [172] G. Yu, J. Gao, J. C. Hummelen, F. Wudl, and A. J. Heeger, "Polymer Photovoltaic Cells: Enhanced Efficiencies via a Network of Internal Donor-Acceptor Heterojunctions," *Science* **270**, 1789–1791 (1995).
- [173] J. Peet, J. Y. Kim, N. E. Coates, W. L. Ma, D. Moses, A. J. Heeger, and G. C. Bazan, "Efficiency enhancement in low-bandgap polymer solar cells by processing with alkane dithiols," *Nature* **6**, 497–500 (2007).

- [174] "Accelrys MS Modeling 4.4," (2008).
- [175] W. R. Tilford, R. W. and Gemmill, H.-C. zur Loye, and J. J. Lavigne, "Facile Synthesis of a Highly Crystalline, Covalently Linked Porous Boronate Network," *Chem. Mater.* **18**, 497–500 (2006).
- [176] A. R. Leach, *Molecular Modelling: Principles and Applications*, (Prentice Hall, Harlow UK, 2007), 2 edn.
- [177] M. Heeney, C. Bailey, K. Genevicius, M. Shkunov, D. Sparrowe, S. Tierney, and I. McCulloch, "Stable Polythiophene Semiconductors Incorporating Thieno[2,3-b]thiophene," *J. Am. Chem. Soc.* **127**, 1078–1079 (2005).
- [178] T. J. Savenije, W. J. Grzegorzczuk, M. Heeney, S. Tierney, I. McCulloch, and L. D. A. Siebbeles, "Photoinduced Charge Carrier Generation in Blends of Poly(Thienothiophene) Derivatives and [6,6]-Phenyl-C61-butyric Acid Methyl Ester: Phase Segregation versus Intercalation," *J. Phys. Chem. C.* **114**, 15 116–15 120 (2010).
- [179] N. S. Sariciftci, L. Smilowitz, A. J. Heeger, and F. Wudl, "Photoinduced Electron Transfer from a Conducting Polymer to Buckminsterfullerene," *Science* **258**, 1474–1476 (1992).
- [180] A. Wochnik, M. Handloser, D. Durach, A. Hartschuh, and C. Scheu, "Increasing Crystallinity for Improved Electrical Conductivity of TiO₂ Blocking Layers," *ACS Applied Materials and Interfaces* **12**, 5696–5699 (2013).
- [181] Y. U. Ahn, E. J. Kim, H. T. Kim, and S. H. Hahn, "Variation of structural and optical properties of sol-gel TiO₂ thin films with catalyst concentration and calcination temperature," *Mater. Lett.* **57**, 4660–4666 (2003).
- [182] H. Yu, S. Zhang, H. Zhao, G. Will, and P. Liu, "An efficient and low-cost TiO₂ compact layer for performance improvement of dye-sensitized solar cells," *Electrochim. Acta* **54**, 1319–1324 (2009).
- [183] K.-I. Jang, E. Hong, and J. H. Kim, "Effect of an electrodeposited TiO₂ blocking layer on efficiency improvement of dye-sensitized solar cell," *Korean J. Chem. Eng* **29**, 356–361 (2012).
- [184] F. Lenzmann, M. Nau, O. Kijatkina, and A. Belaidi, "Substantial improvement of the photovoltaic characteristics of TiO₂/CuInS₂ interfaces by the use of recombination barrier coatings," *Thin Solid Films* **451-452**, 639–643 (2004).
- [185] A. Burke, S. Ito, H. Snaith, U. Bach, J. Kwiakowski, and M. Grätzel, "The Function of a TiO₂ Compact Layer in Dye-Sensitized Solar Cells Incorporating "Planar" Organic Dyes," *Nano Lett.* **8**, 977–981 (2008).
- [186] T.-Y. Cho, S.-G. Yoon, S.-S. Sekhon, M. G. Kang, and C.-H. Han, "The Effect of a Sol-gel formed TiO₂ Blocking Layer on the Efficiency of Dye-sensitized Solar Cells," *Bull. Korean Chem. Soc.* **32**, 3629–3633 (2011).
- [187] A. Yildiz, S. B. Lisesivdin, M. Kasap, and D. Mardare, "Electrical properties of TiO₂ thin films," *J. Non-Cryst. Solids* **354**, 4944–4947 (2008).

-
- [188] J. Aarik, A. Aidla, A.-A. Kiisler, T. Uustare, and V. Sammelselg, "Effect of crystal structure on optical properties of TiO₂ films grown by atomic layer deposition," *Thin Solid Films* **305**, 270–273 (1997).
- [189] P. Cameron and L. Peter, "Characterization of Titanium Dioxide Blocking Layers in Dye-Sensitized Nanocrystalline Solar Cells," *J. Phys. Chem. B* **107**, 14 394–14 400 (2003).
- [190] B. Peng, G. Jungmann, C. Jäger, D. Haarer, H.-W. Schmidt, and M. Thelakkat, "Systematic investigation of the role of compact TiO₂ layer in solid state dye-sensitized TiO₂ solar cells," *Coord. Chem.-Rev.* **248**, 1479–1489 (2004).
- [191] R. Mechiakh, N. Ben Sedrine, R. Chtourou, and R. Bensaha, "Correlation between microstructure and optical properties of nano-crystalline TiO₂ thin films prepared by sol-gel dip coating," *Appl. Surf. Sci.* **257**, 670–676 (2010).
- [192] C. Jiang, M. Leung, W. L. Koh, and Y. Li, "Influences of deposition and post-annealing temperatures on properties of TiO₂ blocking layer prepared by spray pyrolysis for solid-state dye-sensitized solar cells," *Thin Solid Films* **519**, 7850–7854 (2011).
- [193] H. Sun, J. Weickert, H. Hesse, and L. Schmidt-Mende, "Effects of solvent on properties of sol-gel-derived titanium dioxide coating films," *Thin Solid Films* **219**, 18–23 (1992).
- [194] A. Yildiz, S. B. Lisesivdin, M. Kasap, and D. Mardare, "Electrical properties of TiO₂ thin films," *Journal of Non-Crystalline Solids* **354**, 4944–4947 (2008).
- [195] P. Chrysicopoulou, D. Davazoglou, C. Trapalis, and G. Kordas, "Optical properties of very thin (<100 nm) sol-gel TiO₂ films," *Thin Solid Films* **323**, 188–193 (1998).
- [196] L. L. Hench and J. K. West, "The Sol-Gel Process," *Chem. Rev.* **90**, 33–72 (1990).
- [197] C. Chang, L. Cheng, C. Lin, and Y. Yu, "Preparation and characterization of TiO₂ sols and their UV-cured hybrid thin films on plastic substrates," *J. Sol-Gel Sci. Technol.* **63**, 30–35 (2012).
- [198] Y. Hu, H. Tsai, and C. Huang, "Phase transformation of precipitated TiO₂ nanoparticles," *Mater. Sci. Eng.* **A344**, 209–214 (2003).
- [199] B. Mandlmeier, J. Szeifert, D. Fattakhova-Rohlfing, H. Amenitsch, and T. Bein, "Formation of Interpenetrating Hierarchical Titania Structures by Confined Synthesis in Inverse Opal," *J. Am. Chem. Soc.* **133**, 17 274–17 282 (2011).
- [200] M. Rawolle, M. A. Niedermeier, G. Kaune, J. Perlich, P. Lellig, M. Memesa, Y.-J. Cheng, J. S. Gutmann, and P. Müller-Buschbaum, "Fabrication and characterization of nanostructured titania films with integrated function from inorganic-organic hybrid materials," *Chem. Soc. Rev.* **41**, 5131–5142 (2012).
- [201] M. C. Orilall and U. Wiesner, "Block copolymer based composition and morphology control in nanostructured hybrid materials for energy conversion and storage: solar cells, batteries, and fuel cells," *Chem. Soc. Rev.* **40**, 520–535 (2011).

- [202] M. Rawolle, E. V. Braden, M. A. Niedermeier, D. Magerl, K. Sarkar, T. Fröschl, N. Hüsing, J. Perlich, and P. Müller-Buschbaum, “Low-Temperature Route to Crystalline Titania Network Structures in Thin Films,” *Chem. Phys. Chem.* **13**, 2412–2417 (2012).
- [203] A. Stecker, U. Salzberger, and J. Mayer, “Specimen preparation for TEM. Reliable method for cross-sections and brittle materials,” *Prakt. Metallogr.* **30**, 482–495 (1993).
- [204] Y. Yang, L. Wang, H. Yan, T. J. Marks, and S. Li, “Highly transparent and conductive double-layer oxide thin films as anodes for organic light-emitting diodes,” *Appl. Phys. Lett.* **89**, 051116 (2006).
- [205] G. Reiss, J. Vancea, and H. Hoffmann, “Grain-Boundary Resistance in Polycrystalline Metals,” *Phys. Rev. Lett.* **56**, 2100–2103 (1986).
- [206] J. Vancea, H. Hoffmann, and K. Kastner, “Mean free path and effective density of conduction electrons in polycrystalline metal films,” *Thin Solid Films* **121**, 201–216 (1984).
- [207] J. Vancea and H. Hoffmann, “Reduced density of effective electrons in metal films,” *Thin Solid Films* **92**, 219–225 (1982).
- [208] Y. Cao, T. He, Y. Chen, and Y. Cao, “Fabrication of Rutile TiO₂-Sn/Anatase TiO₂N Heterostructure and Its Application in Visible-Light Photocatalysis,” *The Journal of Physical Chemistry C* **114**, 3627–3633 (2010).
- [209] C. A. Gueymard, D. Myers, and K. Emery, “Proposed reference irradiance spectra for solar energy systems testing,” *Solar Energy* **73**, 443–467 (2002).
- [210] W. H. Howie, F. Claeysens, H. Miura, and L. M. Peter, “Characterization of Solid-State Dye-Sensitized Solar Cells Utilizing High Absorption Coefficient Metal-Free Organic Dyes,” *Journal of the American Chemical Society* **130**, 1367–1375 (2008).
- [211] L. Magnani, G. Rumbles, I. D. W. Samuel, K. Murray, S. C. Moratti, A. B. Holmes, and R. H. Friend, “Photoluminescence studies of chain interactions in electroluminescent polymers,” *Synthetic Metals* **84**, 899–900 (1997).
- [212] M. C. Chen, D. J. Liaw, Y. C. Huang, H. Y. Wu, and Y. Tai, “Improving the efficiency of organic solar cell with a novel ambipolar polymer to form ternary cascade structure,” *Solar Energy Materials and Solar Cells* **95**, 2621–2627 (2011).
- [213] Y. Chen, H. Shih, C. Wang, C. Hsieh, C. Chen, Y. Chen, and T. Lin, “Ultraviolet electroluminescence from hybrid inorganic/organic ZnO/GaN/poly(3-hexylthiophene) dual heterojunctions,” *Opt. Express* **19**, A319–A325 (2011).
- [214] M. M. Stylianakis, E. Stratakis, E. Koudoumas, E. Kymakis, and S. H. Anastasiadis, “Organic Bulk Heterojunction Photovoltaic Devices Based on Polythiophene-Graphene Composites,” *ACS Applied Materials & Interfaces* **4**, 4864–4870 (2012).
- [215] M. Baghgar, J. Labastide, F. Bokel, I. Dujovne, A. McKenna, A. M. Barnes, E. Pentzer, T. Emrick, R. Hayward, and M. D. Barnes, “Probing Inter- and Intrachain Exciton Coupling in Isolated Poly(3-hexylthiophene) Nanofibers: Effect of Solvation and Regioregularity,” *The Journal of Physical Chemistry Letters* **3**, 1674–1679 (2012).

-
- [216] H. Yamagata and F. C. Spano, “Interplay between intrachain and interchain interactions in semiconducting polymer assemblies: The HJ-aggregate model,” *The Journal of Chemical Physics* **136**, 184 901 (2012).
- [217] M. Jones, S. L. Shun, and G. D. Scholes, “Quantitative modeling of the role of surface traps in CdSe/CdS/ZnS nanocrystal photoluminescence decay dynamics,” *PNAS* **106**, 3011–3016 (2001).
- [218] M. Breusing, C. Ropers, and T. Elsaesser, “Ultrafast Carrier Dynamics in Graphite,” *Phys. Rev. Lett.* **102**, 086 809 (2009).
- [219] F. T. Vasko and O. G. Balev, “Spectral and polarization dependencies of luminescence by hot carriers in graphene,” *Phys. Rev. B* **82**, 165 449 (2010).
- [220] M. Freitag, H.-Y. Chiu, M. Steiner, V. Perebeinos, and P. Avouris, “Thermal infrared emission from biased graphene,” *Nature Nanotechnology* **5**, 497–501 (2010).
- [221] T. Nihira and T. Iwata, “Temperature dependence of lattice vibrations and analysis of the specific heat of graphite,” *Phys. Rev. B* **68**, 134 305 (2003).
- [222] O. G. Balev and F. T. Vasko, “Hot carriers in a bipolar graphene,” *Journal of Applied Physics* **107**, 124 312 (2010).
- [223] K. S. Novoselov¹, A. K. Geim, S. V. Morozov, D. Jiang, M. I. Katsnelson, I. V. Grigorieva, S. V. Dubonos, and A. A. Firsov, “Two-dimensional gas of massless Dirac fermions in graphene,” *Nature* **438**, 197–200 (2005).
- [224] W.-T. Liu, S. W. Wu, P. J. Schuck, M. Salmeron, Y. R. Shen, and F. Wang, “Non-linear broadband photoluminescence of graphene induced by femtosecond laser irradiation,” *Phys. Rev. B* **82**, 081 408(R) (2010).
- [225] P. Y. Yu and M. Cardona, *Fundamentals of Semiconductors* (Springer, New York, 1996), 1 edn.
- [226] R. R. Nair, P. Blake, A. N. Grigorenko, K. S. Novoselov, T. J. Booth, T. Stauber, N. M. R. Peres, and A. K. Kein, “Fine structure Constant Defines Visual Transparency of Graphene,” *Science* **320**, 1308 (2008).
- [227] A. C. Ferrari, J. C. Meyer, V. Scardaci, C. Casiraghi, M. Lazzeri, F. Mauri, S. Piscanec, D. Jiang, K. S. Novoselov, S. Roth, and A. K. Geim, “Raman Spectrum of Graphene and Graphene Layers,” *Phys. Rev. Lett.* **97**, 187 401 (2006).
- [228] C. Casiraghi, A. Hartschuh, H. Qian, S. Piscanec, C. Georgi, A. Fasoli, K. S. Novoselov, D. M. Basko, and A. C. Ferrari, “Raman Spectroscopy of Graphene Edges,” *Nano Lett.* **9**, 1433–1441 (2009).
- [229] C. Thomsen and S. Reich, “Double Resonant Raman Scattering in Graphite,” *Phys. Rev. Lett.* **85**, 5214–5217 (2000).
- [230] A. Das, S. Pisana, B. Chakraborty, S. Piscanec, S. K. Saha, U. V. Waghmare, K. S. Novoselov, H. Krishnamurthy, A. K. Geim, A. C. Ferrari, and A. K. Sood, “Monitoring dopants by Raman scattering in an electrochemically top-gated graphene transistor,” *Nature Nanotech.* **3**, 210–215 (2008).

- [231] A. Jorio, R. Saito, J. H. Hafner, C. M. Lieber, M. Hunter, T. McClure, G. Dresselhaus, and M. Dresselhaus, “Structural (n,m) determination of isolated single-wall carbon nanotubes by Resonant Raman Scattering,” *Phys. Rev. Lett.* **86**, 1118–1121 (2001).
- [232] N. Anderson, P. Anger, A. Hartschuh, and L. Novotny, “Subsurface Raman Imaging with Nanoscale Resolution,” *Nano Lett* **6**, 744–749 (2006).
- [233] N. Hayazawa, Y. Inouye, Z. Sekkat, and S. Kawata, “Near-field Raman Scattering enhanced by a metallized tip,” *Chem. Phys. Lett.* **335**, 369–374 (2001).
- [234] F. Tuinstra and J. L. Koenig, “Raman Spectrum of Graphite,” *J. Chem. Phys.* **53**, 1126–1130 (1970).
- [235] K. S. Novoselov, D. Jiang, F. Schedin, T. Booth, V. V. Khotkevich, S. V. Morozov, and A. K. Geim, “Two-dimensional atomic crystals,” *Proc. Nat. Acad. Sci* **102**, 10 451–10 453 (2005).
- [236] C. Casiraghi, A. Hartschuh, H. Lidorikis, H. Qian, H. Harutyunyan, T. Gokus, K. Novoselov, and A. Ferrari, “Rayleigh Imaging of Graphene and Graphene Layers,” *Nano Lett.* **7**, 2711 (2007).
- [237] S. Pisana, M. Lazzeri, C. Casiraghi, K. S. Novoselov, A. K. Geim, A. C. Ferrari, and F. Mauri, “Breakdown of the adiabatic Born-Oppenheimer approximation in graphene,” *Nature Mater.* **6**, 198–201 (2007).
- [238] L. Huang, A. B. Artyukhin, N. Misra, J. A. Martinez, P. A. Stroeve, C. P. Grigoropoulos, J.-W. W. Ju, and A. Noy, “Carbon Nanotube Transistor Controlled by a Biological Ion Pump Gate,” *Nano Lett.* **10**, 1812–1816 (2010).
- [239] R. J. Stöhr, R. Kolesov, J. Pflaum, and J. Wrachtrup, “Fluorescence of laser-created electron-hole plasma in graphene,” *Phys. Rev. B* **82**, 121 408(R) (2010).
- [240] J. González, F. Guinea, and M. Vozmediano, “Instability of anisotropic Fermi surfaces in two dimensions,” *Phys. Rev. Lett.* **79**, 3514 (1997).
- [241] J. González, F. Guinea, and M. A. H. Vozmediano, “Marginal Fermi-liquid behavior from two-dimensional Coulomb interaction,” *Phys. Rev. B* **59**, R2474 (1999).
- [242] E. H. Hwang and S. Das Sarma, “Dielectric function, screening, and plasmons in two-dimensional graphene,” *Phys. Rev. B* **75**, 205 418 (2007).
- [243] M. Polini, R. Asgari, G. Borghi, Y. Barlas, T. Pereg-Barnea, and A. H. MacDonald, “Plasmons and the spectral function of graphene,” *Phys. Rev. B* **77**, 081 411 (R) (2008).
- [244] M. Lazzeri, S. Piscanec, F. Mauri, A. Ferrari, and J. Robertson, “Electron Transport and Hot Phonons in Carbon Nanotubes,” *Phys. Rev. Lett* **95**, 236 802 (2005).
- [245] M. Lazzeri, F. Piscanec S.and Mauri, A. Ferrari, and J. Robertson, “Publisher’s Note: Electron Transport and Hot Phonons in Carbon Nanotubes [*Phys. Rev. Lett.* **95**, 236802 (2005)],” *Phys. Rev. Lett* **95**, 236 802 (2005).
- [246] B. Hecht, H. Bielefeldt, L. Novotny, Y. Inouye, and D. W. Pohl, “Local Excitation, Scattering, and Interference of Surface Plasmons,” *Phys. Rev. Lett.* **77**, 1889 (1996).

- [247] M. Kira, F. Jahnke, W. Hoyer, and S. W. Koch, “Quantum theory of spontaneous emission and coherent effects in semiconductor microstructures,” *Prog. Quant. Elec.* **23**, 189–279 (1999).
- [248] C. Attacalite, L. Wirtz, M. Lazzeri, F. Mauri, and A. Rubio, “Doped Graphene as Tunable Electron-Phonon Coupling Material,” *Nano Lett.* **10**, 1172–1176 (2010).

List of Abbreviations

2DEG	...	two-dimensional electron gas
ALD	...	atomic layer deposition
APD	...	avalanche photo diode
BL	...	blocking layer
BLG	...	bi layer graphene
CC	...	carrier-carrier
CCD	...	charged coupled device
CLSM	...	confocal laser scanning microscope
COF	...	covalent organic framework
CP	...	carrier-phonon
CW	...	continuous wave
EDX	...	energy dispersive X-ray spectroscopy
FLG	...	few layer graphene
FM	...	frequency-modulation
FP	...	Fourier-plane
FT-PS	...	Fourier-transform pulse shaping
FTO	...	fluor tin oxide
GDD	...	group delay dispersion
GVD	...	group velocity dispersion
IR	...	infrared
IRF	...	instrument response function
LC	...	liquid crystal
LED	...	light emitting diode
MBE	...	molecular beam epitaxy
MIIPS	...	multiphoton intrapuls interference phase scans
ML	...	mode-locked
Nd:YAG	...	neodymium-doped yttrium aluminum garnet; $\text{Nd:Y}_3\text{Al}_5\text{O}_{12}$
NL-PL	...	non-linear photoluminescence
P3HT	...	poly3-hexylthiophene
PCBM	...	[6, 6]-phenyl C_{61} -butyric acid methylester
PL	...	photoluminescence
PM	...	phase-modulated
RMS	...	root mean square
SBE	...	semiconductor Bloch equation
SEM	...	scanning electron microscopy
SHG	...	second-harmonic generation
SLG	...	single layer graphene
SLM	...	spatial light modulator
SPP	...	surface plasmon polaritons
TCSPC	...	time correlated single photon counting
TEM	...	transmission electron microscope
Ti:Sa	...	titan sapphire oscillator
TLP	...	transform-limited pulse

TT-COF	...	thieno[2,3-b]thiophene covalent organic framework
UPS	...	ultrafast pulse shaping

List of Figures

2.1	p-n junction	3
2.2	Skin depth of silicon	4
2.3	Different solar cell designs	5
2.4	Light traveling through medium	7
2.5	Chirped Gaussians pulses	10
3.1	Epi Geometry	15
3.2	Confocal Setup	16
3.3	Avalanche Photodiode	17
3.4	Detection Sensitivity of the Setup	18
3.5	Beam path for BFP imaging	19
3.6	TCSPC schematic of setup	20
3.7	TCSPC electronic	21
3.8	4f pulse shaper configuration	22
3.9	SLM Setup	22
3.10	$\text{Fe}_2(\text{IO}_3)_3$ structure	23
3.11	Iterative pulse optimization using MIIPS	24
4.1	Nanowire array covered with P3HT and its respective SEM and PL image .	27
4.2	PL-lifetime and intensity measurements for MDMO-PPV and P3HT on different substrates.	28
4.3	Metal induced PL-quenching for MDMO-PPV and P3HT	29
4.4	Excitation Polarization dependence of Ag-nanowire device	30
4.5	Excitation Polarization dependence of dielectric-nanowire device	31
5.1	TT-COF reaction scheme and its respective PXRD pattern	34
5.2	TT-COF TEM image and ad-desorption curves	36
5.3	TT-COF and PCBM host-guest complex	37
5.4	Optical characterisation of TT-COF and TT-COF:PCBM complex	38
6.1	TiO_2 layer thickness	43
6.2	HRTEM images of different TiO_2 -films	44
6.3	TiO_2 grain size as a function of calcination time	44
6.4	I-V characteristics of different TiO_2 films.	45
7.1	TiO_2 nanowire solar cell design	48
7.2	TiO_2 SEM images	49
7.3	TiO_2 TEM images and corresponding EDX spectra	50
7.4	IV-characteristics of different solar cells under illumination	51
7.5	PL-image of different solar cells	52
7.6	PL intensity and lifetime of hybrid solar cells	53
8.1	NL-PL signal of graphene	56
8.2	Reflectivity graphene	57

8.3	Raman-signal graphene	58
8.4	Power dependence of the NL-PL of graphene	59
8.5	Two temperature model for graphene	60
8.6	Energy dependence for the NL-PL from graphene	60
9.1	TEM image and respective EDX spectra of sample	64
9.2	Setup including the spatial light modulator	65
9.3	Carrier relaxation model in graphene	66
9.4	Pl as a function of chirp for graphene	67
9.5	NL-PL of graphene compared to SHG signal as a function of chirp	68
9.6	BFP images as a function of chirp	69
9.7	Modeled NL-PL spectra as a function of chirp	70
9.8	Modeled NL-PL spectra for different excitation power	73

List of Publications

A. Wisnet, M. Handloser, A. Folger, J. Dorman, L. Schmidt-Mende, A. Hartschuh, C. Scheu, "The influence of the blocking layer on the performance of TiO₂ nanowire hybrid photovoltaic device," *manuscript under preparation* (2014).

M. Handloser, T. Winzer, G. Piredda, N. Hartmann, A. Lombardo, R.S. Sundaram, A. Guggenmos, R. Ciesielski, A. Comin, U. Kleineberg, A. C. Ferrari, E. Malic, and A. Hartschuh, "Controlling charge carrier relaxation and photoluminescence in graphene using chirped laser pulses," *manuscript under preparation* (2014).

A. Wochnik, M. Handloser, D. Durach, A. Hartschuh, and C. Scheu, "Increasing crystallinity for improved electrical conductivity of TiO₂ blocking layers," *ACS Applied Materials and Interfaces* **5**, 5696-5670 (2013).

M. Dogru, M. Handloser, F. Auras, T. Kunz, D. Medina, A. Hartschuh, P. Knochel, and T. Bein "A Photoconductive Thienothiophene-Based Covalent Organic Framework Showing Charge Transfer Towards Included Fullerene," *Angew. Chem. Int.* **52**, 2920-2924 (2013).

M. Handloser, R. Dunbar, A. Wisnet, P. Altpeter, C. Scheu, L. Schmidt-Mende, and A. Hartschuh "Influence of metallic and dielectric nanowire arrays on the photoluminescence properties of P3HT thin films," *Nanotechnology* **23**, 305402 (2012).

S. Funk, G. Acuna, M. Handloser, and R. Kersting, "Probing the momentum relaxation time of charge carriers in ultrathin layers with terahertz radiation," *Opt. Exp.* **17**, 17450 (2009).

G. Acuna, F. Buergens, C. Lang, M. Handloser, A. Guggenmos, and R. Kersting, "Interdigitated terahertz emitters," *Electronics Letters* **44**, 3 (2008).

List of Conferences

Workshop on Nano Carbon Optics (WNCO)

Niederstetten (Germany), Sept 25.12-28.09.2012

Oral presentation: "*Graphene (graphite) as ultrafast non-linear plasmon source*"

MRS Conference

San Francisco (USA), April 6.12-9.04.2012

Poster presentation: "*Influence of metallic and dielectric nanowire arrays on the photoluminescence properties of P3HT thin films*"

DPG Conference

Berlin (Germany), Mar 25.12-30.03.2012

Oral presentation: "*Launching surface plasmons on a metal/dielectric interface by emission from graphene*"

Workshop on Nano Carbon Optics (WNCO)

Herrsching (Germany), Okt 6.11-9.10.2011

Oral presentation: "*Influence of metallic and dielectric nanowire arrays on the photoluminescence properties of P3HT thin films*"

CLEO Conference

Munich (Germany), Mai 22.11

Oral presentation: "*Graphene as ultrafast plasmon source*"

DPG Conference

Dresden (Germany), Mar 13.11-18.03.2011

Oral presentation: "*Plasmonic enhancement of light absorption in organic semiconductors using silver nanowire arrays*"

Workshop on Nano Carbon Optics (WNCO)

Niederstetten (Germany), Okt 7.10-10.10.2010

Oral presentation: "*Non-linear Photoluminescence from pristine Graphene*"

NIM Workshop

Venice (Italy), Sept 20.10-24.09.2010

Poster presentation: "*Non-linear Photoluminescence from pristine Graphene*"

Curriculum Vitae

Persönliche Daten

Name:	Matthias Karl Handloser
Geburtstag:	03. September 1979
Geburtsort:	München
Nationalität:	deutsch
Status:	verheiratet

Schul Ausbildung

Aug. 1986- Juni 1990	Grundschule
Aug. 1990 - Juni 2000	Klenze Gymnasium München
Juni 2000	Allgemeine Hochschulreife

Wehrdienst

Okt. 2000 - Okt. 2001	Zivildienst in der Kindertagesstätte Niederpöcking
-----------------------	---

Studium

Okt. 2001 - Mai. 2003	Technische Universität München Studium des Maschinenwesens
Sept. 2003 - Jan. 2010	Ludwig Maximilians Universität München Studium der Physik
Feb 2006	Vordiplom
Jan 2010	Diplom

Promotion

Jan 2010 - Juni 2013	Ludwig-Maximilians-Universität München Doktorarbeit zum Thema: Investigation of charge carrier dynamics in organic semiconductors and graphene for photovoltaic applications; Wissenschaftlicher Angestellter am Department für Chemie und Pharmazie im Arbeitskreis von Prof. Dr. A. Hartschuh
----------------------	--

Beruflicher Werdegang

Juni 2013 - Februar 2014	attocube systems AG Arbeit als Entwicklungsingenieur und Projektleiter in der Sensorentwicklung (R&D)
--------------------------	---

Acknowledgments

In the course of my PHD thesis I meet a couple of inspiring, innovative, brilliant and supportive people contributing significantly to the successful completion of this work. The contact with these persons opened up new dimensions for me, that were to have a lasting influence on my personality and my attitude towards science and life in general. Meanwhile real friendships have developed over the last three and half years supporting me also in a time of personal difficulties. For this and many other reasons I would like to extend my particular thanks to the following persons:

Prof. Achim Hartschuh for his continuous support and giving me the opportunity to work in his group. His enthusiasm towards the addressed scientific questions in this work and science in general motivated me day by day. He followed each step of this work with huge interest always willing to give advice and showing me solutions towards certain scientific and non-scientific questions during this time. I also would like to thank him for giving me the opportunity to present our results on various workshops and conferences.

I also want to thank **Prof. Christina Scheu** for the cooperation with me addressing different scientific questions of organic polymers. Her deep interest towards material science introduced me to the fascinating world of the transmission electron microscopy. Additionally I want to thank her for continuously giving me the possibility for discussion about science and life and also for being the second reviewer of this thesis.

Prof. Thomas Bein for giving me the opportunity to work interdisciplinary in a fruitful cooperation between chemistry and physics.

The group of **Prof. Ermin Malic** and especially **Torben Winzer** I want to thank for their theoretical calculations of the ultrafast experiments on graphene.

Dr. Mirjam Dogru for her patience, friendship and continuous will to educate me in chemistry and for her interest in physics. I enjoyed the fruitful discussions about science and life in general.

Another big thanks goes to **Dr. Angela Wochnik** for being always willing to take a "closer look" with the TEM, for her friendship and continuous support during the time.

Andreas Wisnet I also want to thank for his contribution to the work on organic solar cells.

To all the former and present group members I would like to express my gratitude for the great time I had. For the scientific discussions and especially for the non-scientific ones. For the friendship and the fun we had goes a big thanks to **Miriam, Nicolai, Tobias, Tobia, Julia, Alberto, Alexandre** and **Richard**. A very special thanks goes to **Carsten** who passed away in a tragic accident. I am grateful for the time we had.

Nina I want to thank for her friendship and support during the time. A special thanks goes to **Giovanni** for being always willing to explain the physics of ultrafast experiments to me and for his humor and patience in the lab.

To my former Bachelor students **Christine Hösl** and **Alena Folger** I want to especially express my gratitude for the good piece of work they did. Their regardless approach towards scientific problems addressing the influence of electric fields on carbon nanotubes and the photophysics of TiO₂ in organic polymers always inspired and motivated me.

Philipp Altpeter has built most of the the used samples, while **Alexander Guggenmos** prepared the coatings of the used substrates. Without these persons most measurements wouldn't have been possible.

Antonio Lombardo and **Prof. Andrea Ferrari** for transferring the exfoliated graphene and for fruitful scientific discussions.

To my brother **Johannes** goes a big thanks for being always in good mood and helping me to stay in real life.

My father **Günther** for his interest in me and my work and for giving me the possibility to explore the world like I did. Thank you very much for believing in me and for your continuous support.

The biggest thanks goes to my wife **Gerit**. For her patience and love and for being there during all the time. Without you it wouldn't have been possible. Thank you so much!